COMPUTATIONAL FLUID DYNAMICS SIMULATIONS OF SHIP AIRWAKE WITH A HOVERING HELICOPTER ROTOR

A THESIS SUBMITTED TO
THE GRADUATE SCHOOL OF NATURAL AND APPLIED SCIENCES
OF
MIDDLE EAST TECHNICAL UNIVERSITY

BY

EZGI ORBAY

IN PARTIAL FULFILLMENT OF THE REQUIREMENTS
FOR
THE DEGREE OF MASTER OF SCIENCE
IN
AEROSPACE ENGINEERING

SEPTEMBER 2016

Approval of the thesis:

COMPUTATIONAL FLUID DYNAMICS SIMULATIONS OF SHIP AIRWAKE WITH A HOVERING HELICOPTER ROTOR

submitted by **EZGI ORBAY** in partial fulfillment of the requirements for the degree of **Master of Science in Aerospace Engineering Department, Middle East Technical University** by,

Prof. Dr. Gülbin Dural Ünver
Dean, Graduate School of **Natural and Applied Sciences** ______________

Prof. Dr. Ozan Tekinalp
Head of Department, **Aerospace Engineering** ______________

Assoc. Prof. Dr. Oğuz Uzol
Supervisor, **Aerospace Engineering Department, METU** ______________

Assist. Prof. Dr. Nilay Sezer Uzol
Co-supervisor, **Aerospace Engineering Department, METU** ______________

Examining Committee Members:

Assoc. Prof. Dr. Sinan Eyi
Aerospace Engineering Department, METU ______________

Assoc. Prof. Dr. Oğuz Uzol
Aerospace Engineering Department, METU ______________

Assoc. Prof. Dr. İlkay Yavrucuk
Aerospace Engineering Department, METU ______________

Assoc. Prof. Dr. Eray Uzgören
Mechanical Engineering Department, METU NCC ______________

Assoc. Prof. Dr. Mehmet Metin Yavuz
Mechanical Engineering Department, METU ______________

Date: ______________

I hereby declare that all information in this document has been obtained and presented in accordance with academic rules and ethical conduct. I also declare that, as required by these rules and conduct, I have fully cited and referenced all material and results that are not original to this work.

Name, Last Name: EZGI ORBAY

Signature :

ABSTRACT

COMPUTATIONAL FLUID DYNAMICS SIMULATIONS OF SHIP AIRWAKE WITH A HOVERING HELICOPTER ROTOR

Orbay, Ezgi
M.S., Department of Aerospace Engineering
Supervisor : Assoc. Prof. Dr. Oğuz Uzol
Co-Supervisor : Assist. Prof. Dr. Nilay Sezer Uzol

September 2016, 92 pages

In this thesis, Computational Fluid Dynamic simulations of ship airwake for a simple ship geometry are performed for the horizontal and inclined deck configurations and also with and without the helicopter rotor over the deck. An actuator disk model is used for the CFD simulations of a rotor model hovering over the flight deck. All of the computations are performed by using a commercial finite volume CFD flow solver. The unstructured tetrahedral grids are generated in the computational domain including ship geometry and rotor disk. The flow around the Simple Frigate Shape 2 (SFS2) ship geometry is computed by solving RANS and hybrid RANS/LES equations. The steady-state and unsteady computations with different turbulence models are performed. A good validation is obtained with the hybrid RANS/LES turbulence model. After the validation study for the simulation results with the standard (horizontal) model, ship motion due to sea waves is discussed and only an instant of the roll motion is considered as an inclined flight deck problem and investigated. Therefore, a 10 degree rotation about x-axis is given to ship geometry, which illustrates roll motion of ship in rough sea conditions. Comparisons of the results with horizontal (un-inclined) and inclined deck cases are done. Also, a rotor disk with zonal boundary conditions is used with both horizontal and inclined ship models to investigate downwash effect of rotor on ship airwake. Full-scale, four-bladed S-76 helicopter rotor is selected as the rotor model. Rotor only case is first solved and validated with the available wind tunnel data. Then, steady-state simulations for ship with rotor cases are performed. In this part of the study, the effect of ship airwake on rotor performance was not considered, only the effect of hovering rotor wake (downwash) on the ship airwake was taken into account. Flow around the inclined ship deck is observed as different from the horizontal deck. When a rotor is also included over the deck, the flow features such as vortical structures and vertical velocity magnitudes are changed showing that the interactions is more complicated to accurately model and solve.

Keywords: Ship Airwake, Computational Fluid Dynamics (CFD), Helicopter Rotor, Actuator Disk Model

ÖZ

GEMİ İZ BÖLGESİNDE ASKIDA DURAN HELİKOPTER ROTOR HESAPLAMALI AKIŞKANLAR DİNAMİĞİ SİMULASYONLARI

Orbay, Ezgi
Yüksek Lisans, Havacılık ve Uzay Mühendisliği Bölümü
Tez Yöneticisi : Doç. Dr. Oğuz Uzol
Ortak Tez Yöneticisi : Yrd. Doç. Dr. Nilay Sezer Uzol

Eylül 2016 , 92 sayfa

Bu tezde, basit bir gemi geometrisi etrafındaki hava iz bölgesinin Hesaplamalı Akışkanlar Dinamiği simülasyonları, yatay ve eğik gemi güvertesi için ve ayrıca gemi güvertesi üzerinde rotorlu ve rotorsuz olarak yapıldı. Bir aktüatör disk modeli, uçuş güvertesi üzerinde askıda duran bir rotor modelinin HAD simülasyonları için kullanıldı. Bütün hesaplamalar ticari bir sonlu hacim HAD akış çözücü kullanılarak yapıldı. Gemi geometrisini ve rotor diskini içeren hesaplama alanında yapısal olmayan üçgen yüzeyli çözüm ağı oluşturuldu. Basit Fırkateyn Şekli 2 (SFS2) gemi geometrisi etrafındaki akış RANS ve hibrit RANS/LES denklemleri çözülerek hesaplandı. Daimi ve zamana bağlı hesaplamalar farklı türbülans modelleri kullanılarak yapıldı. Hibrit RANS/LES türbülans modeli ile iyi bir doğrulama elde edildi. Standart (yatay) model ile elde edilen simülasyon sonuçları için yapılan doğrulama çalışmasından sonra, deniz dalgalarının oluşturduğu gemi hareketi tartışıldı ve sadece yuvarlanma hareketinin bir anlık durumu eğik uçuş güvertesi problemi olarak göz önüne alındı ve incelendi. Bu yüzden, gemi geometrisine, geminin sert deniz koşullarındaki yuvarlanma hareketini yansıtan x-ekseni etrafında 10 derecelik bir dönüş uygulandı. Yatay (eğik olmayan) ve eğik güverte durumları için elde edilen sonuçların karşılaştırılması yapıldı. Ayrıca, bölgesel sınır koşulu ile rotor diski, hem yatay hem de eğik gemi modelleri ile, rotorun gemi iz bölgesi hava akımına olan aşağı hava akışı etkisini araştırmak için kullanıldı. Tam ölçekli, dört palalı S-76 helikopter rotoru, rotor modeli olarak seçildi. İlk olarak, sadece rotor durumu çözüldü ve mevcut rüzgar tüneli verileri ile doğrulandı. Daha sonra, rotorlu gemi vakaları için daimi durum simülasyonları gerçekleştirildi. Çalışmanın bu kısmında, gemi iz bölgesi hava akımının rotor uçuş performansına etkisi dikkate alınmayıp, sadece askıda kalan rotorun iz bölgesinin (aşağı hava akışının) gemi iz bölgesi hava akımı üzerindeki etkisi incelendi. Eğik gemi güvertesi etrafındaki akış, yatay gemi güvertesininkinden farklı olarak gözlemlendi. Güverte üzerine rotor eklendiğinde, girdap yapıları ve dikey hız büyüklüğü gibi akış özellikleri değişti. Bu da, etkileşimlerin doğru bir şekilde modellemek ve çözmek için daha da karmaşık hale geldiğini göstermektedir.

Anahtar Kelimeler: Gemi İz Bölgesi Hava Akımı, Hesaplamalı Akışkanlar Dinamiği (HAD), Helikopter Rotoru, Aktüatör Disk Modeli

To my family and people who are reading this page

ACKNOWLEDGMENTS

First of all, I would like to express my great thanks to especially co-supervisor Assistant Professor Nilay Sezer-Uzol for her excellent motivation, guidance, and friendship. She always encourages me and never let me reduce my incentive. Also, I would like to thank my supervisor Associate Professor Oğuz Uzol. It was a great honor to work with both of them for the last two years and our cooperation influenced my academical and world view highly.

I deeply thank to all of professors in the Department of Aerospace Engineering for their guidance and support.

I want to thank all my research assistants and project assistants friend for their supports and most importantly their frienships. Especially, special thanks should be given to Metehan Yayla for his valuable comments and for his helps.

I am grateful to my office friend Emre Oktay, Tuğba Tunçel, Derya Kaya, Tansu Sevine, Berk Gür, Muharrem Özgün. They have been exquisite friends and supporters. I want to thank Murat Şenipek, Mehmet Şahbaz and Alper Açıcı for their helps during my master study.

I would also like to thank you my dear husband Ziya Akcengiz for always listening and leading me from the start to end of this thesis and support through our lives.

Finally, I would like to thank to my family for their endless support and love. And I thank to my sister for being an excellent mentor and friend through my entire life. Last but not the least, I wish to thanks all my friends with whom I have worked on stage and my dearest friends for their wonderful friendship.

I would like to end my words with the quote from Doctor Who: "... , before I go, I just want to tell you, you were fantastic, absolutely fantastic. And do you know what? So was I!"

TABLE OF CONTENTS

LIST OF TABLES

TABLES

LIST OF FIGURES

FIGURES

CHAPTER 1

INTRODUCTION

The helicopter ship operations such as launch and recovery are one of the most challenging operations for the pilots. The pilot should overcome bad weather conditions, airwake of the ship due to superstructures, visibility problems and moving flight deck during hovering over or landing on the flight deck. The most dangerous problem occurs because of ship airwake, which is a highly turbulent, three dimensional, vortical flow with large regions of separation behind the superstructure of the ship and over the flight deck. In order to make helicopter-shipboard operations safe, The Safe Helicopter Operating Limits (SHOLs) should be determined for each helicopter-ship combination. SHOLs are generally expressed by wind-over-the deck (WOD) envelopes, which show allowable wind conditions in terms of azimuth angle and speed for a given helicopter ship combination. In Figure 1.1, an example of WOD envelope is given.

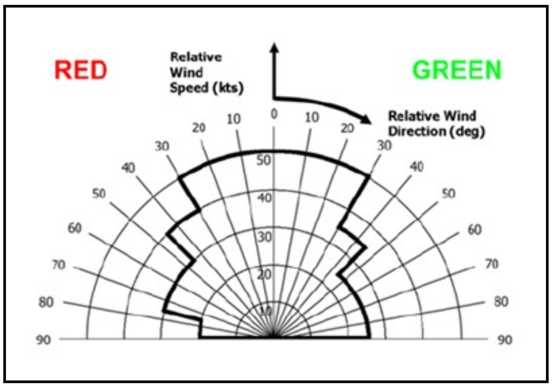

Figure 1.1: WOD Envelope [32]

These envelopes can be obtained by either experimentally or computationally. In the experiments, full scale tests or model scale wind tunnel tests are performed. It is hard to obtain WOD envelopes by full scale tests because they are expensive, time consuming and unsafe. Moreover, results can vary according to the pilot's evaluation. Also, model scale wind tunnel tests are costly and time consuming, and they can remain weak to create the complexity of real flow field. On the other hand, numerical methods are safer, cheaper and easier to control. By using suitable models, the results can simulate the real situation.

When simulating the complexity of the airwake, some technical challenges may occur. Modeling of the ship is difficult due to its complex geometry including towers, antennae, radar dishes, exhaust stacks. Also, moving flight deck which is due to sea waves can alter the characteristics of flowfield. Therefore, modeling sea waves and ship motion is important. Moreover, interaction between ship and helicopter's rotor and fuselage must be taken into account, which makes the flow more complex. In addition to these, the results can be affected by application of atmospheric boundary layer and atmospheric turbulence.

In this thesis, the flow over Simple Frigate Shape 2 (SFS2) is simulated by using Computational Fluid Dynamics (CFD). In order to investigate the effect of the inclined flight deck due to ship 2 motion, 10 degree roll is given to SFS2. An illustration of inclined flight deck of a ship with a hovering helicopter on it is presented in Figure 1.2. Also, by using helicopter rotor disk model, the effect of the rotor on the ship airwake is studied. All of the computations are performed by using a commercial flow solver code of CFD++ software.

Figure 1.2: Helicopter hovering on inclined flight deck of a ship due to sea waves [8]

In the literature, the ship airwake studies mainly focus on understanding the physics of the flowfield, obtaining more accurate simulation, investigating DI and interaction between ship airwake and rotor, with effects of Atmospheric Boundary Layer and ship motion. The studies concerning ship airwake are presented in table form in Table 1.1 before 2005. The studies conducted after 2005 are listed in Table 1.2. A summarized table comprising Simple Frigate shape and similar frigates used in ship airwake studies are given in Figure 1.3. In this table, both experimental and computational studies concerning only ship airwake and DI between airwake and helicopter rotor are presented. The detailed summary of the studies, performed before 2005 on ship airwake and dynamic interface, is given by Sezer-Uzol et al [56]. Review on the previous studies both experimental and computational, performed after 2005 on ship airwake and dynamic interface, are summarized in the next sections 1.1 and 1.2. Also, a short review of the literature on ship motion is presented in the section 1.3.

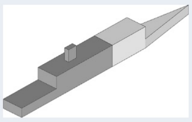	SFS	(Mora, 2014)
	SFS2	(Forrest, J.S., Owen, I., 2010), (Lee, R., 2007), (Zan et al. 2003)
	USNA YP676	(Snyder, 2012)
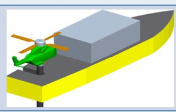	Merlin AW-101 & SRF (The shortened research frigate)	(Forrest, J. S. , Kääriä, C. H., Wang, Y., Padfiel, G. D. , and Owen, I., 2012)
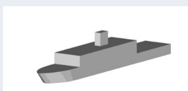	SFSN	(Muijden, J. Van, Boelens, O. J., Vorst, J. Van Der, Gooden, J. H. M, 2013)

Figure 1.3: Summary of the literature investigating airwake of only SFS and similar frigate shapes

	Ship	References
Experimental (Ship Only)	LHA	(Polsky, S. A, and Bruner, C. W. S.,2000), (Polsky, S. A.,2002), (Daley, W. H., 1998)
	DD-963	(Johns, M. K., 1988), (Johns, M. K. and Healey, J. V., 1989)
	LPD-17	(Tai, T. C., 1995), (Guillot, M. J. and Walker, M. A., 2000)
	GF	(Zan, S. J. and Garry, E. A., 1994
	CPF	(Zan, S. J., Syms, G. F., and Cheney, B. T., 1998), (Syms, G. G., 2004)
	SFS	(Cheney, B. T. and Zan, S. J., 1999), (Zan, S. J., 2001)
	La Fayette frigate model	(Taghizad, A., Verbeke, C. and Desopper, A., 1998)
	Others	(Maslov, L. A., Valuev, N. D., and Zharinov, A. V., 1998)
Experimental (Ship and Helicopter)	LPH-USS TRIPOLI & XP-115	(Ball, J. C., 1983)
	LPH-9 USS GUAM & H-46	(Ball, J. C. and White, W. R., 1984)
	Others	(Williams, S. L. and Long, K. R., 1997)
	CPF & a 4-bladed rotor model	(Zan, 2002)
	CPF & a rotorless Sea King fuselage	(Lee and Zan, 2004)
	LHA & V-22 tiltrotor	(Silva et al., 2004)
Computational (Ship only)	LHA	(Tai, T. C., 1995), (Polsky, S. A., and Bruner, C. W. S., 2000), (Polsky, S. A., 2002), (Polsky, S. A., 2003), (Arunajatesan, S., Shipman, J. D., and Sinha, N., 2004), (Sezer-Uzol et al., 2005)
	CPF	(Syms, G. F., 2004)
	LPD	(Tai, T. C., 1995)
	LPD-17	(Guuillott, M. J., and Walker, M. A., 2000), (Camelli, F., Lohner, R. and Sandberg, W., and Ramamurti, R., 2004), (Sezer-Uzol et.al.2005)
	DD-963	(Tai, T.C., and Carico, D., 1995)
	SES(Surface Effectt Ship)	(Moctar, O. E., and Bertram, V., 2003)
	SFS1	(Reddy, K. R., Toffoletto, R., and Jones, K. R. W., 2000)
	Royal Navy Ships	(Bogstad, M. C., Habashi, W. G., Akel, I., Ait-Ali-Yahia, D., Giannias, N. and Longo, V., 2002)
		(Zan, S. J., 2003)
	DDG-5111	(Landsberg, A. M., Sandberg, W. C., Ypung, T. R., J., and Boris, J. P, 1996)
Computational (Ship and Helicopter)		(Zan, S. J., and Syms, G. F., 19955), (Landsberg, A. M., Young, T. R.,j., and Boris, J. P., 1995), (Tattersall, P., Albone, C. M., Soliman, M. N., and Allen, C. B., 1998), (Wakefield, N. H., Newman, S. J. and Wilson, P. A., 2002),
	SFS & CVN-75 & LHA	(Modi, A., 1999)
	AV-8B Harrier	(Arunajatesan, S. Shipman, J. D., and Sinba, N., 2004)
	LPD-17	(Sezer-Uzol, N., Sharma, A., and Long, L. N., 2005), (Sharma, A., and long, L. N., 2001)
Dynamic Interface	LHA & UH-60A	Lee et al. 2005
	LHA & UH-60A	Lee, D., Horn, J. F., Sezer-Uzol, N. and Long, L. N.
	Others	Wilkinson, C. H., Zan, S. J., Gilbert, N. E. and Funk, J. D.
		Wilkinson, C. H., Roscoe, M. . and VanderVliet, G. M, 2001
		Taghizad, A., Verbeke, C. and Desopper, 1998
		Bogstad, M. C., Habashi, W. G., Akel, I., Ait-Ali-Yahia, D., Giannias, N. and Longo, V., 2002
		Healey, J. V., 1987, Lee, D. and Horn, J. F., 2002
		Tatte, S. J. and PPadfield, G. D., 1994
		Williams, S. and Long, K., 1997, Bunnell, J. W., 2000
		Lumsden, B. R., Wilkinson, C. H. and Padfield, G. D., 1998
		de Ferrier, B. and Langlois, B., 1998
		Wilkinson, C. H., VanderVliet, G. M. and Roscoe, M. F., 2000
		VanderVliet, G. M., Wilkinson, C. H., and Roscoe, M. F., 2000

Table 1.1: Literature review consisting of studies before 2005[56]

	Ship	References
Experimental (Ship only)	SFS	(Mora, 2014)
	SFS2	(Forrest, J.S., Owen, I., 2010)
	USNA YP676	(Snyder, 2012)
Experimental,(Ship and Helicopter)	Merlin AW-101 & SRF	(Forrest, J. S. , Kääriä, C. H., Wang, Y., Padfiel, G. D., and Owen, I., 2012)
	A simplified 1/50 scale frigate waterline model and traverse mounted powered rotor	(Nacakli, Y. & Landman, D., 2011)
Computational (Ship only)	LHA	(Sezer-Uzol, N., Sharma, A., and Long, L. N., 2005), (Liu, 2012)
	LPD-17	(Sezer-Uzol, N., Sharma, A., and Long, L. N., 2005)
	SFS1	(Syms, 2008), (He, S. H., Liu, D. Y., & Tan, D. L., 2014)
	SFS2	Forrest, J.S., Owen, I., 2010), (Syms, 2008), (Zhang, F., Xu, H. & Ball, N. G., 2009)
	SFSN	(Muijden, J. Van, Boelens, O. J., Vorst, J. Van Der, Gooden, J. H. M., 2013)
	LPD2	(Muijden, J. Van, Boelens, O. J., Vorst, J. Van Der, Gooden, J. H. M., 2013)
	T23	(Forrest, J. S., Owen, I., 2010), (Thornber, B., Starr, M. & Drikakis, D., 2010)
	Wave class A O	(Thornber, B., Starr, M. & Drikakis, D., 2010)
	USNA YP676	(Snyder, 2012)
		(Gaonkar, 2006)
Computational,(Ship and Helicopter)	SFS2	(Hodge, S. J., Zan, S. J., Roper, D. M., Padfield, G. D., & Owen, I., 2009), (Quon, E. W., Cross, P. A., Smith, M. J., Rosenfeld, N. C. & Whitehouse, G. R., 2014)
	Generic ship model	(Scott, P., Owen, I. & White, M., 2014)
		(Ramos, R. L. C. B., Andrade, D. & Góes, L. C. S., 2009)
Dynamic Interface	LHA & UH-60A	Lee at al. 2005 [1-3], (Alpman, E., & Long, L., 2007), (Horn, J. F. & Bridges, D. O., 2007), (Horn, J. F., Bridges, D. O. & Lee, D., 2006), (Montanye, P. L., Smith, E. C., Rahn, C. & Conlon, S. C., 2009)
	DDG-81 Class Ship & H-60 Actuator disk model	(Schau, K. A., Gaonkar, G. H. & Polsky, S., 2014)
	CPF& Shipborne Sea King Helicopter & actuator disk model	(Crozon, C., Steijl, R. and Barakos, G. N. , 2014)
	SH-60B&Type 23 Frigate and Wave class auxiliary oiler	(Forrest, J. S., Owen, I., Padfield, G. D. and Hodge, S. J., 2012)
	SH-60B & SFS2	(Forrest, J. S., Owen, I., Padfield G. D. & Kaaria, C. H., 2009)
	Lynx-like helicopter & SFS2 and Type 23	(Forrest, J. S., Hodge, S. J., Owen, I. & Padfield, G. D., 2008)
	DDG-81	(Sparbanie, S. M., Horn, J. F., Geiger, D. H. & Sahasrabudhe, V., 2009), (Rigsby, J., Geiger, D. & Xin, H., 2011)
		(He, C., Lee, D., Zhao, J. & Ware, C., 2011)
	DDG-81 & S-92-class FBW RCAH	(Geiger, D. H., Horn, J. F. & Polsky, S., 2008)
		(Rajmohan, N., Zhao, J., He, C., Kim, J., Sankar, L.N. & Prasad, J.V.R., 2012)
	SFS2	(Forrest, J. S., Kaaria, C. H. & OWen, I., 2010)
		(Schafer, S., Horn, J. F. & Cooper, J., 2015)
	Others	(Horn, J F., Sparbanie, S. M., Cooper, J. & Schierman, J., 2009), (Gaonkar, Toward a Complete Stochastic Model of Airwake Turbulence for Helicopter Shipboard Operation, 2007)
	Type-23 frigate & Type-45 Destroyer	(Turner, G., Clark, W., Cox, I., Finlay, B. & Duncan, J. , 2006)
	MH-60S	(Keller, J. D., Wachspress, D. A. & Hoffler, J. C., 2015)
	SH-60B& DDG-88	(Ferrier, B. & Carico, D., 2007)
Ship Motion	X-craft Catamaran, HSS Trimaran	(Lin, R. & Kuang, W., 2011)
		(Journée, J.M.J. & Pinkster, J., 2002)
	Floating Production Storage and, Offloading, (FPSO)	(Li, X., Zhang, T., Zhang, Y. & Wang, Y., 2014)
	TMV-114 Fast Ferry	(Soneson, G. L. & Horn, J. F. , 2014)
		(Briggs, M. J., Demirbilek, Z. & Lin, L., 2014)
	DTMB model 5512	(Carrica, P. M., Wilson, R. W., Noack, R. W. & Stern, F., 2007)
	KRISO Container	(Tezdogan, T., Demirel, Y. K., Kellett, P., Khorasanchi, M , Incecik, A. & Turan, O., 2015)
		(Mousaviraad, 2010)
	S175 hull	(Kim, Y., Kim, K. H., Kim, J. H., Kim, T., Seo, M. G. & Kim, Y. , 2013)
	KCS container	(Simonsen, C. D., Otzen, J. F., Joncquez, S. & Stern, F., 2013)
	4500 TEU class container carrier	(Kim, S. & Lee, H., 2011)
	Oliver Hazard Perry Class FFG frigate, ANZAC Class frigate	(Khantsis, 2006)
		(Ueng, S. K., Lin, D. & Liu, C. H., 2008)
		(Weymouth, G. D., Wilson, R. V. & Stern, F., 2005)
	DTMB 5613	(Carrica, P. M., Sadat-Hosseini, H. and Stern, F., 2012)
	DTMB 5512, Full scale race boat hull	(Owen, H., Houzeaux, G., Samaniego, C., Lesage A. C. and Vázquez, M., 2013)
	Littoral Combat Ships	(Azcueta, 2004)

Table 1.2: Literature review consisting of studies after 2005

1.1 Previous Studies on Ship Airwake

In order to investigate and understand turbulent, unsteady characteristics of ship airwake, many studies on various ship models were conducted computationally and experimentally. As mentioned above, this part gives only the recent studies on ship airwake after 2005, since the studies before 2005 were presented previously.

The recent experimental studies include wind tunnel tests on SFS [41], SFS2 [13, 49], and USNA YP676 [61] and LHA [50], and full scale tests on SFS [41] and USNA YP676 [60]. These tests provide flow topology on the surface and velocity data including mean velocities and turbulence intensities. Also, the interaction between the ship air wake and the helicopter was studied by Forrest [26] and Nacakli [44] with model scales of Merlin AW-101 and SRF and a simplified 1/50 scale frigate waterline model and traverse mounted powered rotor respectively.

The Computational Fluid Dynamic (CFD) analyses were performed on different ship models with different numerical methods. Many researchers focused on only analysis of air wake. In 2006, Sezer-Uzol et al. [56] investigated the flow around a Landing Helicopter Assault (LHA) ship and a Landing Platform Dock-17 (LPD-17) ship by using CFD solver PUMA2 for inviscid flow with slip wall boundary conditions for the ship and sea surface. LHA was also verified with experimental data in 2012 [38] by using three different grids including prismatic layer grid and it was shown that the prismatic layers do not affect the results. In 2008, Syms studied both SFS and SFS2 geometries by using Lattice-Boltzman method [63]. Various spatial discretization schemes on SFS were discussed by He et al. in 2014 [18]. Forrest et al. validated their computational data of SFS2 with experimental results and compute the flow over T23 ship by using hybrid turbulence model DES with SST $k-\omega$ [13]. They stated that application of Atmospheric Boundary Layer on computations can increase the accuracy. Another study on SFS2 was conducted by Quon et al. in order to assess the ability of URANS and URANS/Vorticity Transport hybrid computational methodology to capture airwake characteristics [49]. Three flow conditions on SFS2 was also investigated by Zhang et al. using unsteady flow solver Cobalt in order to use the results in a work of helicopter-ship interaction [69]. Muijden et al. solved the flow over SFSN (SFS with modified bow by National Aerospace Laboratory) and LPD2 by steady-state with RANS and unsteady with hybrid RANS/LES turbulence model, and compared results with experimental data [43]. Implicit large eddy simulation was validated on two different Royal Navy ships; T23 and Wave Class AO by Thornber et al by comparing results with both wind tunnel and full-scale tests [65]. In 2012, Snyder et al. solved flow over USPN-76 using Monotone Integrated Large Eddy Simulation for 6 different WOD angles [60].

In addition to the airwake computations, there have been several computational studies on ship airwake/helicopter rotor. Hodge et al used the time-accurate ship airwake data obtained on SFS2, in order to observe unsteady aerodynamic load on helicopter in 2009 [19]. Moreover, ship motion effect on pilot workload was studied in the flight simulator in this study. In 2014, the effect of the ship size was investigated by using DES turbulence model and the obtained data was extracted to perform an offline flight mechanics operating analysis of the SH60B rotor response [55].

1.2 Previous Studies on Dynamic Interface

The helicopter and ship interaction has been an important topic for researchers. This is mainly due to investigating pilot's response and workload during helicopter's shipboard operations, determining the safe WOD angles, generating safe flight trajectories for helicopters and developing flight simulators for training pilots and engineering. These studies were conducted on different classes of ships and helicopters such as SFS2 [12, 48] with SH-60B [25, 55] and Lynx-like helicopter [11], LHA with UH-60A [2]. Additionally, interactions of DDG-81 class ship with H-60 actuator disk model [54], CPF ship with Shipborne Sea King Helicopter, and actuator disk model [7], Type 23 Frigate and Wave class auxiliary oiler with SH-60B [14], DDG-88 ship model with SH-60B [9] helicopter/ship combinations were investigated.

The ship airwake obtained from coupled studies with rotor wake have very different flow characteristics compared to the isolated ship simulations [51]. In 2005, Lee et al. studied DI between LHA and UH-60A by using PUMA2 and GENHEL [35, 33, 34]. By using the same code and flight dynamics simulation model, Alpman and Long also investigated interaction between LHA and UH60-B [2], and they compared fully coupled results with one way coupled and no-coupling cases in 2007. As a result, it was stated that the airwake is influenced by the rotor wake and this effect gets powerful as helicopter moves closer to ground and hangar structure. In 2009, the study with the same helicopter/ship combination concluded in that trailing edge flaps can be useful for shipboard gust alleviation by Montanye et al. [40]. Downwash effect of H-60 rotor on DDG-81 class ship was investigated by Schau et al in 2014 [54] and it was stated that airwake energy increases with downwash in one order of magnitude. The steady-state calculations with actuator disc model and CPF ship model were observed to be sufficient to understand the importance of the coupling effects by Crozon et al in 2014 [7]. They also performed unsteady RANS simulations using Sea King helicopter rotor blades. The SHOL diagrams for the FLIGHTLAB model of SH-60B Seahawk helicopter over the deck of a Type 23 frigate and a Wave class auxiliary oiler were determined by Forrest et al [14]. In this study, pilot's ratings and comments were also mentioned. SH-60B was also integrated on the study of SFS2 ship airwake at 2 different WOD angles with the various helicopter locations [25]. Another ship-helicopter DI study of Type 23 frigate was conducted by using Merlin helicopter simulator as a part of project SAIF [66]. When determining SHOL for a helicopter-ship combination, small-scale geometric features should be also taken into account according to Forrest et al [11]. They found that relatively small-scale geometric features can alter the characteristics of the flow field even though they may not affect the pilot ratings. In 2007, Gaonkar developed a complete stochastic model for ship airwake [15]. In this paper, complete stochastic was referred to autospectral densities of all velocity components and cross-spectral densities of any combination of velocity components at two arbitrarily chosen points. Stochastic model for airwake instead of the CFD was preferred over DDG-81 model ship by Sparbanie et al. in 2009 [62] and Rigsby et al in 2011 [52]. Geiger et al. studied on the development of a flight control design to compensate the airwake load on S-92 class over a DDG-81 shipboard environment [16]. In 2011, He et al. developed a simulation and control tool for a helicopter-ship dynamic interface [17]. Horn et al. developed an on-line algorithm to identify the airwake disturbance on rotors by using linear filters on unsteady disturbance during real time simulations [20]. Schafer et al. also carried out a work on the development of methodology of the identification of ship airwake gust disturbance in order to use this data on DI simulations later [53].

The effect of the hangar edge on the helicopter/ship DI was also investigated over SFS2 [12]. While the modifications decreasing airwake turbulence does not necessarily decrease the pilot workload, the relation between the modifications increasing the effect of airwake turbulence and the pilot workload is more obvious.

1.3 Previous Studies on Ship Motion

Also, moving platform is another difficulty for helicopters' shipboard operations. The airwake around the ship's superstructure is affected by moving flight deck due to sea waves. This creates more dangerous environment for helicopters' landing and hovering.

The ships floating over sea are under the influence of 6 degree of freedom rigid body motion. These are translational motions; heave, sway and surge, and rotational motions; pitch, roll and yaw. Heave, pitch and roll occur due to sea waves which is the most important factor of the unintended ship motion. Sea waves can be classified as regular and irregular waves. While the regular waves are harmonic, the irregular ones are obtained by superposition of sinusoidal waves [24]. For example, Soneson and Horn used the sum of sine waves to illustrate the motion of TMV-114 Fast Ferry [61].

In the literature, there are many studies [61, 4, 5, 29, 30, 36, 37, 46, 58, 64] investigating the ship response to sea waves for different sea states. In 2011, a computer program WISH which uses time-domain Rankine panel method and solves ship response to linear and nonlinear sea waves was developed by Kim et al [30]. Like the panel methods, the CFD also gives valid results for fully nonlinear analysis [29]. The Volume of Fluid (VOF) method is used in order to model the sea waves in the CFD analysis of ship motion [36]. Lin and Kuang developed a fully nonlinear dynamic numerical model for X craft catamaran with a fixed heading, which means the yaw, surge and sway motions were not investigated [37]. Carrica et al. studied heave and pitch motions by using dynamic overset grids and their computational results showed excellent agreement with experimental data [6]. Tezdogan et al. again used overset grids to model the computational domain which was constructed for calculation of the ship response to sea waves by using URANS equations [64]. In 2005, Weymouth et al. compared steady-state and unsteady RANS simulations of heave and pitch motions and investigated first and second harmonic amplitudes of motions [68]. Mousaviraad conducted a comprehensive study including harmonic waves and windy conditions effects on ship resistance, maneuvering, seakeeping and controllability [42]. In this study, URANS turbulence model and single-phase level-set free surface model were preferred. In 2013, Simonsen et al. conducted experimental and computational studies over KCS container to analyze the heave and pitch motions during regular waves [58].

In 2006, a control system was developed for unmanned aerial vehicle's shipboard operations using motion data of FFG Sidney and ANZAC frigate under the influence of sea waves [27]. There were given 10 different sea states, from 0 to 9, describing calm and phenomenal water. It was stated that frigates perform heave between +2.5 m and -2.5 m, pitch between +4.8 degree and -4.8 degree and roll between +26.5 degree and -26.5 degree for sea state 6 which corresponds to very rough wave conditions. Ueng et al. simulated ship motions for three different classes; warship, craft and fishing boat in 2008 [67]. Sea waves are also influenced by the ship rigid body; therefore there is a coupling effect on ship motions. In the literature, studies investigating this coupling effect also exist [30].

1.4 Objective of Thesis

The ship airwake is a vital issue for helicopters' shipboard operations. Complex nature of flow over the flight deck due to superstructures of ship creates dangerous environment for the pilots. Therefore, it is important to understand the aspects of the flowfield, which is highly turbulent, unsteady and vortical with flow separation over the sharp edges. In literature, there are several numerical studies investigating ship airwake with several computational methods. With these motivation for this complex problem, in my master thesis, I would like to concentrate on investigating the ship airwake with several turbulence models for SFS2 geometry and perform CFD simulations of two cases:

- Inclined flight deck effects

- Rotor / Ship airwake interactions

In this thesis, the Chapter 1 presents a general information about ship airwake study and literature review of ship airwake, Dynamic Interface and ship motion. In the Chapter 2, computational fluid dynamics analysis details are given. The information about steady-state and unsteady simulations with detailed information of computational domains are explained in this chapter. Also, governing equations and turbulence models are discussed. In the Chapter 3, validation process of ship airwake with several turbulence model and simulations results are given. Ship motion effect on ship airwake is explained in the Chapter 4. Ship motion due to sea waves for different sea states are discussed and steady-state and unsteady simulation results with inclined flight deck are given. In the Chapter 5, rotor validation in hover condition and simulation results including rotor disk downwash effect on ship airwake are presented. Finally, conclusion is made and future works are discussed in the Chapter 6.

CHAPTER 2

COMPUTATIONAL FLUID DYNAMICS ANALYSIS

The ship airwake is investigated on SFS2 in four different cases: horizontal (un-inclined) ship, inclined ship by 10 degree roll, horizontal (un-inclined) ship with rotor and inclined ship by 10 degree roll with rotor. Computations are conducted with freestream velocity of 30 knots (15.43 m/s) and WOD angle of 0 degree. SFS2 is an extended version of Simple Frigate Shape (SFS) with a pointed bow. In several ship airwake studies [13, 49], this geometry is used as the ship model. The flight deck is located behind the hangar structure. Although it is a relatively simple geometry to compute, it gives realistic results.

The rotor of Sikorsky S-76 helicopter is used as a rotor model in this study, which is a four-bladed, fully articulated rotor system. It is one of the most tested rotor systems with SC1095 and SC1095 R8 airfoils [59, 10, 45, 3]; therefore, there is a very large database available in the literature [57, 31, 22, 23, 21, 1, 28].

The computations are conducted using CFD++, which is a commercial CFD software. It provides users to generate steady-state and unsteady simulations for compressible and incompressible, laminar and turbulent flows in a large range of speed regimes including low speeds through subsonic, transonic, supersonic and hypersonic speeds. There are several turbulent models (RANS, hybrid, LES) available. Also, it allows very complex geometries to be solved by using any kind of cell types and all grids such as structured, unstructured, hybrid and overset. In addition, application of physics sources such as helicopter rotor is already included.

In this thesis, Implicit time integration method is used for steady-state simulations, while Explicit 4th order Runge-Kutta Method is used in unsteady computations with CFL number of 0.8.

2.1 Governing Fluid Dynamics Equations

In this sections, the governing equations that are used in computations by CFD solver are presented. In this thesis, compressible perfect gas Navier-Stokes equations are solved with standard atmospheric conditions. Since viscous flow is considered for computations with turbulence models, viscous terms exist in the Navier-Stokes equations. Also, turbulence model equations used in this study for closure of the governing equations are presented in the following sections.

2.1.1 Navier Stokes Equations

Three dimensional, unsteady, compressible and viscous flow motions can be described by Navier Stokes equations. Newton's second law is applied to fluid motion and the stress in the fluid is described as the sum of diffusing viscous term which is proportional to the velocity gradient and pressure term. In three-dimensional Cartesian coordinates, the Navier-Stokes equations can be written as:

$$\frac{\partial Q}{\partial t} + \frac{\partial}{\partial x}(F_1 + G_1)\frac{\partial}{\partial y}(F_2 + G_2) + \frac{\partial}{\partial z}(F_3 + G_3) = \dot{S} \tag{2.1}$$

On the other hand, Euler equations are for inviscid flows and therefore, viscous terms are not included. They are expressed as in the Equation 2.2.

$$\frac{\partial Q}{\partial t} + \frac{\partial}{\partial x}(F_1) + \frac{\partial}{\partial y}(F_2) + \frac{\partial}{\partial z}(F_3) = \dot{S} \tag{2.2}$$

In these equations, Q is vector of the dependent variable, $F1$, $F2$ and $F3$ are the inviscid flux vectors, $G1$, $G2$ and $G3$ are the viscous flux vectors and $\dot{S}$ is the source term. The source term is usually be zero unless physics source terms such as helicopter rotor model is used. Q, F's and G's are defined as follows:

$$Q = \begin{pmatrix} e \\ \rho \\ \rho u \\ \rho v \\ \rho w \end{pmatrix} \tag{2.3}$$

$$F_1 = \begin{pmatrix} (e+p)u \\ \rho u \\ \rho u^2 + p \\ \rho v u \\ \rho w u \end{pmatrix}, F_2 = \begin{pmatrix} (e+p)v \\ \rho v \\ \rho u v \\ \rho v^2 + p \\ \rho w v \end{pmatrix}, F_3 = \begin{pmatrix} (e+p)w \\ \rho w \\ \rho u w \\ \rho v w \\ \rho w^2 + p \end{pmatrix} \tag{2.4}$$

$$G_1 = \begin{pmatrix} \dot{q}_x - u\tau_{xx} - v\tau_{xy} - w\tau_{xz} \\ 0 \\ -\tau_{xx} \\ -\tau_{xy} \\ -\tau_{xz} \end{pmatrix} \tag{2.5}$$

$$G_2 = \begin{pmatrix} \dot{q}_y - u\tau_{yx} - v\tau_{yy} - w\tau_{yz} \\ 0 \\ -\tau_{yx} \\ -\tau_{yy} \\ -\tau_{yz} \end{pmatrix} \tag{2.6}$$

$$G_3 = \begin{pmatrix} \dot{q}_z - u\tau_{zx} - v\tau_{zy} - w\tau_{zz} \\ 0 \\ -\tau_{zx} \\ -\tau_{zy} \\ -\tau_{zz} \end{pmatrix} \tag{2.7}$$

where e is the total energy, ρ is the density, p is the pressure and u, v and w are the velocity components in the Cartesian coordinate respectively.

For a Newtonian fluid, the viscous stresses tensor components, τ_{ij}, in the viscous flux equations are the functions of velocity gradients:

$$\tau_{xx} = 2\mu\frac{\partial u}{\partial x} - \frac{2}{3}\mu\Phi \tag{2.8}$$

$$\tau_{yy} = 2\mu\frac{\partial v}{\partial y} - \frac{2}{3}\mu\Phi \tag{2.9}$$

$$\tau_{zz} = 2\mu\frac{\partial w}{\partial z} - \frac{2}{3}\mu\Phi \tag{2.10}$$

$$\tau_{xy} = \tau_{yx} = 2\mu(\frac{\partial u}{\partial y} + \frac{\partial v}{\partial x}) \tag{2.11}$$

$$\tau_{xz} = \tau_{zx} = 2\mu(\frac{\partial u}{\partial z} + \frac{\partial w}{\partial x}) \tag{2.12}$$

$$\tau_{yz} = \tau_{zy} = 2\mu(\frac{\partial w}{\partial y} + \frac{\partial v}{\partial x}) \tag{2.13}$$

where μ is the coefficient of viscosity and Φ is the dilatation. Dilatation is the gradient of velocity vector:

$$\Phi = \frac{\partial u}{\partial x} + \frac{\partial v}{\partial y} + \frac{\partial w}{\partial z} \tag{2.14}$$

The heat flux, $\dot{q}_i$, in the viscous flux equation can be written from Fourier's law of conduction by neglecting body forces and volumetric heating:

$$\dot{q}_x = -k\frac{\partial T}{\partial x} \tag{2.15}$$

$$\dot{q}_y = -k\frac{\partial T}{\partial y} \tag{2.16}$$

$$\dot{q}_z = -k\frac{\partial T}{\partial z} \tag{2.17}$$

where k is the thermal conductivity. In computations, air is approached as an ideal gas. The equation of state for a perfect gas is given as:

$$P = \rho RT \tag{2.18}$$

The Navier-Stokes equations are very difficult to solve analytically since equations are coupled. Therefore, various turbulence models have been suggested to close the system. In this thesis, Realizable $k - \epsilon$ turbulence model and Limited Numerical Scale (Hybrid RANS/LES turbulence model) are used. When a turbulence model is activated, extra transport equations are added to equations. Also, the viscosity in the above equations will written as $\mu + \mu_t$ and the thermal conductivity as $k + k_t$.

2.1.2 Realizable $k - \epsilon$ Turbulence Model

Realizable $k - \epsilon$ model is a modified version of standard $k - \epsilon$ turbulence model. As in the standard model, two transport equations are solved. One is for turbulent kinetic energy, k, and other one is for the dissipation of kinetic energy, ϵ. In CFD++'s Realizable $k-\epsilon$ model, the Boussinesq relation is used on obtain Reynolds-stresses(algebraically) from the modelled eddy viscosity (μ_i) and the available mean-strain tensor:

$$\rho\overline{u_i u_j} = \frac{2}{3}\delta_{ij}\rho k - \mu_i S_{ij}, \tag{2.19}$$

where

$$S_{ij} = \left(\frac{\partial U_i}{\partial x_j} + \frac{\partial U_j}{\partial x_i} - \frac{2}{3}\frac{\partial U_k}{\partial x_k}\delta_{ij}\right). \tag{2.20}$$

The model consists of the following transport equations for k and ϵ:

$$\frac{\partial(\rho k)}{\partial t} + \frac{\partial}{\partial x_j}(U_j \rho k) = \frac{\partial}{\partial x_j}\left[\left(\mu + \frac{\mu_t}{\sigma_k}\right)\frac{\partial k}{\partial x_j}\right] + P_k - \rho\epsilon, \tag{2.21}$$

$$\frac{\partial(\rho\epsilon)}{\partial t}+\frac{\partial}{\partial x_j}(U_j\rho\epsilon)=\frac{\partial}{\partial x_j}\left[\left(\mu+\frac{\mu_t}{\sigma_\epsilon}\right)\frac{\partial\epsilon}{\partial x_j}\right]+(C_{\epsilon1}P_k-C_{\epsilon2}\rho\epsilon+E)T_t^{-1}, \quad (2.22)$$

in which the rate of production of turbulence energy, $P_k = -\rho\overline{u_iu_j}\partial U_i/\partial x_j$, T_t is a realizable estimate of the turbulence timescale:

$$T_t=\frac{k}{\epsilon}max\{1,\zeta^{-1}\},\ \zeta=\sqrt{R_t/2}, \quad (2.23)$$

and the turbulence Reynolds number, $R_t = \rho k^2/(\mu\epsilon)$. A new term, E, is added to the dissipation-rate equation in order to improve the model response to adverse pressure-gradient flows. This term is expressed as:

$$E=A_E\rho\sqrt{\epsilon T_t}\Psi max\{k^{\frac{1}{2}},(\nu\epsilon)^{\frac{1}{4}}\},\ \Psi=max\{\frac{\partial k}{\partial x_j}\frac{\partial\tau}{\partial x_j},0\},\ \tau=k/\epsilon. \quad (2.24)$$

The model constants are given by:

$$C_\mu=0.09,\ C_{\epsilon1}=1.44,\ C_{\epsilon2}=1.92,\sigma_k=1.0,\ \sigma_\epsilon=1.3,\ A_E=0.3.$$

The eddy viscosity, μ_t, is obtained from:

$$\mu_t=min\{C_\mu f_\mu\rho k^2/\epsilon,\phi\frac{\rho k}{S}\} \quad (2.25)$$

$$\phi=\begin{cases}2/3, & \text{Schwatz}\\ 0.31, & \text{Bradshaw}\end{cases} \quad (2.26)$$

where $S = \sqrt{S_{kl}S_{kl}/2}$ is the dimensional strain magnitude and f_μ is a low-Reynolds number function, designed to account for viscous and inviscid damping of turbulent fluctuations close to solid surfaces:

$$f_\mu=\frac{1-exp^{-0.0084R_t}}{1-exp^{-\sqrt{R_t}}}max\{1,\left(\frac{2}{R_t}\right)^{\frac{1}{2}}\} \quad (2.27)$$

This $k - \epsilon$ model can be integrated directly to walls for fine meshes or used with wall functions application to coarse grids.

2.1.3 Limited Numerical Scale

Limited Numerical Scale is a hybrid turbulence model which blends automatically statistical Reynolds-Averaged Navier-Stokes (RANS) closures with an anisotropic form of Smagorinsky Large-Eddy Simulation (LES) methods in finer grids. As RANS equations, Cubic $k - \epsilon$ equations which is one of the two-equation turbulence model are solved.

In Cubic $k - \epsilon$ model, transport equations are given as in the Realizable $k - \epsilon$ model [39]:

$$\frac{\partial(\rho k)}{\partial t} + \frac{\partial}{\partial x_j}(U_j \rho k) = \frac{\partial}{\partial x_j}\left[\left(\mu + \frac{\mu_t}{\sigma_k}\right)\frac{\partial k}{\partial x_j}\right] + P_k - \rho\epsilon, \tag{2.28}$$

$$\frac{\partial(\rho \epsilon)}{\partial t} + \frac{\partial}{\partial x_j}(U_j \rho \epsilon) = \frac{\partial}{\partial x_j}\left[\left(\mu + \frac{\mu_t}{\sigma_\epsilon}\right)\frac{\partial \epsilon}{\partial x_j}\right] + (C_{\epsilon 1} P_k - C_{\epsilon 2}\rho\epsilon + E)T_t^{-1}, \tag{2.29}$$

The difference between Realizable and Cubic(non-linear) $k - \epsilon$ turbulence models is the calculation of Reynolds stress tensor.

$$\begin{aligned}
\rho\overline{u_i u_j} = {} & \rho\frac{2}{3}kS_{ij} - \mu_t S^*_{ij} + c_1\frac{\mu_t k}{\epsilon}\left(S^*_{ik}S^*_{kj} - \frac{1}{3}S^*_{kl}S^*_{kl}S_{ij}\right) \\
& + c_2\frac{\mu_t k}{\epsilon}\left(\Omega_{ik}S^*_{kj} + \Omega_{jk}S^*_{ki}\right) + c_3\frac{\mu_t k}{\epsilon}\left(\Omega_{ik}\Omega_{jk} - \frac{1}{3}\Omega_{lk}\Omega_{lk}S_{ij}\right) \\
& + c_4\frac{\mu_t k^2}{\epsilon^2}\left(S^*_{ki}\Omega_{lj} + S^*_{kj}\Omega_{li}\right)S^*_{kl} \\
& + c_5\frac{\mu_t k^2}{\epsilon^2}\left(\Omega_{il}\Omega_{lm}S^*_{mj} + S^*_{il}\Omega_{lm}\Omega_{mj} - \frac{2}{3}S^*_{lm}\Omega_{mn}\Omega_{nl}S_{ij}\right) \\
& + c_6\frac{\mu_t k^2}{\epsilon^2}S^*_{ij}S^*_{kl}S^*_{kl} + c_7\frac{\mu_t k^2}{\epsilon^2}S^*_{ij}\Omega_{kl}\Omega_{kl}
\end{aligned} \tag{2.30}$$

$$S^*_{ij} = \left(\frac{\partial U_i}{\partial x_j} + \frac{\partial U_j}{\partial x_i}\right) \tag{2.31}$$

$$\Omega_{ij} = \left(\frac{\partial U_i}{\partial x_j} - \frac{\partial U_j}{\partial x_i}\right) \quad (2.32)$$

$$S = \frac{k}{\epsilon}\sqrt{\frac{1}{2}S^*_{ij}S^*_{ij}} \quad (2.33)$$

$$\Omega = \frac{k}{\epsilon}\sqrt{\frac{1}{2}\Omega^*_{ij}\Omega^*_{ij}}. \quad (2.34)$$

The time scale is defined as:

$$T_t = \frac{k}{\epsilon}max\{1, \xi^{-1}\}, \quad (2.35)$$

where $\xi = \sqrt{R_t}/C_\tau$, with $R_t = k^2/(\nu\epsilon)$ and $C_\tau = \sqrt{2}$.

The eddy viscosity in the transport equations is calculated as follows:

$$\mu_t = C_\mu f_\mu \rho k^2/\epsilon \quad (2.36)$$

The remaining model parameters are:

$$C_{\mu SZL} = \frac{2/3}{A_1 + S + 0.9\Omega},\ C_{\mu G} = min\{\frac{0.09 + 0.13\phi}{1 + \phi^{2.5}},\ C_{\mu SZL}\}, \quad (2.37)$$

$$\phi = \|\Omega - S\|,\ c_1 = \frac{3/4}{(1000 + S^3)C_\mu},\ c_2 = \frac{15/4}{(1000 + S^3)C_\mu}, \quad (2.38)$$

$$c_3 = \frac{-19/4}{(1000 + S^3)C_\mu},\ c_4 = -10C_\mu^2,\ c_5 = 0,\ c_6 = -2C_\mu^2,\ c_7 = -c_6 \quad (2.39)$$

and

$$f_\mu = \frac{1 - e^{-A_\mu R_t}}{1 - e^{-\sqrt{R_t}}}max\{1, \xi^{-1}\} \quad (2.40)$$

Expressions of E, Ψ and τ terms are given as in the previous section in which Realizable $k-\epsilon$ model is explained.

$$E = A_{E_\tau}\rho max[k^{\frac{1}{2}},(\nu\epsilon)^{\frac{1}{4}}]\sqrt{\epsilon T_t}\Psi_\tau, \tag{2.41}$$

$$\Psi_\tau = max\left\{\frac{\partial k}{\partial x_j}\frac{\partial \tau}{\partial x_j}\right\},\ \tau = \frac{k}{\epsilon}. \tag{2.42}$$

The model constants are given by:

$$A_1 = 1.25,\ C_{e1} = 1.44,\ C_{e2} = 1.92, \sigma_k = 1.0,$$

$$\sigma_e = 1.3,\ A_\mu = 0.0085, A_{E_\tau} = 0.15,\ C_s = 0.05.$$

Blending process between RANS and LES models is conducted by adjusting the modeled stress tensor according to a latency parameter.

$$\overline{u_i u_j} = \alpha \overline{u_i u_j}^M, \tag{2.43}$$

Here, $\overline{u_i u_j}^M$ is the Reynolds stress tensor obtained by RANS equations. Latency parameter is the ratio of minimum of characteristic length-scale/velocity-scale product of turbulence models and characteristic length-scale/velocity-scale product of RANS model.

$$\alpha = min(LV_{LES}, LV_{RANS})/LV_{RANS} \tag{2.44}$$

By introducing the product of characteristic length-scale/velocity-scale of selected RANS and LES models, latency parameter expression becomes:

$$\alpha = min\left\{C_s(L_i^\Delta)^2\sqrt{S_{kl}^* S_{kl}^*/2}, C_\mu k^2/\epsilon + \delta\right\}\left(C_\mu k^2/\epsilon + \delta\right)^{-1} \tag{2.45}$$

2.2 Unstructured Grid

The unstructured grids are used for full scale SFS2 geometry due to their capability of resolving the complex structures and simplicity to generate. The grids are generated by using Pointwise grid generation software [47]. A fairly uniform grid surface on the ship is generated because the time step is determined according to the minimum cell size by using explicit time scheme. However, smaller triangular cells are preferred on the surface corresponding to flight deck in order to get finer grids in the region above the deck. In the Figure 2.1, the computational domain can be seen. The detailed mesh of the ship surface is given in the Figure 2.2

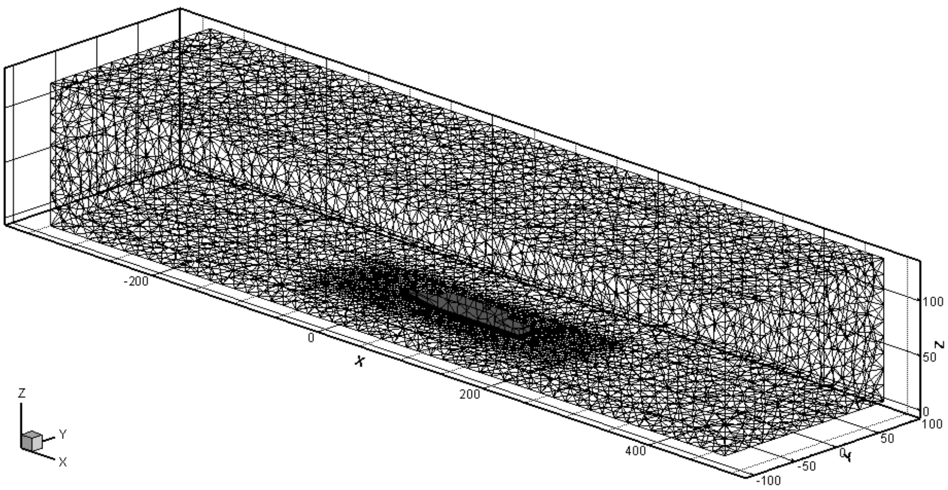

Figure 2.1: Computational Domain

The full scale SFS2 geometry used in the simulations has length of 140 m, and width of approximately 14 m. The flight deck is 4.5 m above the sea level and the height of the hangar structure is approximately 11 m [13, 49]. The domain extends 2.5 times of the ship length behind and in front the ship, while the side walls of the outer domain lie between 7 times of the ship width from the centerline. The computational domain has 1028 K tetrahedral grid cells. The bottom surface of the domain refers to the sea surface. The upper surface is approximately 12 times the hangar height above the bottom surface. In the Figure 2.3, the mesh around the ship geometry is presented.

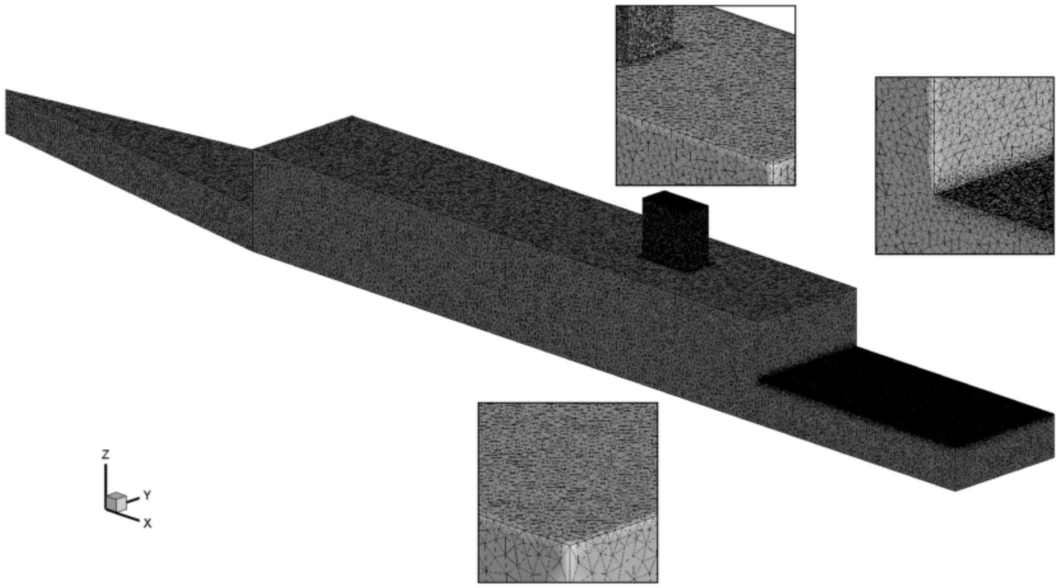

Figure 2.2: Mesh of the SFS2 standart ship model (horizontal)

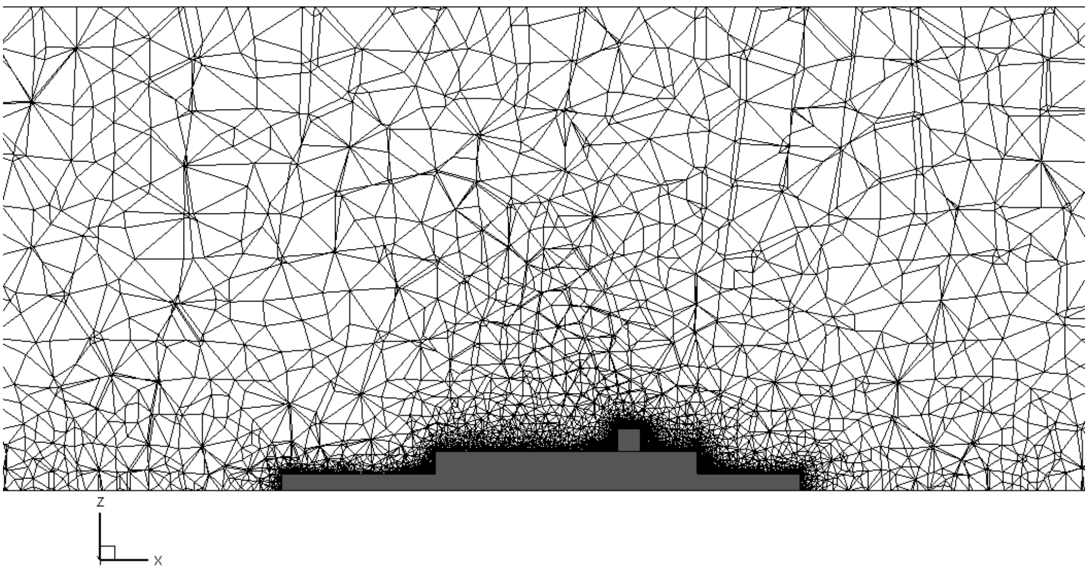

Figure 2.3: Zoomed view of mesh on the centerline slice

Inclined flight deck is an important factor for the helicopter's shipboard operations. Therefore, the ship model is given a roll angle of 10 degree about the x axis. On the ship surface and other five surfaces of the domain, the same grid size as previous computations is given. The new computational domain can be seen in 3-D view in Figure 2.4. The new computational domain contains approximately 778 K grid cells.

The back view is given with comparison to the standard ship in Figure 2.5.

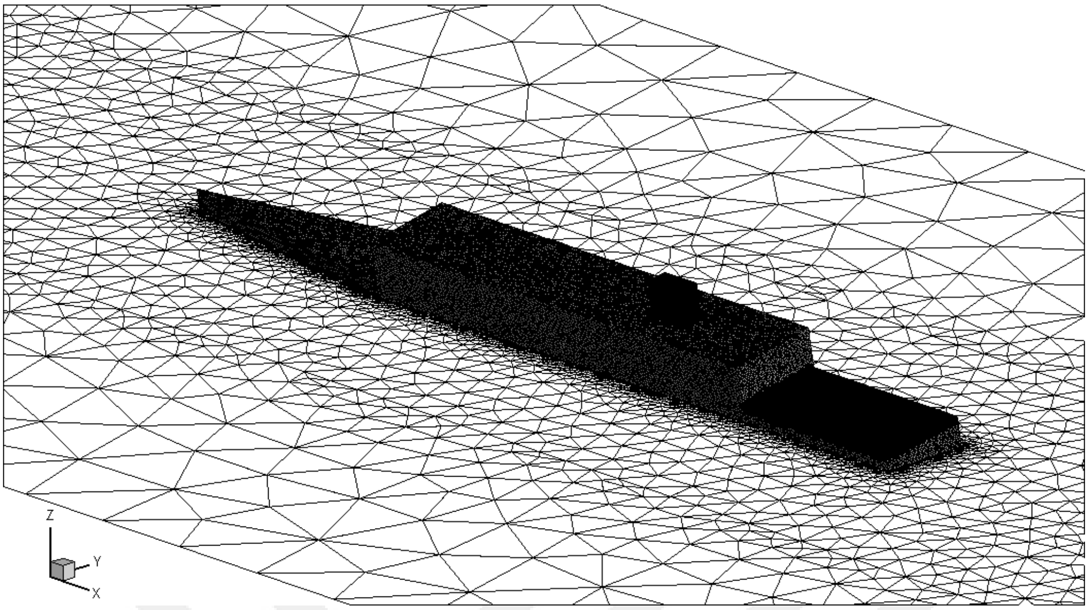

Figure 2.4: Mesh of the inclined SFS2 ship model

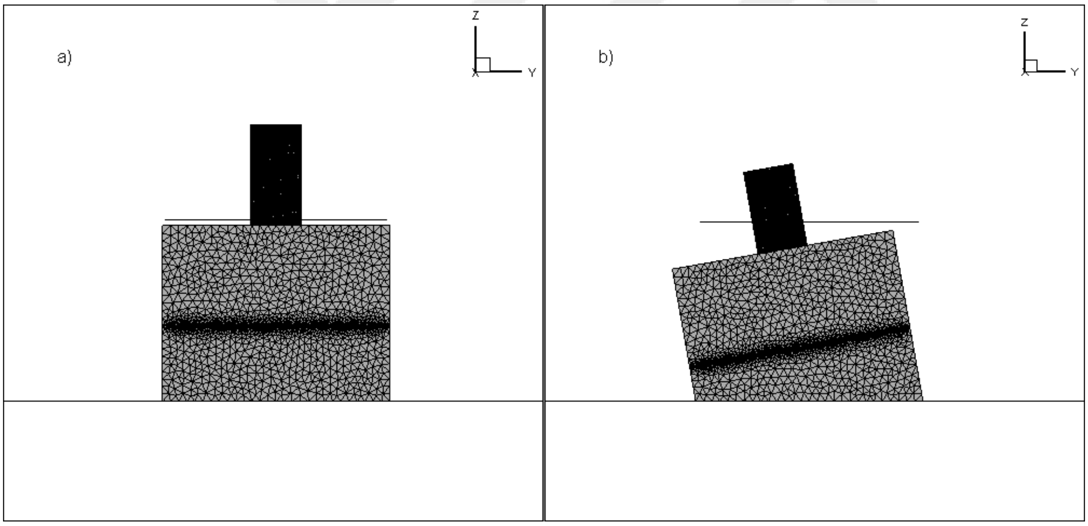

Figure 2.5: a) Standart (horizontal) SFS2 ship model b) Inclined SFS2 ship model

In order to investigate the rotor downwash effect on ship airwake, as the importance of the interactions is mentioned in the previous sections, a rotor disk model is added to the domain. The position of the disk in the first combination (horizontal ship) is chosen as mid-deck at 11 m above the waterline. The location of the rotor disk is kept unchanged for the other combination (inclined ship). While the domain with disk on the plane ship has 1550 K number of grid cells, the combination of inclined ship and

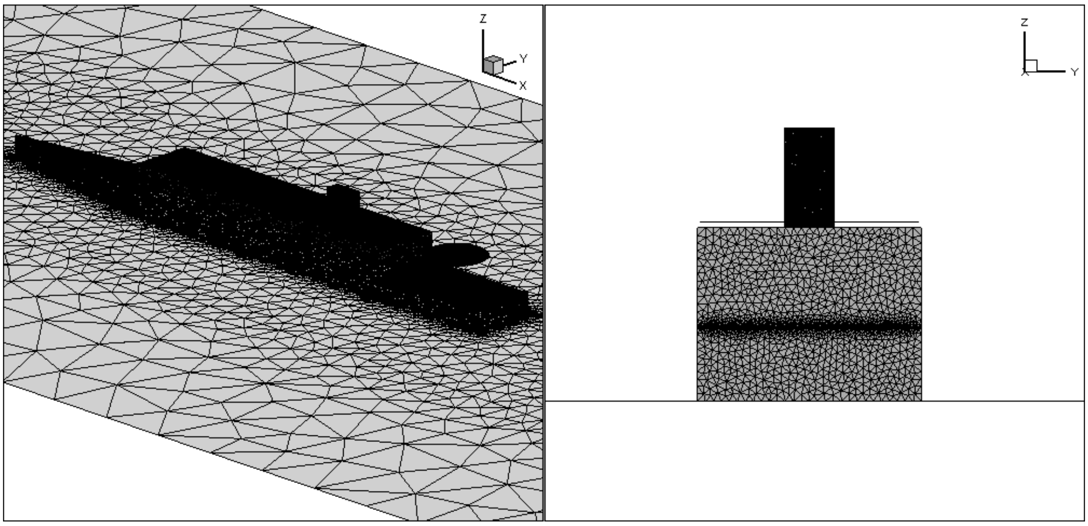

Figure 2.6: Horizontal SFS2 ship model with rotor disc

disk geometry contains 1500 K grid cells. The unstructured meshes are shown for two combinations in Figure 2.6 and 2.7, respectively.

In all computations except horizontal flight deck case with Euler method, no slip boundary condition is used for the ship's surface. In Euler, the slip boundary condition is applied to ship surface, therefore wall function is not required to the walls. On the other hand, Advanced two layer wall function in equilibrium mode is applied to ship surface in all computations with slip wall boundary condition. Slip condition is used for the sea surface which is bottom surface of the domain. The characteristic-based farfield boundary condition is used on the outer domains, hereby any reflection is avoided from side walls.

2.3 Parallel Computing

The computations are performed by using the Poyraz HPC Cluster at the Dept of Aerospace Engineering/RÜZGEM in METU. Poyraz HPC Cluster has eight nodes, each with four AMD Opteron 6276 2.3 GHz central processing units (CPU) which has sixteen cores and 32 MB RAM per CPU, 256 GB DDR3, 1333 MHz 8 GB dual in-line memory module (DIMM) and it is using 10 gigabit ethernet (GBE) connection with total 512 cores, 2 TB memory and 20 TB storage capacity. The operating system

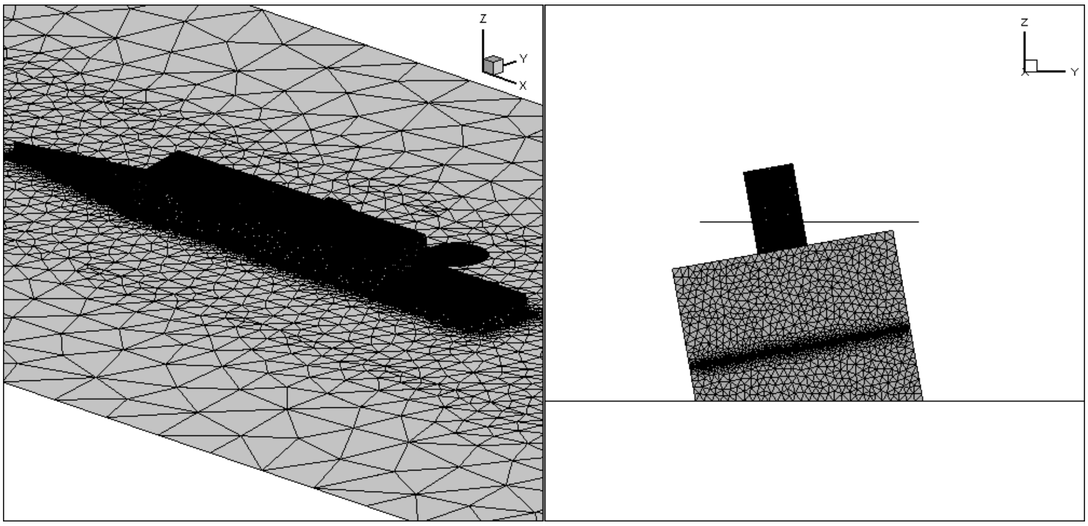

Figure 2.7: Inclined SFS2 ship model with rotor disc

is Centos/Scientific Linux. The computations for this study are performed on 16 or 64 cores.

CHAPTER 3

SHIP AIRWAKE SIMULATIONS

3.1 Introduction

The CFD simulations are performed for four cases, the ships that are horizontal and inclined and the ships with rotor model that are again horizontal and inclined. The results are presented and discussed below. The ship airwake studies are independent of Mach Number. In other words, flows with different speeds do not have different characteristics in terms of nondimensional flow characterstics which was also stated by Zhang et al. [69]. Therefore, ship airwake studies are compared in terms of non-dimensionalized velocities by free-stream speeds. Also, it is assumed that airwake does not depend on Reynolds number. Because ship geometry consists of sharp edges and steep bodies, the flow is full of separation. In addition, it is a grid independent case. As mentioned in the next section, a grid study is conducted and it is observed that none of them offers a better solution.

3.1.1 Grid Independence Study

Firstly, the ship airwake studies are performed to test the grid independence of the computations. Grid cells are changed from a base cell size by multiplying and dividing a factor 2. There are three different meshes as follows: Grid A (535K), Grid B (1028K) and Grid C (3231K). In here, Grid B is the base grid. These grids are used in steady-state computations with Realizable $k - \epsilon$ turbulence model. Computations are performed with 15.43 m/s freestream velocity and 0 WOD angle. The results are compared with respect to mean velocity distribution over the flight deck at hangar height. The velocity distribution is given in Figure 3.1. The velocity magnitudes and lateral distances are non-dimensionalized with free-stream velocity and ship beam respectively. The figure also includes the experimental wind tunnel data. It can be seen that difference between the results of study are very small. None of the grids offer a better solution.

Time step for the unsteady simulations decreases as cell size gets smaller. In other words, it varies linearly with grid spacing. For this case, more computational time is required for Grid C. On the other hand, Grid A needs larger time step and the mean velocity distribution over the flight deck are also satisfactory with respect to other grids. However, such a larger time step may cause to lose unsteadiness of flow and unsteady nature cannot be observed with the coarser grid due to its poor mesh quality.

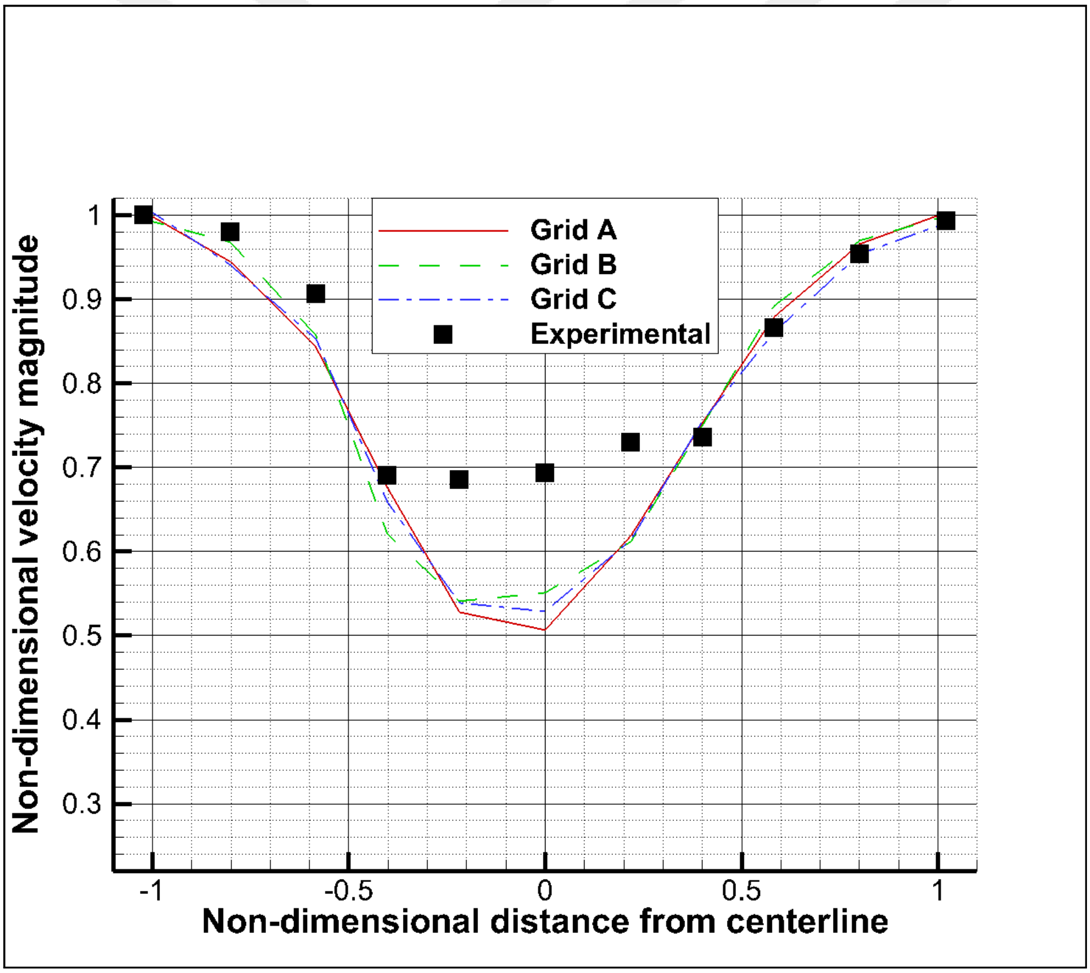

Figure 3.1: Comparison of velocity distribution over the flight deck for three different grids

In comparisons, Grid B seems to give promising results with smaller time consumption with respect to Grid C. Therefore, Grid B is selected for further computations. In inclined ship case and simulations with rotor disk, this grid is used as base. However, it is hard to conduct a grid independence study for unstructured grids, since even if mesh is fine on the surface of ship, grid size is getting coarser as grid cells are away from walls. Therefore, more systematic study is needed for preparation of validation guideline for such problems. For example, finer grids for unsteady solutions can be tried if computational cost is allowed and wake grid clustering can be tried separately to capture more smaller scales in the flow.

3.2 Computations with Different Turbulence Models

In the literature, there are many different turbulence models used in the ship airwake computations, as mentioned Chapter 1. In order to decide which model is appropriate for SFS2 ship model, a model study is also conducted. In this study, RANS turbulence models; Realizable $k-\epsilon$, Realizable $k-\omega$ and SST; Hybrid turbulence models such as DES97 (DES with one equation Spalart Allmaras) and LNS-Limited Numerical Scale (Batten and Goldberg's hybrid RANS/LES) models are taken into account. These models are compared in terms of mean velocity distribution over the flight deck and their computational cost for unsteady simulations. Mean velocity comparison is done for steady-state simulations of 2500 iterations. As a result, Realizable $k-\epsilon$ and LNS showed good agreement with experimental data when considering flow topology over the flight deck.

Also, the Figure 3.2 shows that Realizable $k-\epsilon$ and LNS methods are cheaper than DES97. Despite the fact that computational cost of Realizable $k-\omega$ and SST models are less than the others, they are weak to obtain flowfield characteristics of ship airwake.

As a result, Realizable $k-\epsilon$ and LNS turbulence models are selected for this study. Their steady-state and unsteady results are compared with experimental data and they are discussed in the next sections.

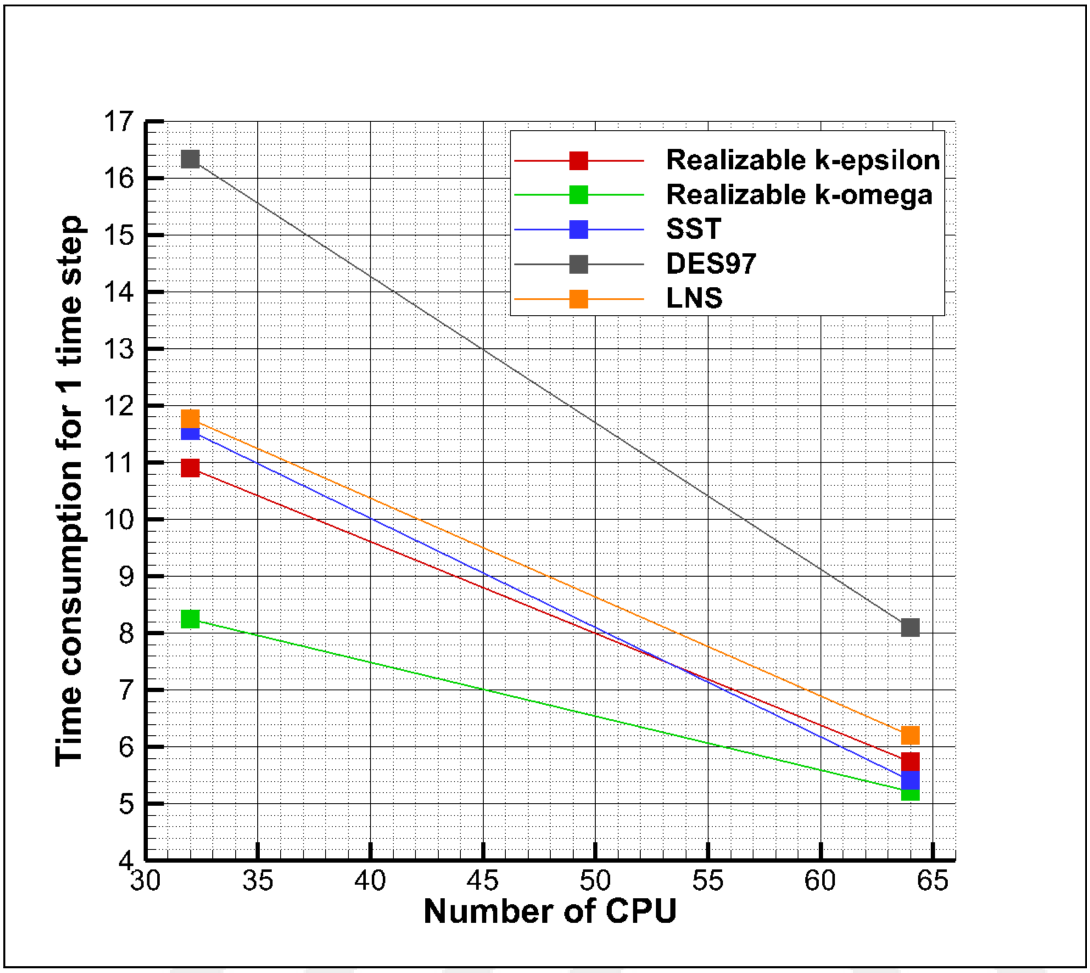

Figure 3.2: Comparison of time consumptions of turbulence models for 1 time step

3.3 Results for Standard Ship and Validations

In this study, ship airwake over SFS2 is investigated by using Realizable $k-\epsilon$ which is two-equation turbulence model and hybrid RANS/LES turbulence models and they are compared.

3.3.1 Computational Results for Realizable $k-\epsilon$ Turbulence Model

In this part of the study, results obtained by Realizable $k-\epsilon$ turbulence model are presented for both steady-state and unsteady simulations. The steady-state computations are performed over 2500 iterations at which momentum residuals are allowed to decrease in 3 order. Unsteady simulations starts from the steady-state. In unsteady simulations, the turbulence equations are solved after 2500 iterations, which makes computations laminar before 2500 iterations.

In Figure 3.3, the steady-state simulation result is given. In this figure, flow topology over flight deck can be observed. In Figure 3.5, the surface flow topology obtained by experiments [41] is presented. As it is seen that steady-state RANS equations are successful to obtain the main characteristics of flowfield. Location of the vortex cores, which are called horseshoe vortex cores are similar to each other. In Figure 3.4, flow on vertical slice through ship centerline is illustrated. In Figure 3.6 and Figure 3.7 , results obtained by PIV method in the experiments are presented. Experiments are conducted with freestream velocity of 20 m/s. It can be seen a some asymmetry in flowfield despite the symmetric structure of SFS2. Also, magnitude of the vortex cores are observed as different. On vertical slice, the location of recirculation zone is similar while magnitude of vortices are different.

Steady-state Realizable $k-\epsilon$ simulations provides us to understand general behaviour of flow behind hangar over the flight deck. There are two vortex cores named as horseshoe vortices on the flight deck surface and recirculation zone due to sharp edges of hangar structure. After separation, flow reattaches again to surface at middle of flight deck. This illustrations show downward flow at hangar height and mid-deck, where the helicopter rotor is located while hovering.

After steady-state simulations, unsteady computations are performed by using Realizable $k - \epsilon$. Unsteady simulations are initialized laminar steady-state as applied to unsteady hybrid RANS/LES simulations. Simulation results are time averaged. In Figure 3.8 and in Figure 3.10, mean velocity vectors and streamlines can be observed with contour plots over flight deck. The result is presented on a horizontal slice at half hangar height. In Figure 3.11, streamlines of time averaged unsteady simulations on the centerline slice is presented. It can be observed that unsteady RANS is very good to reflect the main characteristics of airwake behind the hangar structure as in experiments. The asymmetric nature of flow over the flight deck can be observed. Also, the velocity magnitudes are in good agreements with respect to non-dimensional values.

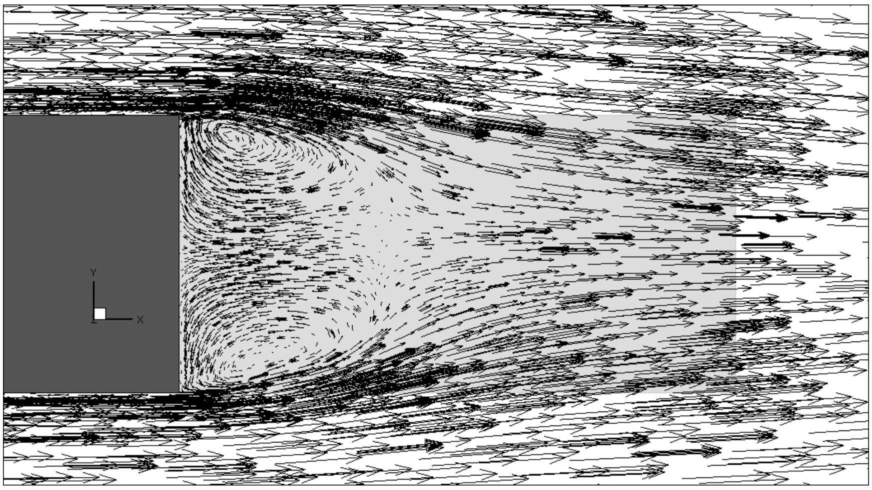

Figure 3.3: Flow topology over the flight deck for a horizontal slice 7.5 m above sea level

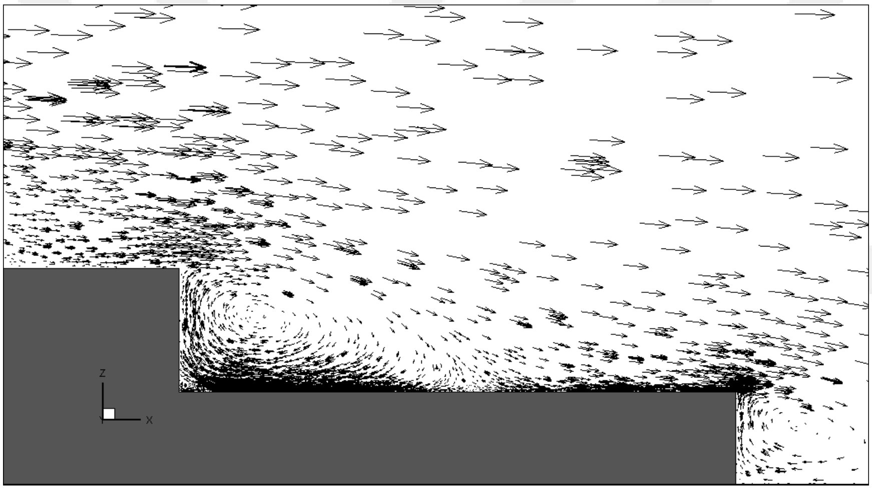

Figure 3.4: Flow topology over the flight deck for a vertical slice at centerline of ship

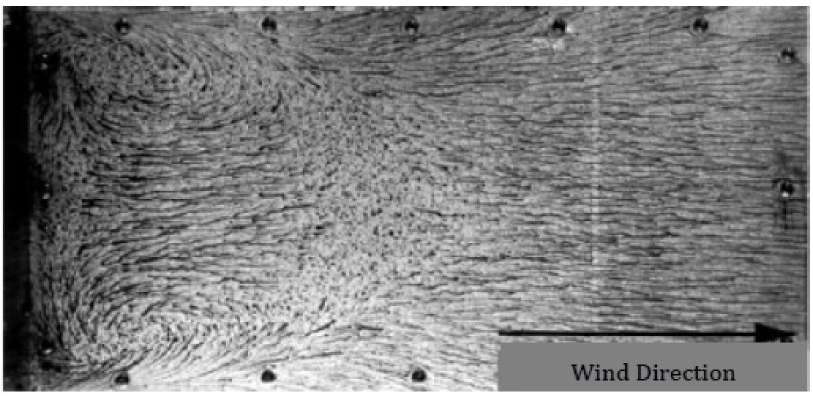

Figure 3.5: Flow topology over the flight deck [41]

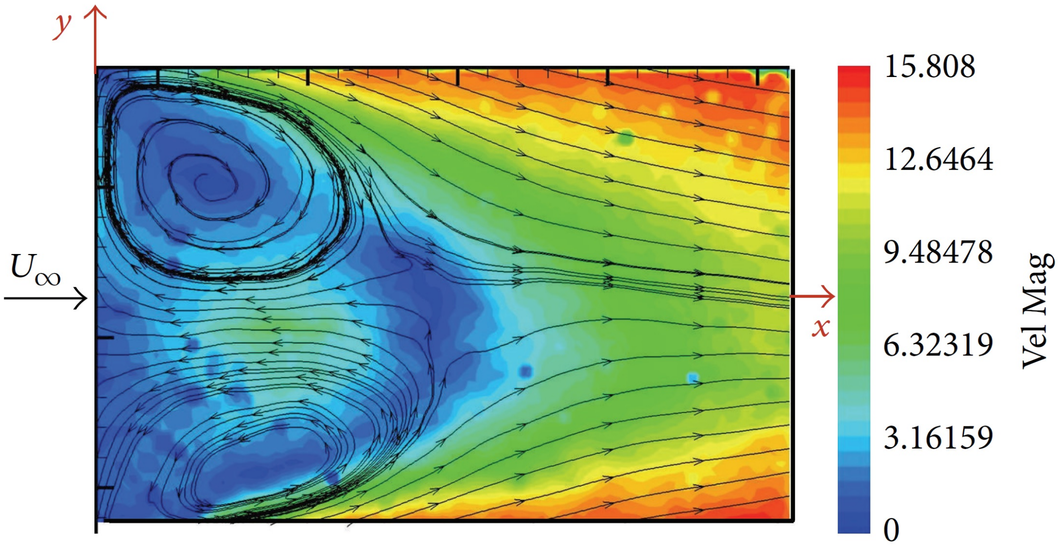

Figure 3.6: Flow velocity magnitude contour of experiments at half hangar height [41]

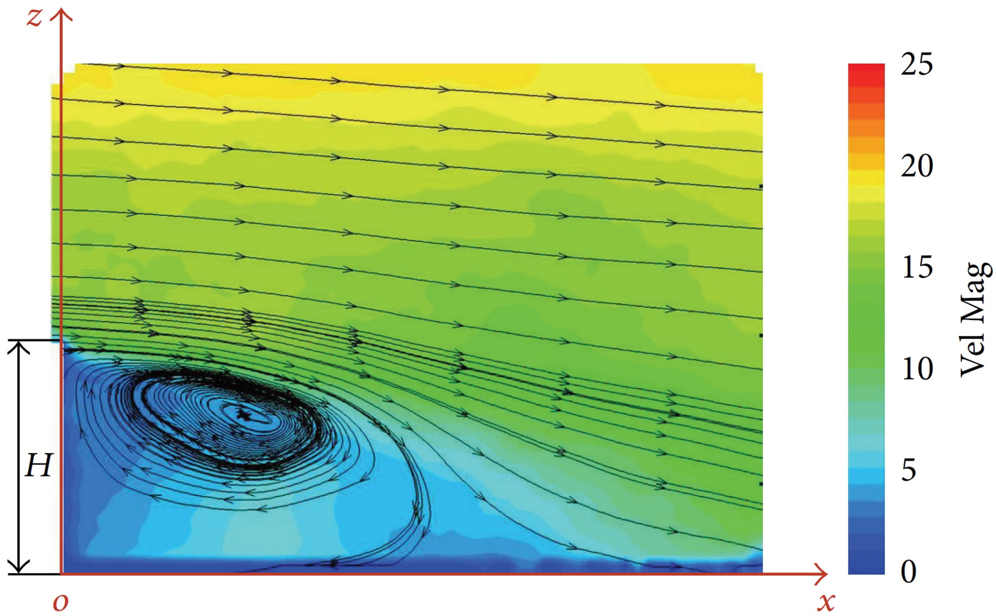

Figure 3.7: Flow velocity magnitude contour of experiments on the centerline [41]

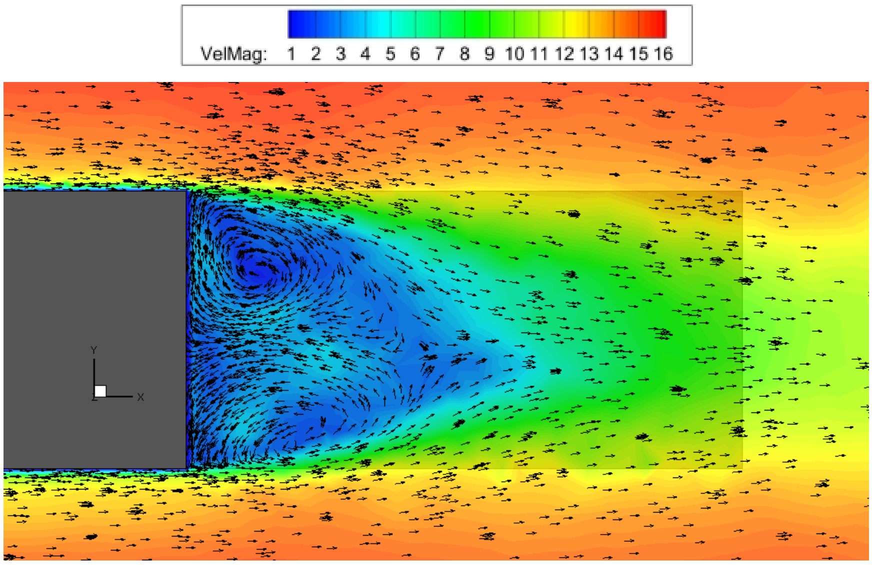

Figure 3.8: Velocity contour and velocity vector plots of unsteady Realizable $k - \epsilon$ on horizontal slice at half hangar height

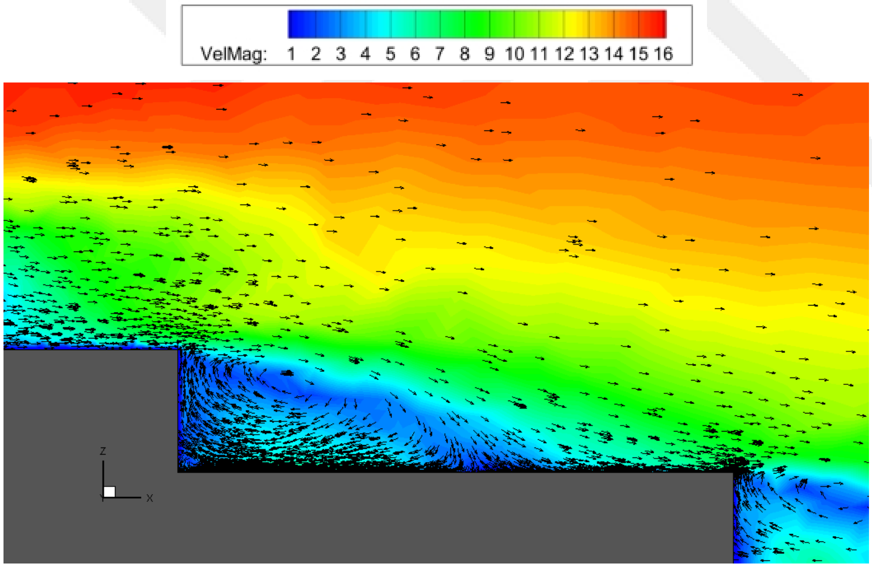

Figure 3.9: Velocity contour and velocity vector plots of unsteady Realizable $k - \epsilon$ on vertical slice along ship centerline

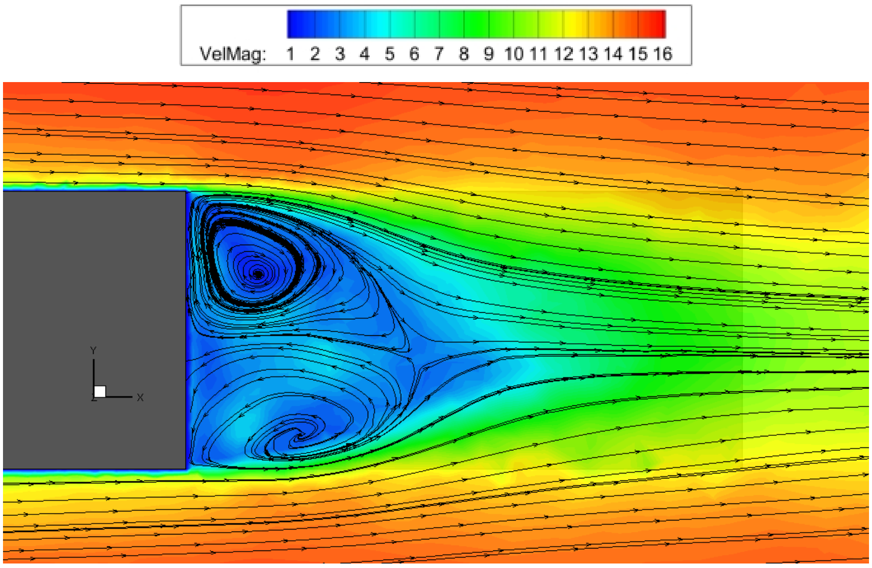

Figure 3.10: Streamlines over flight deck of unsteady Realizable $k - \epsilon$ on horizontal slice at half hangar height

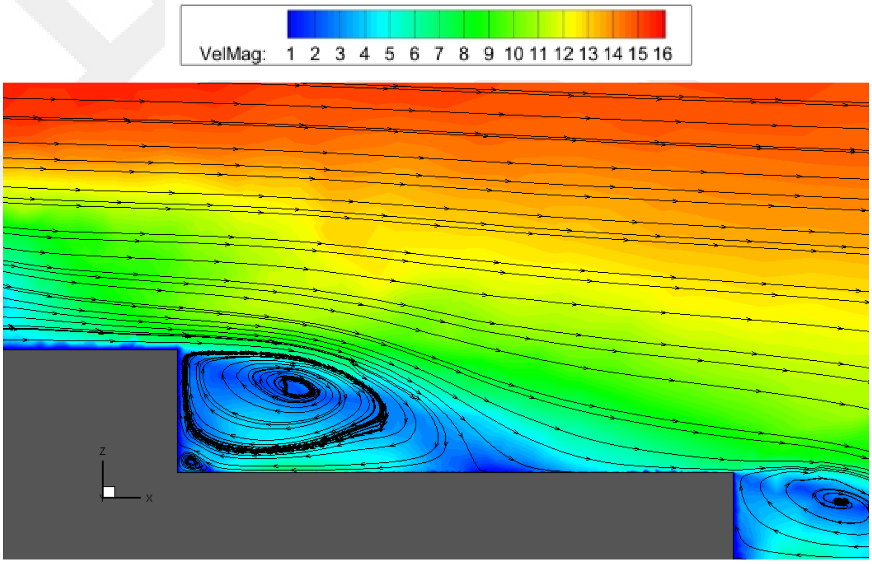

Figure 3.11: Streamlines over flight deck of unsteady Realizable $k - \epsilon$ on vertical slice along ship centerline

After simulations of steady-state and unsteady RANS, hybrid RANS/LES turbulence model by Batten and Goldberg is used as turbulence model. As in Realizable $k - \epsilon$ case, simulations are performed both steady-state and unsteady. The results for steady-state simulations of hybrid RANS/LES is given in Figure 3.12 and in Figure 3.13. These figures show the streamtraces on horizontal slice at half hangar height and vertical slice at centerline respectively. It is observed that hybrid RANS/LES method is successful to obtain nature of flow behind the superstructures. Here, the magnitude of vortex cores are not obtained correctly, while locations of cores and recirculation zone are similar to experimental findings.

Besides of steady-state simulations, ship airwake analysis is investigated as unsteady simulations with hybrid RANS/LES turbulence model. Unsteady calculations are started from laminar steady-state simulation. The results are given in Figure 3.14 and Figure 3.15 in terms of mean velocity magnitude contour plots and vectors. The streamtraces over the flight deck behind the hangar are demonstrated in Figure 3.16 and in Figure 3.17 on horizontal slice and vertical slice respectively.

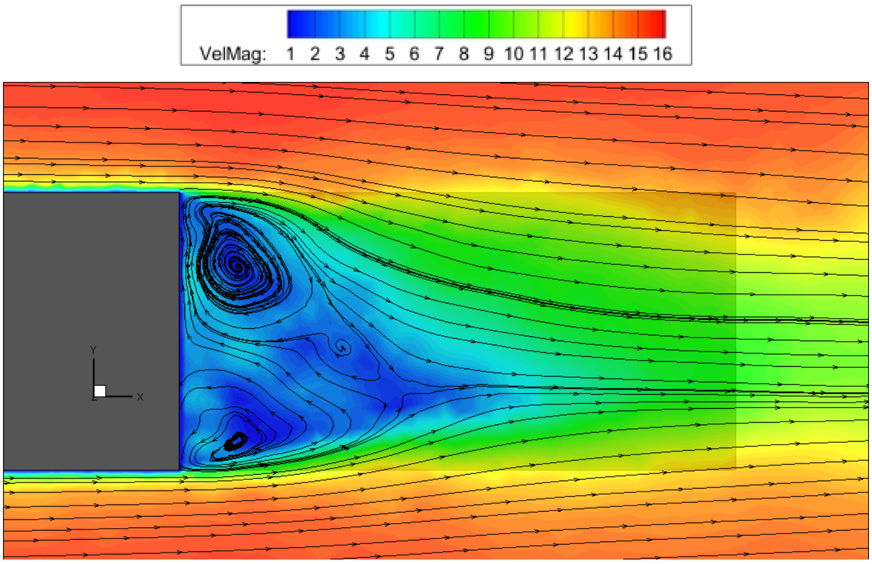

Figure 3.12: Streamlines over flight deck of steady-state hybrid RANS/LES on horizontal slice at half hangar height

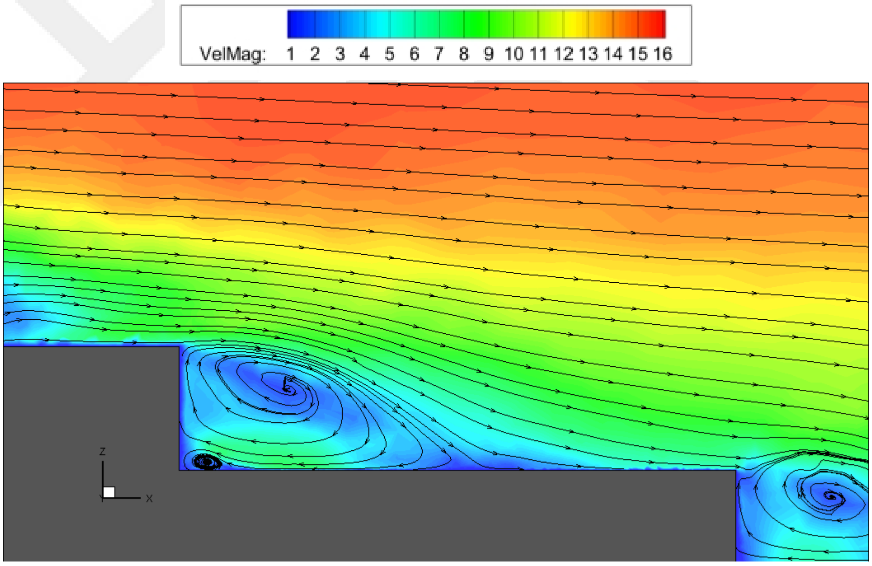

Figure 3.13: Streamlines over flight deck of steady-state hybrid RANS/LES on vertical slice at centerline

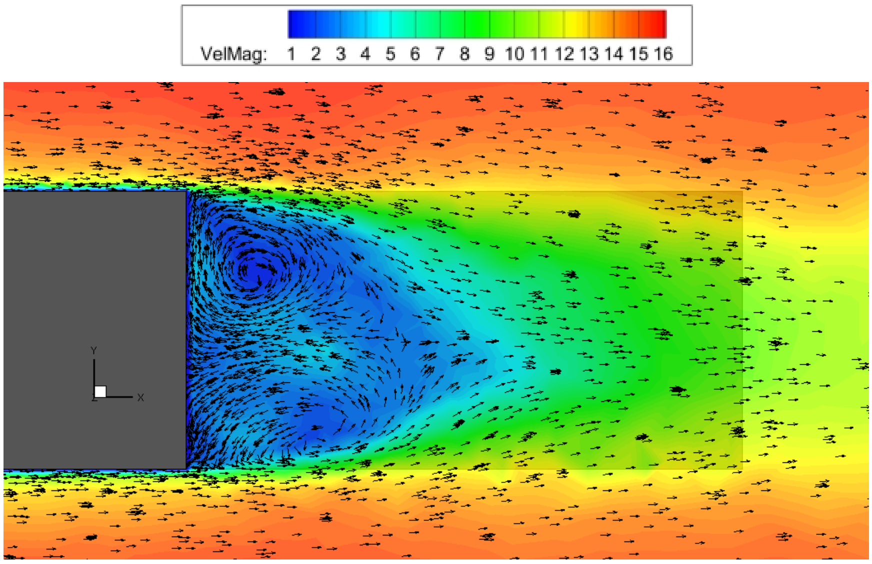

Figure 3.14: Velocity contour and velocity vector plots of unsteady hybrid RANS/LES on horizontal slice at half hangar height

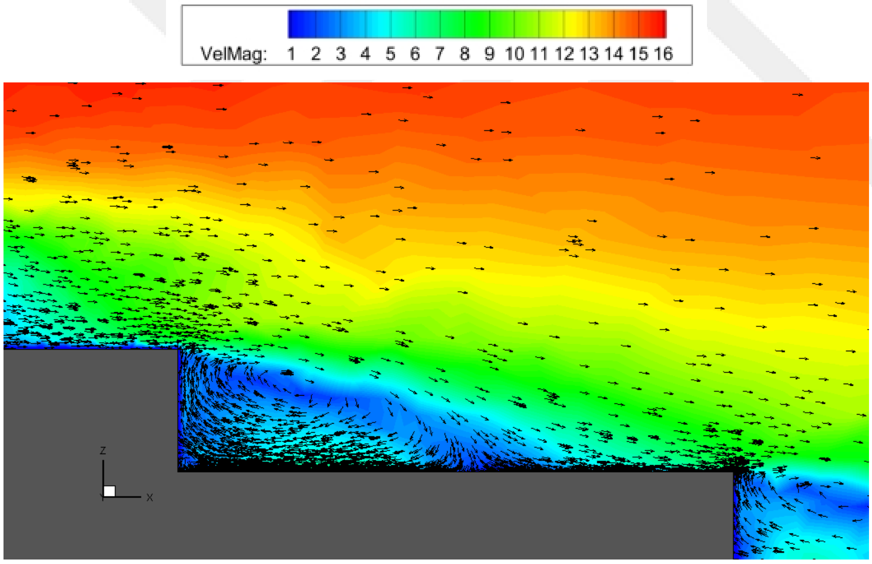

Figure 3.15: Velocity contour and velocity vector plots of unsteady hybrid RANS/LES on vertical slice at centerline

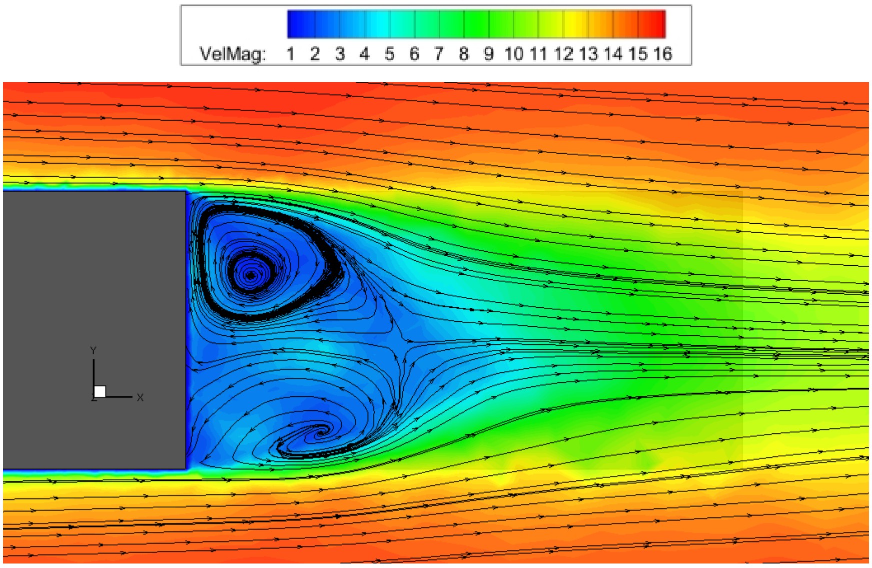

Figure 3.16: Streamline plots of unsteady hybrid RANS/LES on horizontal slice at half hangar height

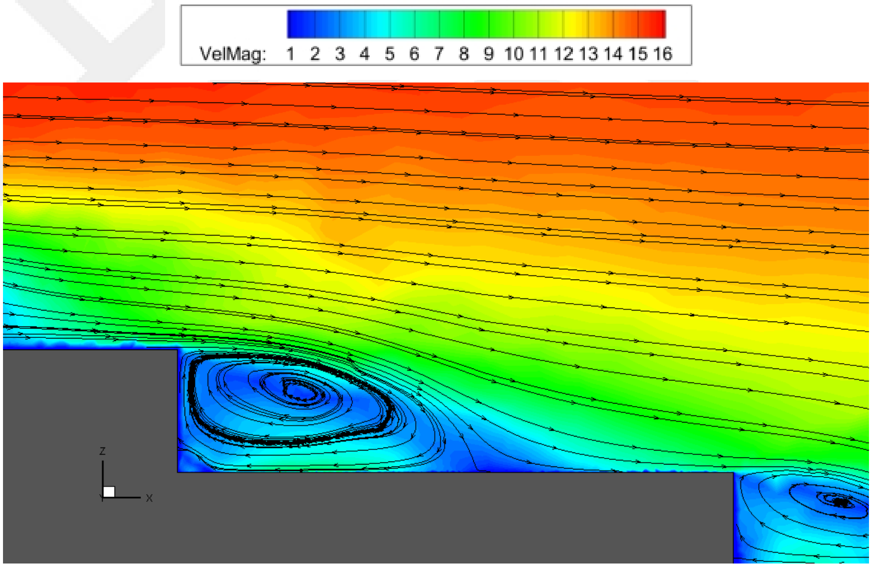

Figure 3.17: Streamline plots of unsteady hybrid RANS/LES on vertical slice at centerline

The velocity distribution of time averaged unsteady LNS simulation is presented in Figure 3.18. The velocity data is collected over the flight deck at hangar height and middle of the deck (125,0,11). The computational results are in good agreement with experimental findings presented by Zhang [69]. The results are averaged over a 25 second time range by neglecting the first 5-second period of 30-second simulation.

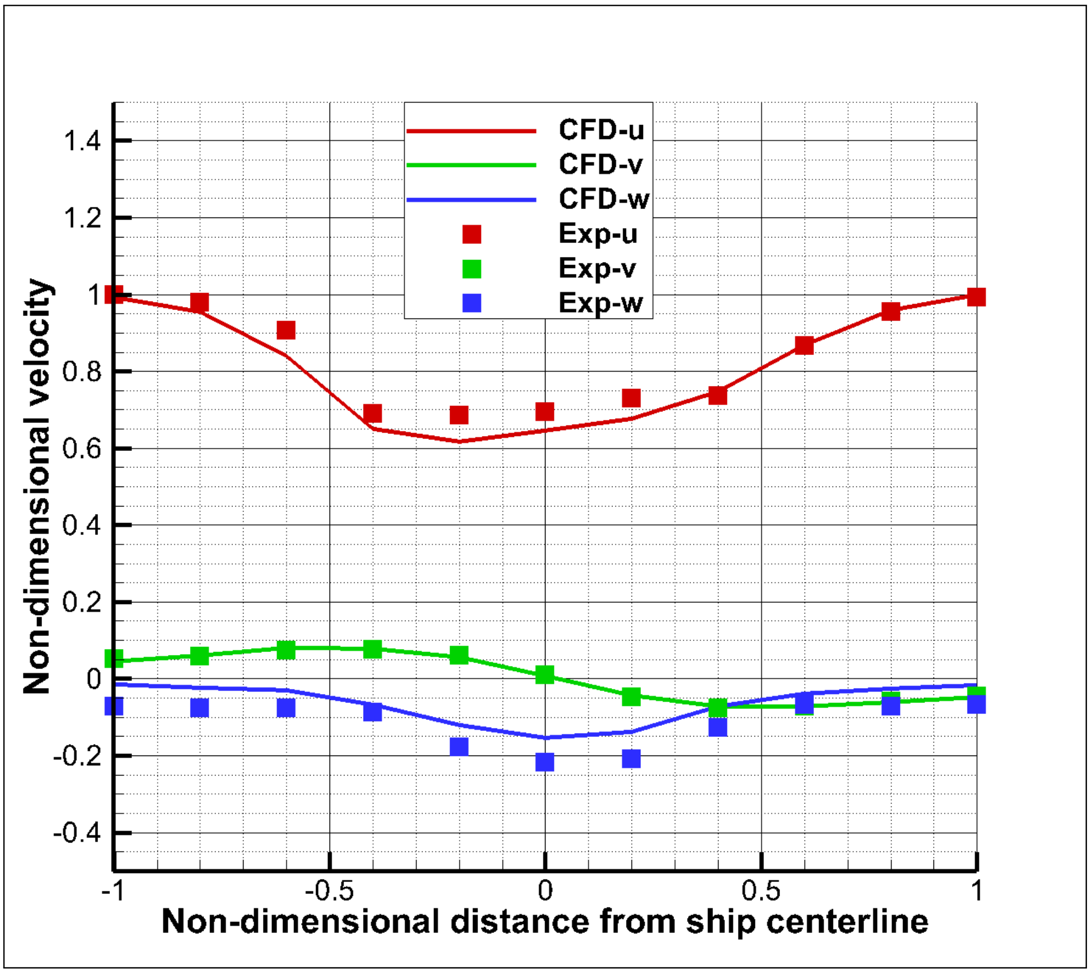

Figure 3.18: Comparison of computational results and experimental data in terms of velocity distribution over flight deck

As it can be seen from comparison between computational and experimental results, unsteady hybrid simulation is satisfactory to obtain real topology of ship airwake.

Euler equations are also solved for this problem. With Runge-Kutta scheme, Euler solutions behave like MILES (Monotone Integrated Large Eddy Simulations) solutions. Slip condition is applied to ship surface for Euler simulations unlike previous RANS and hybrid RANS/LES computations. Like RANS and Hybrid RANS/LES computations, Implicit scheme and Explicit 4th order Runge-Kutta scheme are used for steady-state and unsteady computations respectively. Contour plots of time-averaged unsteady Euler simulations can be found in Appendix A.1. During computations, it is observed that Euler solutions are successful to investigate airwake problem.

In order to demonstrate the unsteady nature of flow, instantaneous plots are presented. From Figure 3.19 to Figure 3.25 instantaneous unsteady RANS/LES simulation results are given for every 5 seconds. Also, the mean velocity distribution over the ship beam at half hangar height and mid-deck are presented with the comparison of instantaneous velocity distribution at t=20 sec in Figure 3.26. As seen from the plot, the velocity fluctuations over the mean values dominate the flow. These fluctuations generate unsteady loading on the rotor blades, which is an unfavorable condition. Moreover, the spanwise velocity distribution over the flight deck indicates the decrease in the freestream velocity. In such an environment, the thrust produced by the helicopter rotor can be insufficient to compensate the necessary thrust for hovering.

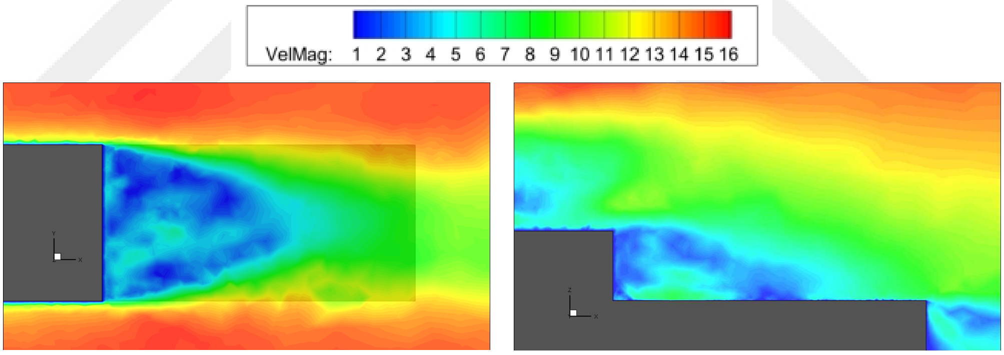

(a) Horizontal slice 11m above sea level (b) Centerline slice

Figure 3.19: Instantaneous contour plots of velocity magnitude, at steady-state (Laminar)

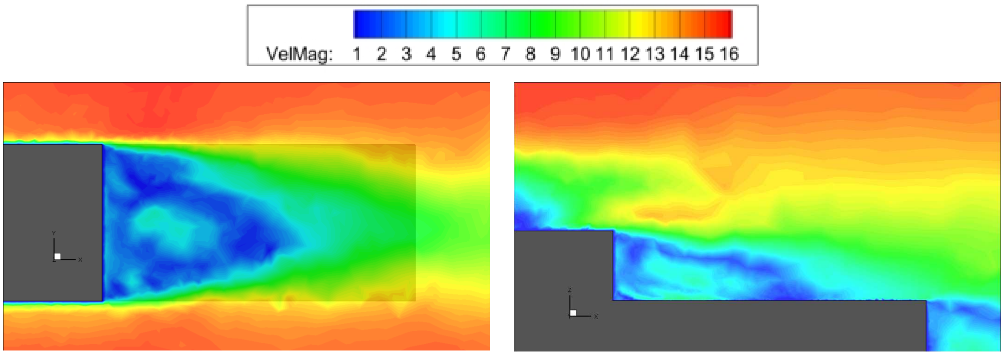

(a) Horizontal slice 11m above sea level (b) Centerline slice

Figure 3.20: Instantaneous contour plots of velocity magnitude, at t=5 sec (LNS)

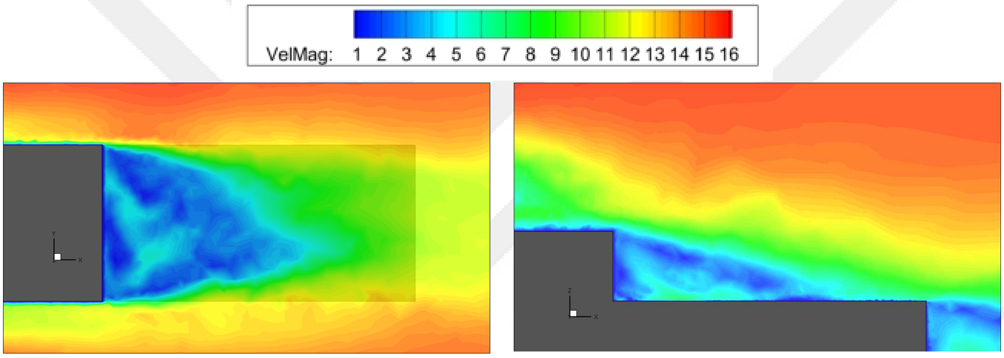

(a) Horizontal slice 11m above sea level (b) Centerline slice

Figure 3.21: Instantaneous contour plots of velocity magnitude, at t=10 sec (LNS)

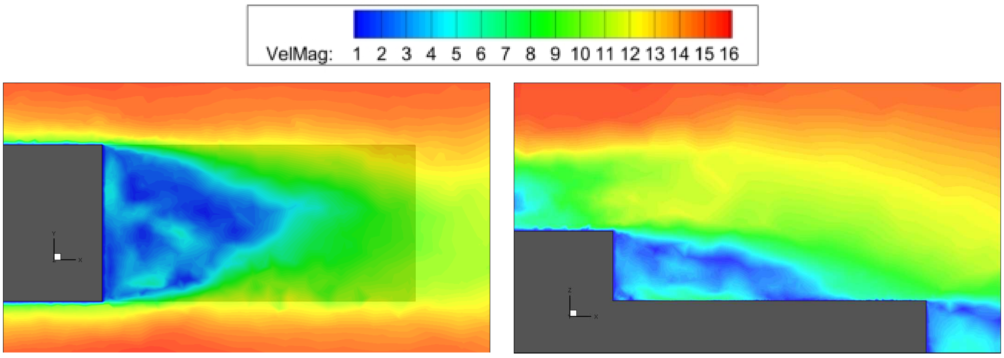

(a) Horizontal slice 11m above sea level (b) Centerline slice

Figure 3.22: Instantaneous contour plots of velocity magnitude, at t=15 sec (LNS)

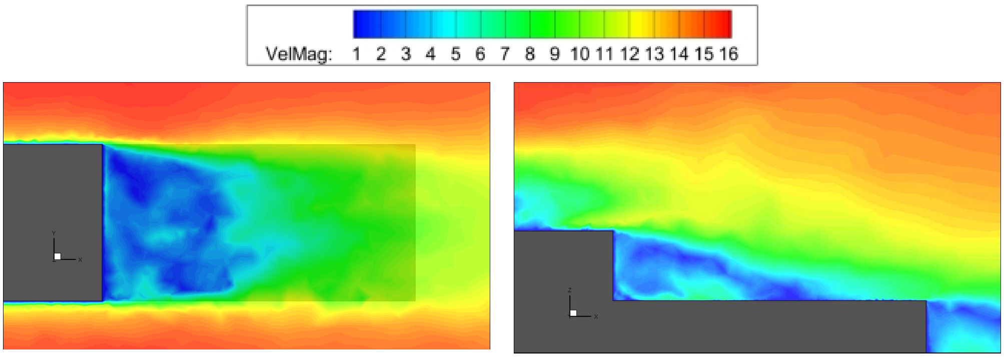

(a) Horizontal slice 11m above sea level (b) Centerline slice

Figure 3.23: Instantaneous contour plots of velocity magnitude, at t=20 sec (LNS)

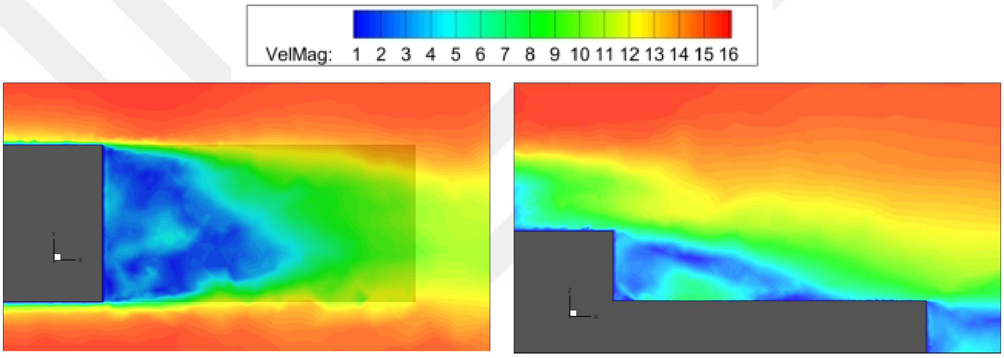

(a) Horizontal slice 11m above sea level (b) Centerline slice

Figure 3.24: Instantaneous contour plots of velocity magnitude, at t=25 sec (LNS)

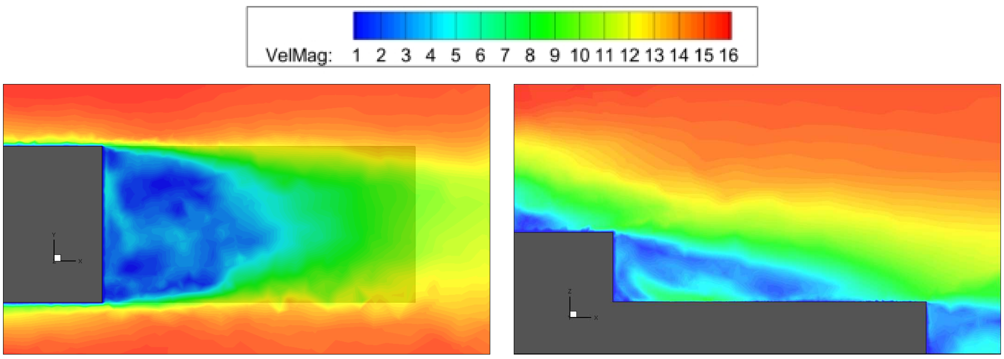

(a) Horizontal slice 11m above sea level (b) Centerline slice

Figure 3.25: Instantaneous contour plots of velocity magnitude, at t=30 sec (LNS)

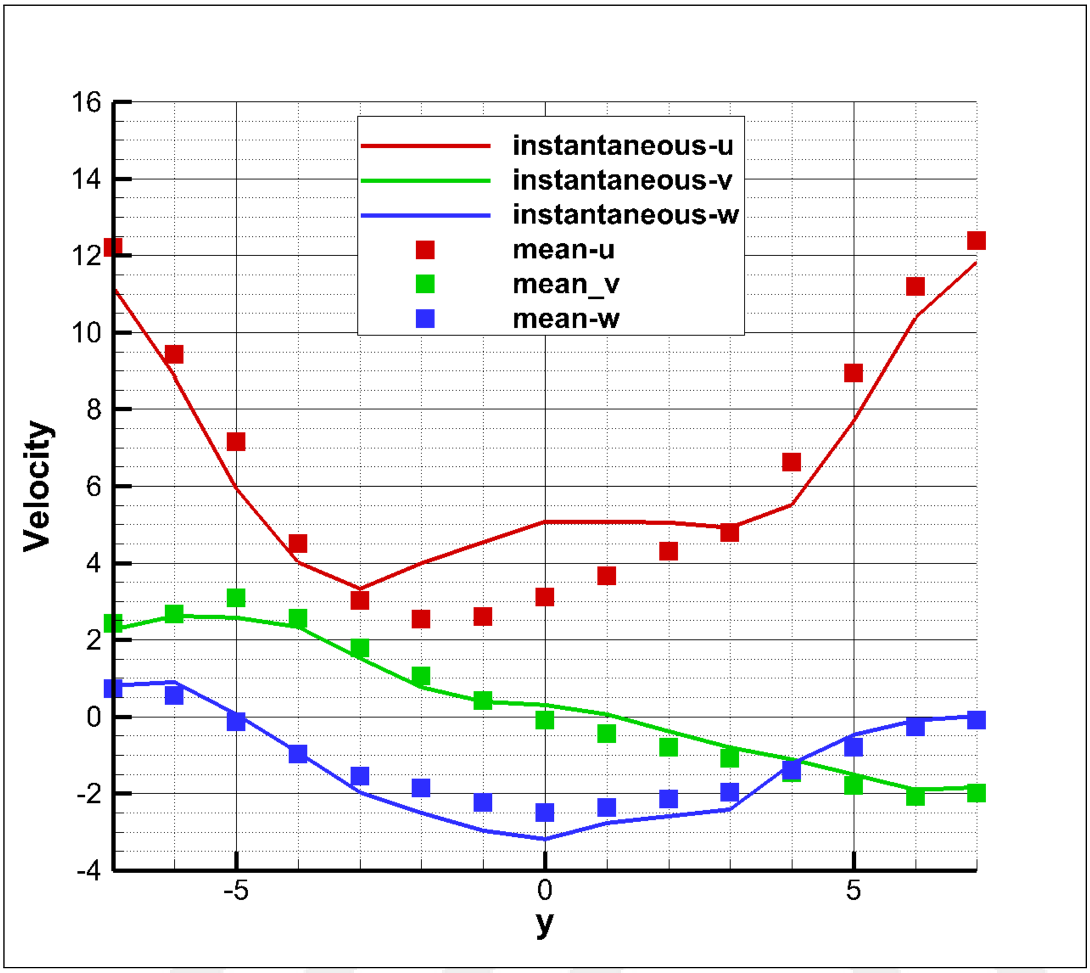

Figure 3.26: Comparison of time averaged and instantaneous velocity magnitude across the fligth deck for horizontal ship

It is important to analyze time history of velocity vector in order to observe and underline the unsteadiness of ship airwake. Therefore, comparison of computational methods mentioned previously are presented in terms of time history data. For this comparison, a point at hangar height and middle of the flight deck is selected. In Figure 3.27, Figure 3.28 and Figure 3.29, time history plots are given for x, y and z components of velocity vector. At the first glance, large fluctuations of velocity can be observed around mean value. These unsteadiness creates unsteady extra loading to helicopter rotor and changes in angle of attack of incoming flow to the rotor blades. In comparison of computational methods, it is seen that velocity vector starts from same value for Realizable $k-\epsilon$ and LNS simulations because both are initialized from the same steady-state. Moreover, LNS performs similar results as Realizable $k-\epsilon$. This situation can be caused by the fact that mesh is coarser for LES. Because of that, the switch from RANS to LES in LNS turbulence model cannot be successed. Also, time history data shows that dissipation rate is larger when Realizable $k - \epsilon$ turbulence model is used and magnitude of fluctuations around mean value is diminishing. For further computations, Realizable $k - \epsilon$ turbulence model can be weak to obtain unsteadiness. On the other hand, LNS turbulence model is more successful to reflect the unsteadiness of flow. In addition, Euler results are more different than LNS. If LES is performed for this computational mesh, Euler solutions can be similar with LES results. From figures, it can be said that more time records is necessary to obtain periodical motions in time history data. This can be helpful to perform more accurate airwake simulations.

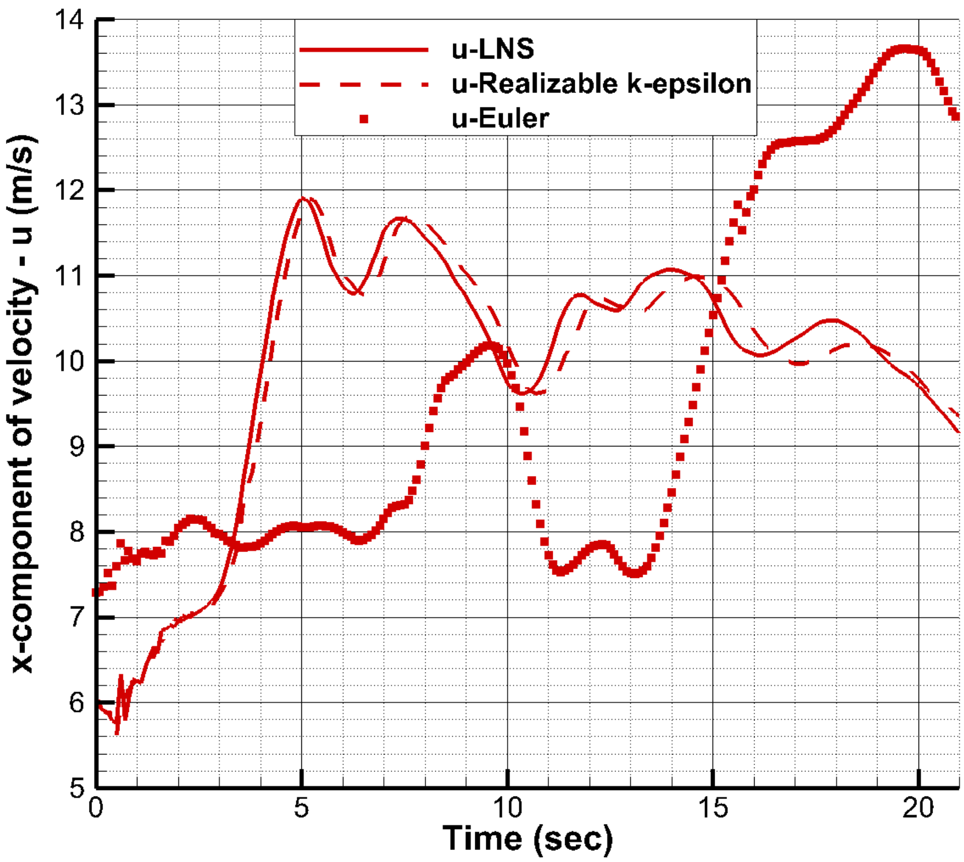

Figure 3.27: Comparison of time history data for x-component of velocity of Realizable $k - \epsilon$, Hybrid Turbulence models and Euler method for location at hangar height and mid-deck

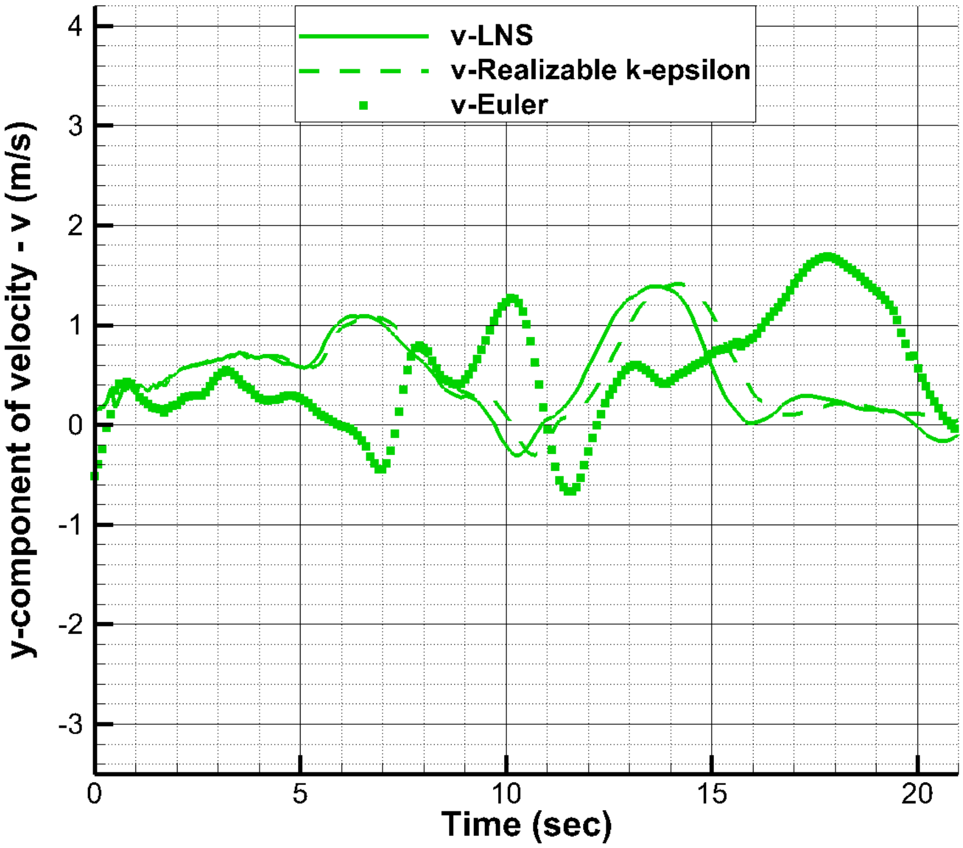

Figure 3.28: Comparison of time history data for y-component of velocity of Realizable $k - \epsilon$, Hybrid Turbulence models and Euler method for location at hangar height and mid-deck

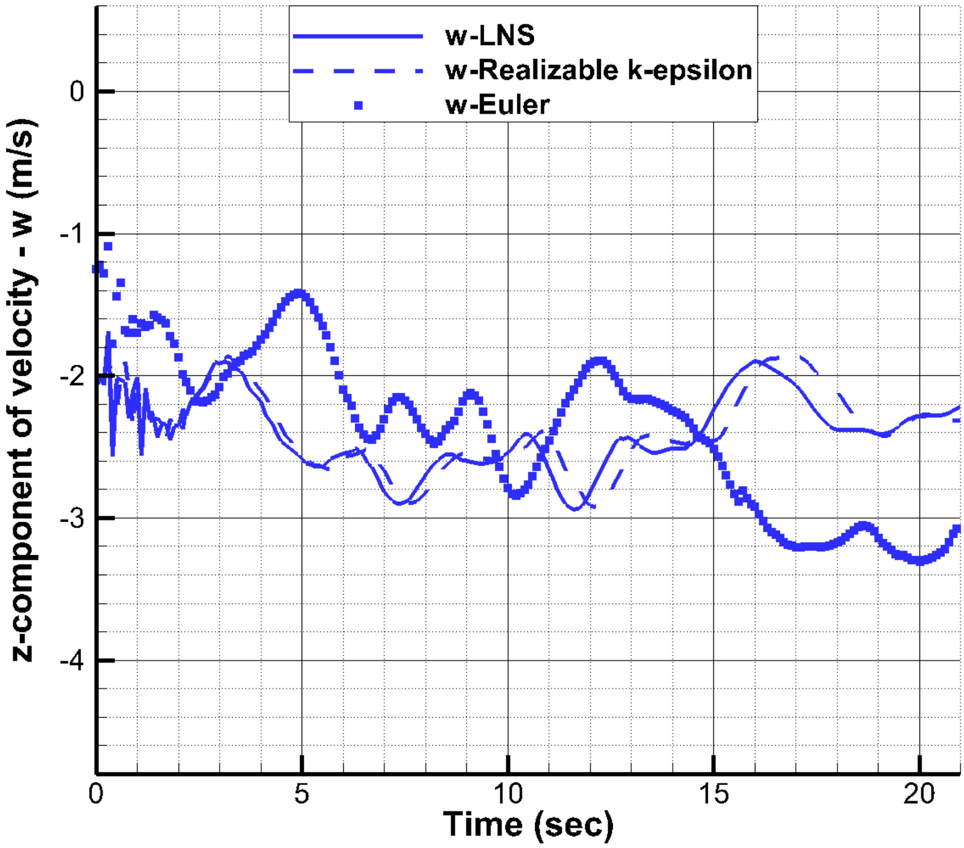

Figure 3.29: Comparison of time history data for z-component of velocity of Realizable $k-\epsilon$, Hybrid Turbulence models and Euler method for location at hangar height and mid-deck

The power spectral analysis is conducted by using time history data of velocity vector. Fast Fourier Transform is applied to time history data for the point (125,0,11). After that, Hamming window filtering is applied. This process is done for longitudinal and vertical component of velocity vector. In Figure 3.30, result for longitudinal component (u) is given. A few peak can be observed around 0.5 Hz. Power is greater at lower frequencies. For simulations with larger time integration, more peaks could occur. In Figure 3.31, PSD analysis of vertical component (w) of velocity vector can be seen. As in previous case, peaks are observed at frequencies lower than 0.5 Hz. Since w velocity directly affects the angle of attack coming to rotor blades, these oscillations in power becomes important.

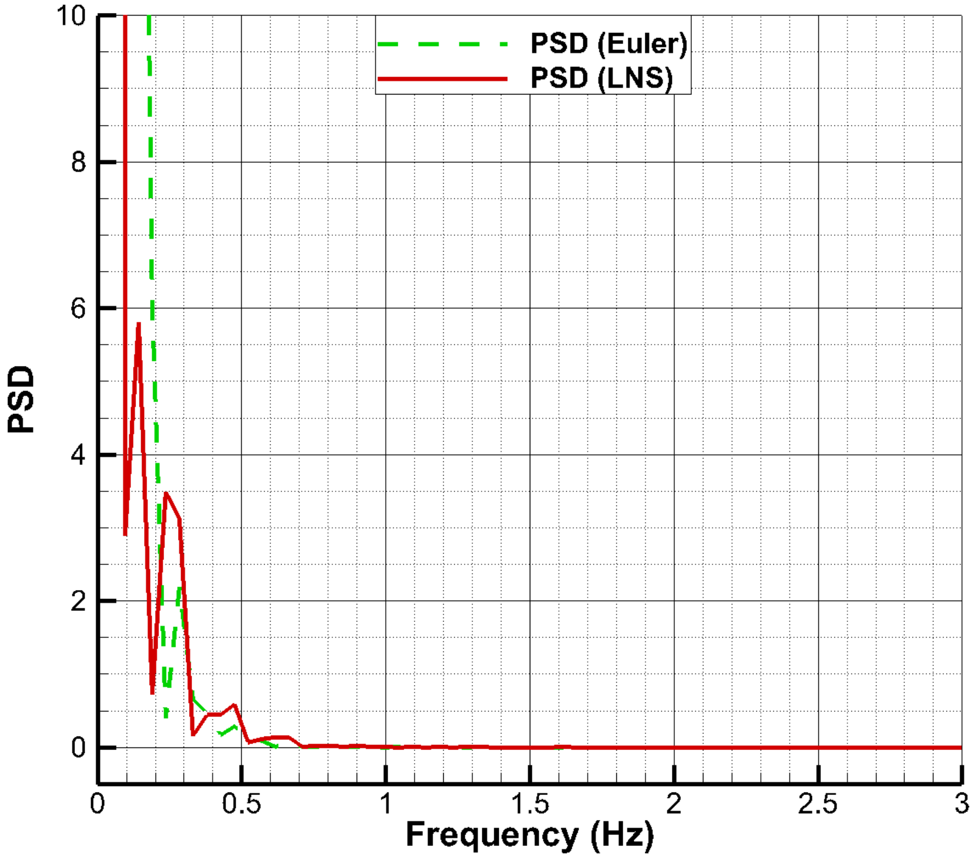

Figure 3.30: PSD analysis of longitudinal component of velocity vector (u) for Euler and LNS turbulence model

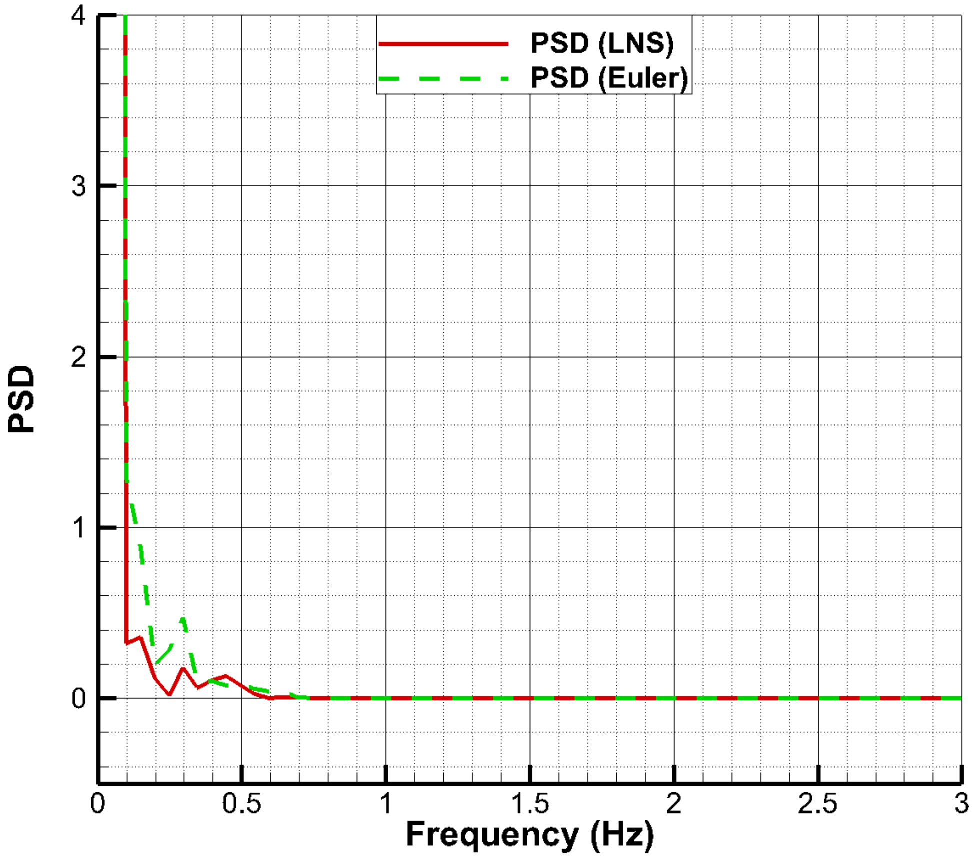

Figure 3.31: PSD analysis of vertical component of velocity vector (w) for Euler and LNS turbulence model

As conclusion, both Realizable $k - \epsilon$ and hybrid RANS/LES turbulence models give promising results when comparing to wind tunnel tests. By comparing contour plots, non-dimensional velocity magnitudes show good agreements. Also, locations of the horseshoe vortex structure are similar, but the comparison between RANS and hybrid RANS/LES method shows that unsteady feature of ship airwake is reflected better with hybrid methods. Therefore, hybrid RANS/LES turbulence model is selected in computations of next cases to be analyzed.

CHAPTER 4

SHIP AIRWAKE SIMULATIONS WITH INCLINED SHIP DECK

4.1 Description of Ship Motion

Ship motion due to sea waves is another important issue for the helicopter shipboard operations. These motions not only affect the landing deck position but also have a great influence on flow over the flight deck. In this chapter, the effect of the ship motion on the airwake is discussed. The ships are under the influence of 6 degree of freedom rigid body motion in various ocean conditions. The ship motion can be classified as translational motions; heave, sway and surge (motions in the x, y and z directions respectively), and rotational motions; pitch, roll and yaw (rotations about the axis x, y and z respectively). Heave, pitch and roll are the unintended periodical motions caused by sea waves. In general, ship motion is approached as an simple harmonic motion. In equation 4.1, the relation of the simple harmonic motion is given. In here, A, ω and ϕ represent wave amplitude, frequency and inital phase respectively. This equation provides enough information about motion due to sea waves for studies not investigating detailed analysis of ship motion over the sea.

$$y = Asin(\omega t + \phi) \tag{4.1}$$

The wave amplitudes and frequency of the waves change with sea states. Sea state parameters are listed in Table 4.1 [27].

Here, the significant sea height is described as the average value of the vertical dis-

Table 4.1: Sea State Parameters

Sea state	World Meteorological Organisation		Design Wave Slope	Design wind Speed (kn)
	Description	Significant Wave Height (m)		
0	Calm (glassy)	0	-	-
1	Calm (ripples)	0-0.1	-	-
2	Smooth (wavelets)	0.1-0.5	-	-
3	Slight	0.5-1.25	1:20	15
4	Moderate	1.25-2.5	1:16	20
5	Rough	2.5-4.0	1:12	25
6	Very Rough	4.0-6.0	1:10	30
7	High	6.0-9.0	-	-
8	Very High	9.0-14.0	-	-
9	Phenomenal	Over 14	-	-

tance between trough and crest, and it is used to define the sea states from calm to rough. For this thesis, the Sea State 6 is chosen. The relative wave amplitude and frequency according to the sea state 6 and 0 degree wave direction are presented in Table 4.2. These data are provided by Khantsis [27] for the Oliver Hazard Perry Class FFG frigate and the ANZAC Class frigate which are in similar size with SFS2. The graphs of heave, roll and pitch motions for SFS2 are given in Figure 4.1, Figure 4.2 and Figure 4.3 respectively. As seen from the graphs, roll motion has a great influence on the ship's flight deck location, therefore roll motion (rotation about x axis) is taken into account for the thesis.

Table 4.2: Wave amplitudes and ship frequencies

	Amplitude [m, deg]	Frequency [Hz]
Heave	2.532	0.076
Roll	26.59	0.114
Pitch	4.791	0.086

In rough sea, SFS2 performs roll motion between 26 degree to -26 degree as seen from Figure 4.2.For this study, the effect of the ship motion is approached as an inclined flight deck problem for a roll motion (rotation about x axis). Therefore, 10 degree inclination is given to ship model. The steady-state and unsteady simulations are performed with the same conditions as previous computational case by using hybrid RANS/LES turbulence model. Grid details are given in Chapter 2.

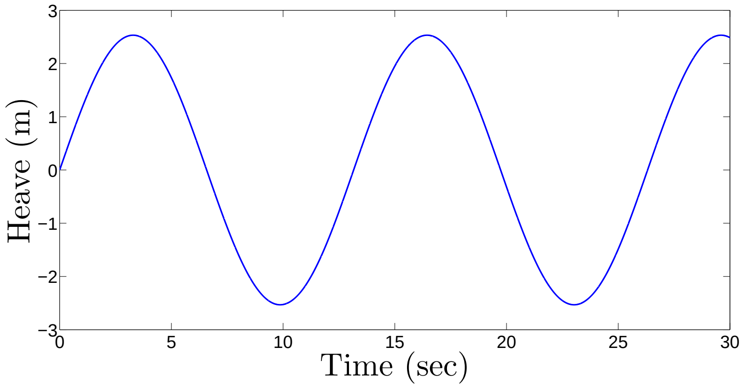

Figure 4.1: Heave motion of SFS2

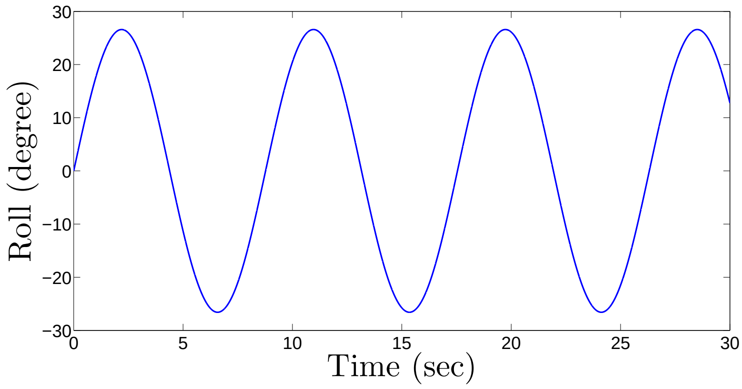

Figure 4.2: Roll motion of SFS2

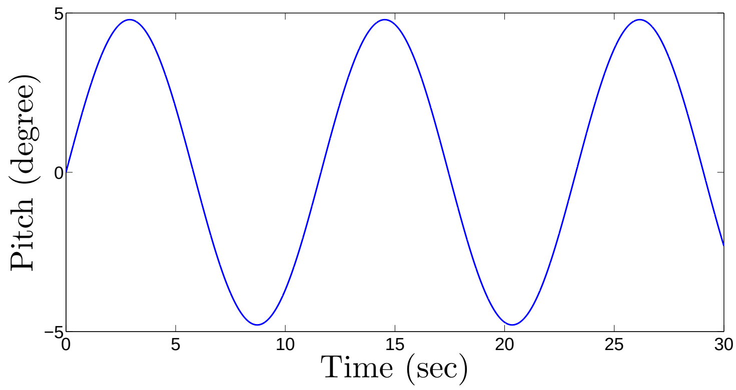

Figure 4.3: Pitch motion of SFS2

4.2 Results for Steady-State Computations and Comparison

In this section, the steady-state simulation results of horizontal and inclined flight deck cases. simulations are performed for 2500 iterations by using hybrid RANS/LES turbulence model. The results are plotted for horizontal slice 7.5 meter above sea level, vertical slice on centerline of the ship and x-axis slice on mid-deck behind the hangar. In Figure 4.4, 4.6 and 4.8 show velocity vectors on z-slice, y-slice and x-slice respectively. Streamtraces on the same locations are presented in Figure 4.5, 4.7 and 4.9.

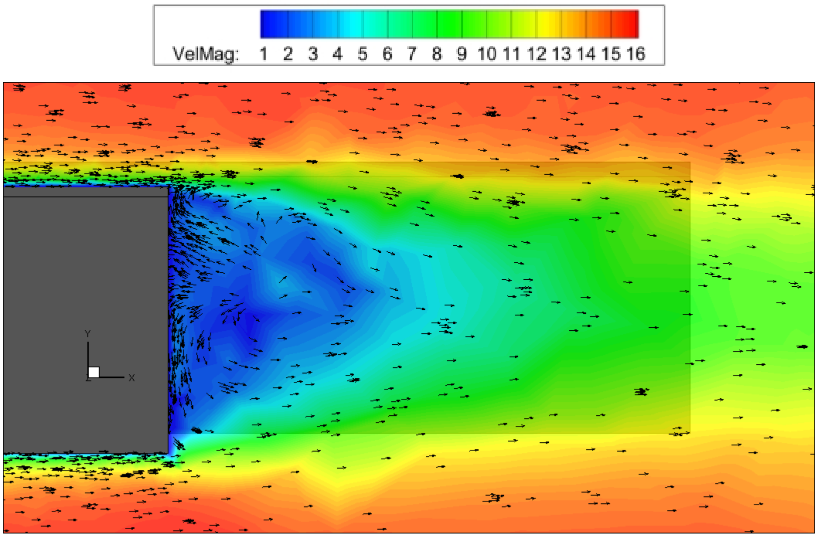

Figure 4.4: Velocity contour and vector plots on the horizontal slice at z=7.5 m above the waterline with steady-state hybrid RANS/LES for inclined ship

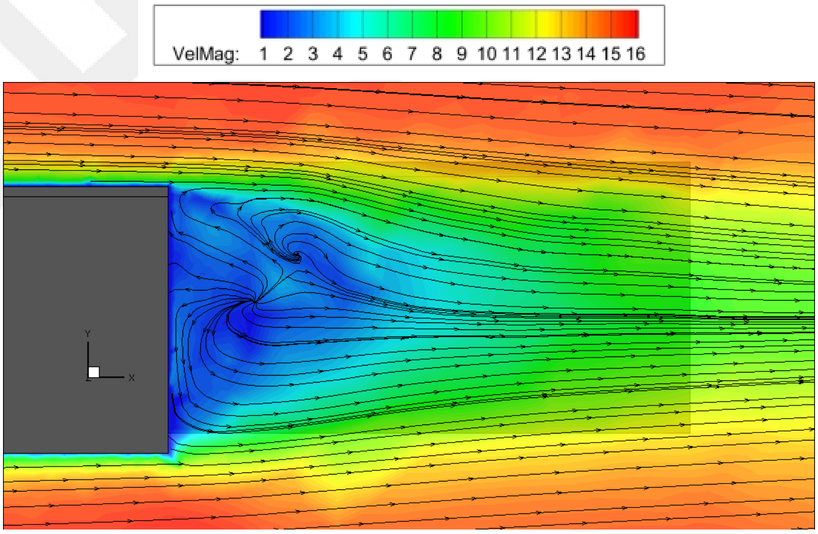

Figure 4.5: Streamlines on the horizontal slice at z=7.5 m above the waterline with steady-state hybrid RANS/LES for inclined ship

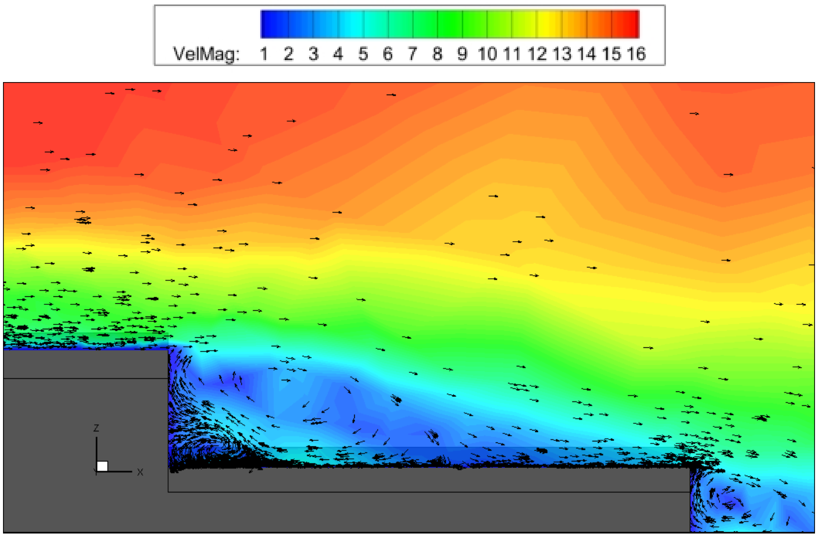

Figure 4.6: Velocity contour and vector plot on vertical slice along centerline with steady-state hybrid RANS/LES for inclined ship

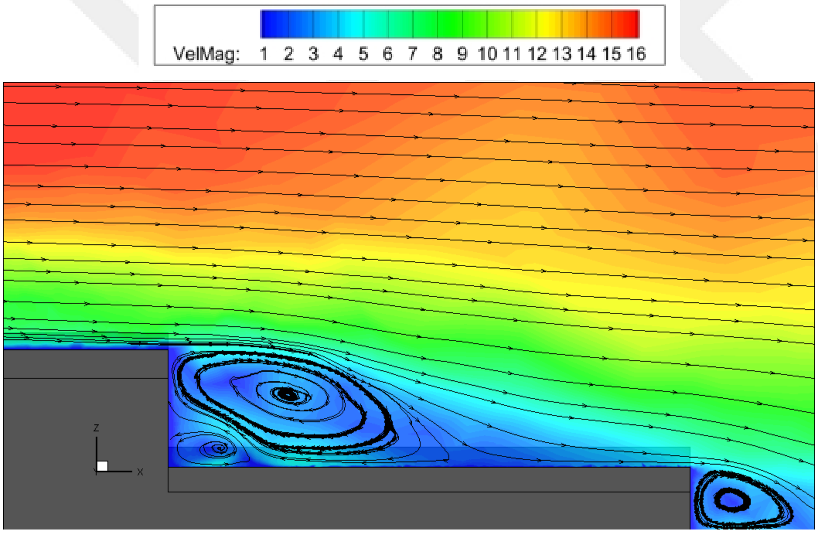

Figure 4.7: Streamlines on vertical slice along centerline with steady-state hybrid RANS/LES for inclined ship

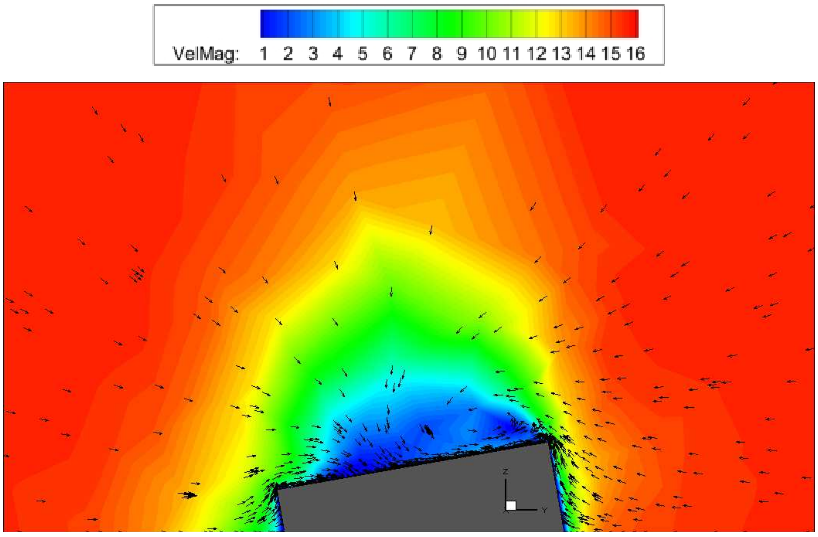

Figure 4.8: Velocity contour and vector plot on x-axis slice at mid-deck with steady-state hybrid RANS/LES for inclined ship

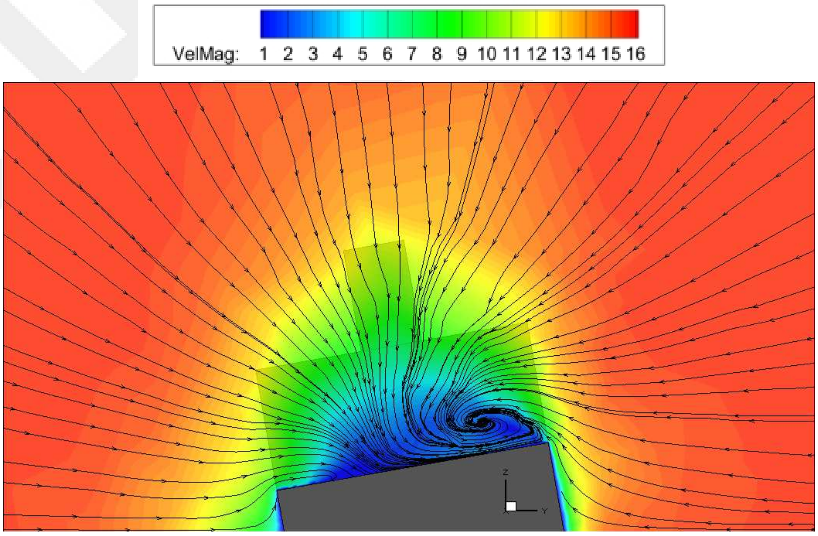

Figure 4.9: Streamlines on x-axis slice at mid-deck with steady-state hybrid RANS/LES for inclined ship

4.3 Results for Unsteady Computations and Comparison

The unsteady computations are conducted for 20 seconds in real time. In Figure 4.10, the mean flow topology over the inclined flight deck at centerline and z=7.5 m above the waterline is given. It can be said that velocity magnitude decreases due to inclination. This causes rotor to produce lower thrust than it needs to hover over the flight deck. Comparison between the horizontal ship case and inclined case shows that the symmetrical feature of the vortical structures disappears. In Figure 4.11, the comparison between the inclined ship and horizontal ship is presented in terms of velocity distribution over the ship beam, at 7.5 meter above the sea surface and at the mid of the flight deck.

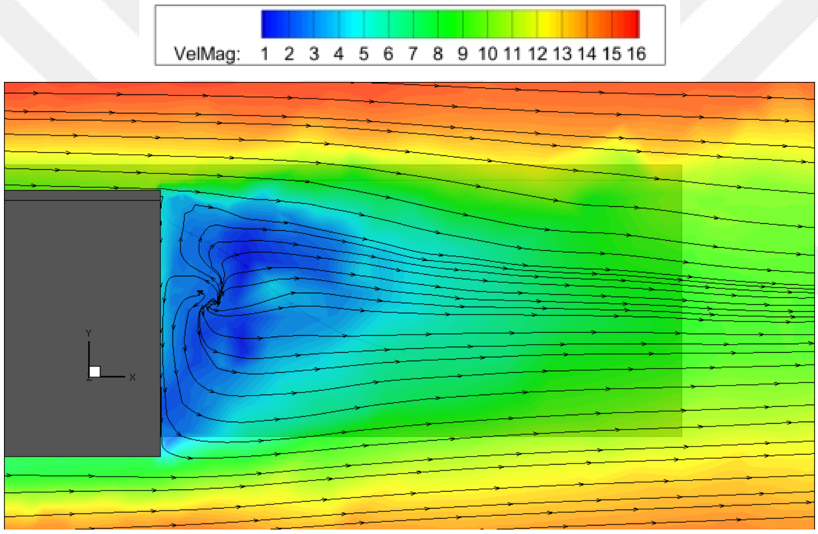

Figure 4.10: Streamlines on the horizontal slice at z=7.5 m above the waterline (top) and at vertical slice along centerline (bottom) with unsteady hybrid RANS/LES for inclined ship

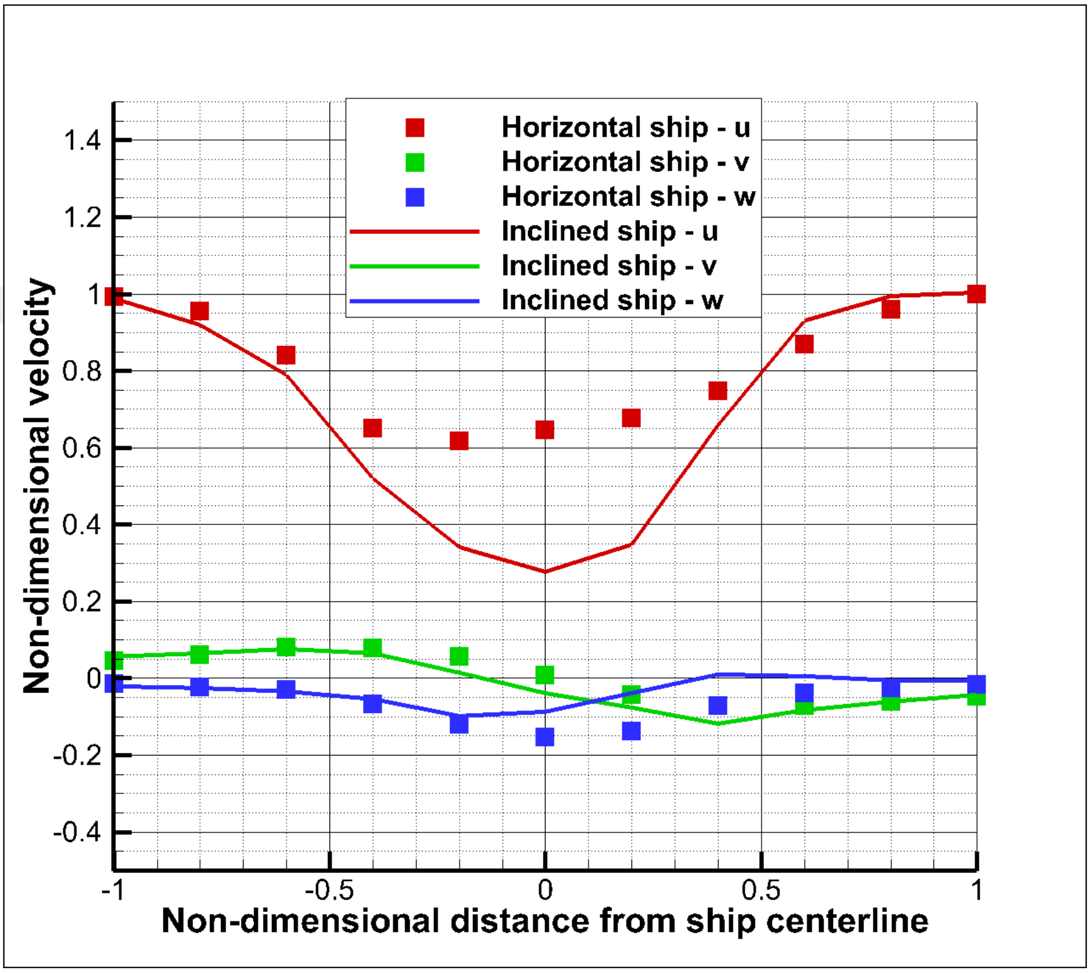

Figure 4.11: Comparison of the time averaged velocity magnitude across the flight deck for horizontal and inclined ship

CHAPTER 5

ROTOR APPLICATION INTO SHIP AIRWAKE SIMULATIONS

5.1 Introduction

In order to see the downwash effect of the helicopter rotor on ship airwake, a rotor disk is added in both previous cases. The rotor of Sikorsky S-76 helicopter is selected since there are many studies investigating hover condition of this rotor in the literature. Main features of S-76 rotor are given in Table 5.1. The blade consists of two different airfoils SC1095 and SC 1095 R8. The twist distribution is illustrated in figure 5.1.

Table 5.1: Characteristics of S-76 main rotor

Radius	6.7056 m
Nominal chord	0.3937 m
Nominal twist	- 10 degree
Blade reference area	10.56029 m^2
Solidity	0.0748
Number of blades	4
Airfoils	SC1095-SC1095R8
Flapping hinge offset	3.7 % radius
Lock number	11.6
100 % RPM	293
100 % Tip Speed	205.74 m/s

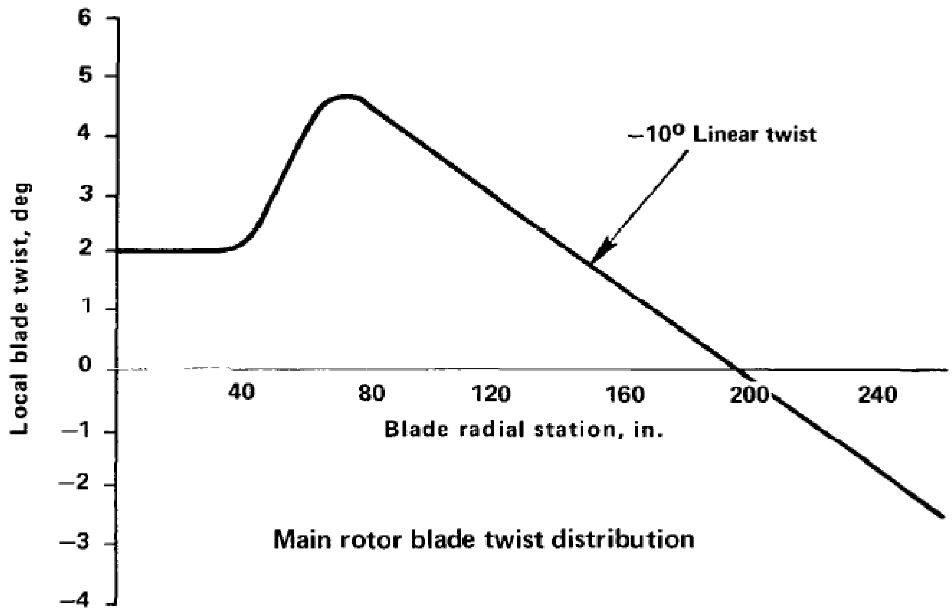

Figure 5.1: Twist distribution of S-76 main rotor blade [22]

5.1.1 Helicopter Rotor Model

Helicopter rotor model in CFD++ can be used for simulations of flows across either helicopter rotors or propellers. Solver modifies pressure and momentums as the flow pass through the rotor disk area. Blade properties and rotor operating conditions are required in order to determine the momentum and pressure changes. This module can be applied as zonal boundary condition or as a source term. This rotor model is based on Blade Element Method. Incremental lift and drag forces calculated by BEM are transformed and integrated over zonal boundary. during computations, mass flux across boundaries which rotor model is applied equals to zero. In order to compute thrust and torque, the momentum fluxes across the given boundaries which is outputted as forces should be calculated. They are computed as given in Equation 5.1. In all flux equations, η_f, $\vec{\vec{\tau}}$ are defined as volume fraction of continuous phase and the viscous stress tensor respectively.

$$MO_{flux} = \{\eta_f(MO_{inv} + MO_{vis}) + MO_{edp}\} \tag{5.1}$$

$$MO_{inv} = (\rho\vec{u})\vec{u}\cdot\hat{n}A + p\hat{n}A \tag{5.2}$$

$$MO_{vis} = \vec{\vec{\tau}}\cdot\hat{n}A \tag{5.3}$$

CFD++ computes forces and moments with respect to local coordinate system. Forces and moments are calculated by using incremental force vectors and position vector according to origin.

$$\vec{F} = \sum\vec{f} \tag{5.4}$$

where

$$\vec{f} = f_x\hat{i} + f_y\hat{j} + f_z\hat{k} \tag{5.5}$$

$$M_0 = \sum r_0 \times \vec{f} \tag{5.6}$$

If moments is desired to be calculated relative to an arbitrary reference point, the following equation can be used.

$$\vec{M} = \sum \vec{r} \times \vec{f} = \sum (\vec{r_0} + (\vec{P_0} - \vec{P})) \times \vec{f} = \vec{M_0} + (\vec{P_0} - \vec{P}) \times \vec{F} \tag{5.7}$$

Non-dimensional forces are calculated by dividing forces by air density, square of freestream velocity and reference area of rotor disk. On the other hand, moment coefficients are found by dividing moments air density, square of freestream velocity, reference area of rotor disk and reference length of moment. Relations are given in Equation 5.8 and 5.9

$$C_{fx_i} = \frac{Force(x_i)}{\rho^{ref}(U^{ref})^2 A_{xi}^{ref}} \tag{5.8}$$

$$C_{Mx_i} = \frac{Moment(x_i)}{\rho^{ref}(U^{ref})^2 A_{xi}^{ref} L_{xi}^{ref}} \tag{5.9}$$

x,y,z components of force and moment will give drag, lift and yaw according to flow direction and angle of attack. To illustrate, lift coeficient for two dimensional frame in xy plane is calculated as folllows:

$$C_L = C_{f_y} \cos\alpha - C_{f_x} \sin\alpha \tag{5.10}$$

5.1.2 Validation in Hover Condition

Firstly, a validation process is performed before implementing the rotor model in ship cases. For this reason, a new computational domain containing 2400 K grid cells is generated. In Figure 5.2 and Figure 5.3, the domain can be seen. The outer domain is 3R away from the center of rotor disk, where R is the radius of rotor. The upper face is 5R above the disk, while the lower face is 3R below it.

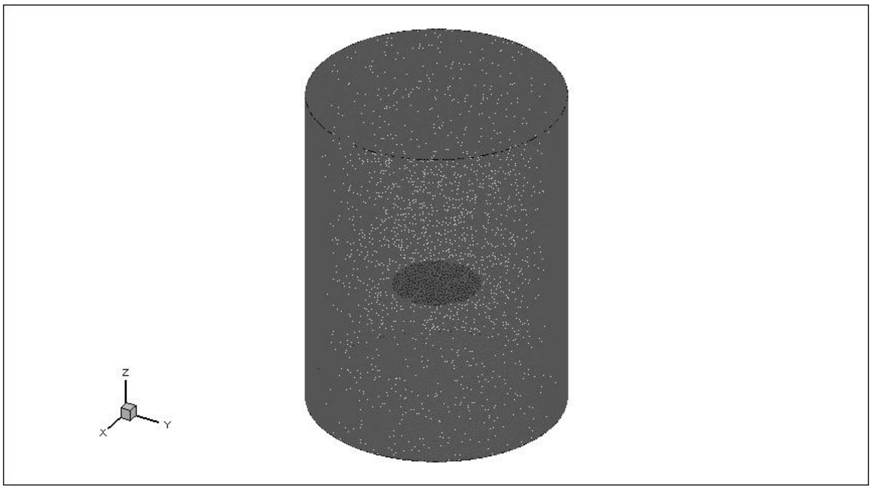

Figure 5.2: Cylindrical computational domain

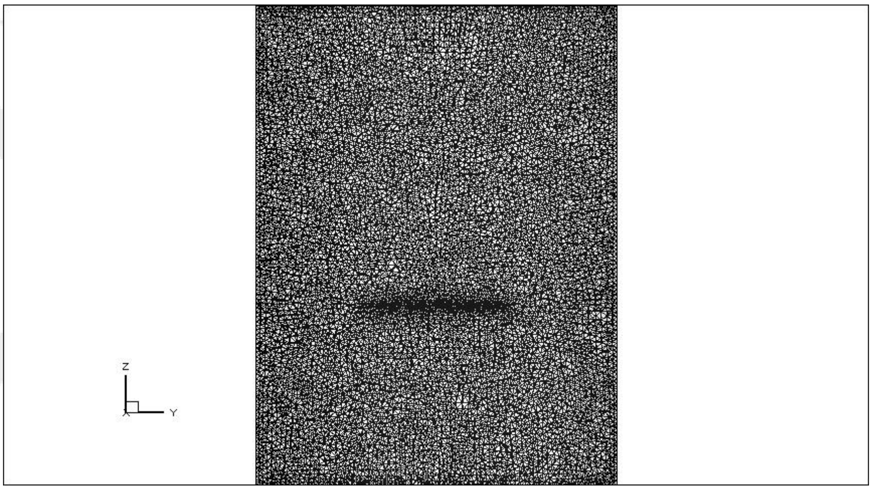

Figure 5.3: Computaional mesh around the rotor disk on centerline

Computations are performed in steady-state for 2000 iterations. Airfoil data is obtained by Qblade software which is based on poteantial flow theory and they are given in Appendix A.2. They are also validated with experimental data by Flemming [10]. In validation case, 3 different collective pitch angle are taken into account; 4.2, 6.7 and 8.1 degrees. CFD computations are performed in steady-state with a freestream velocity 1.0 m/s. In CFD++, such a small freestream velocity, computations approaches to hover conditions. The results are compared in terms of rotor thrust coefficient and rotor torque coefficient. In Figure 5.4, results of computations are presented with the experimental data. Experimental data is taken from study of Shinoda [57]. As it can be seen from the figure, good agreement with is obtained by computations. In Figure 5.5, the downwash effect of the rotor is demonstrated for hover flight with 4.2 collective pitch angle. The streamlines are plotted over a horizontal slice passing through the center of the rotor disk. Zoomed view is given in Figure 5.6. The velocity magnitude distribution over top disk is illustrated in figure 5.7, and velocity vector representing the flow velocity on the top disk of rotor is given in Figure 5.8

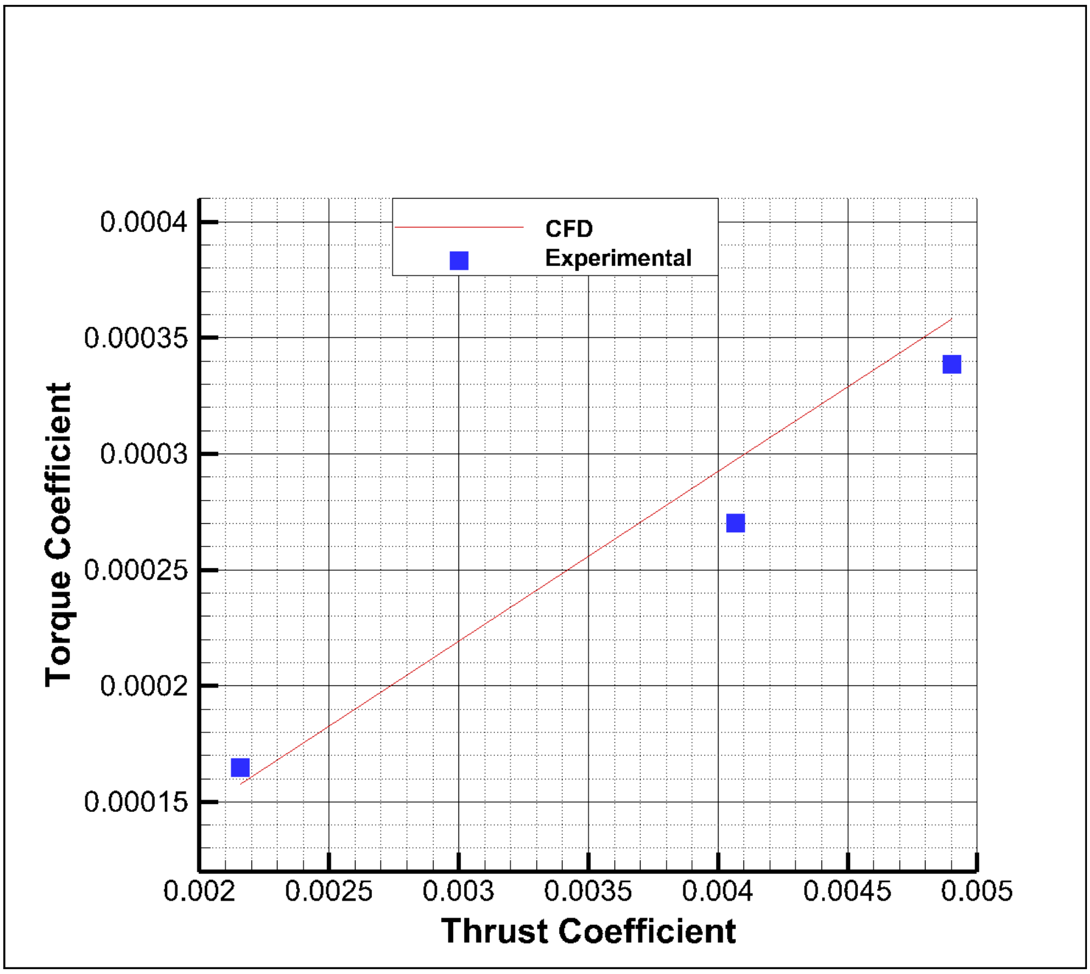

Figure 5.4: Results of CFD analysis in compared to experimental data [57] in terms of thrust coefficient vs torque coefficient

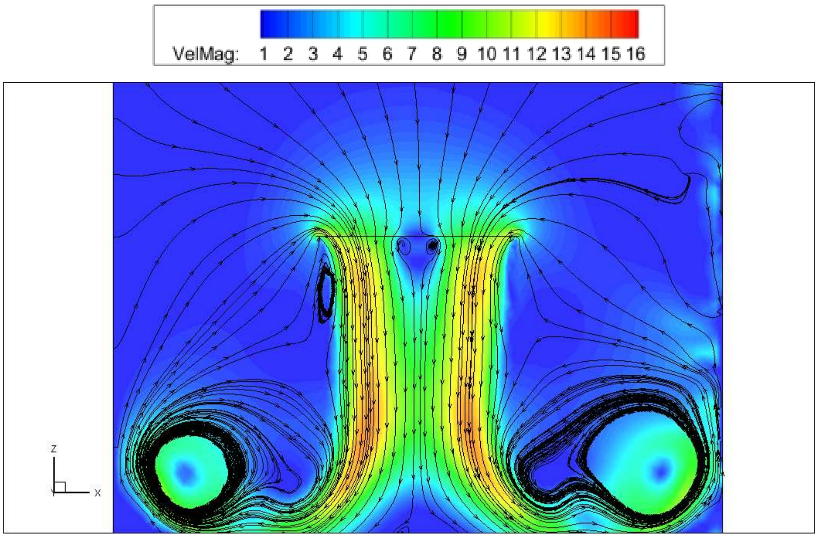

Figure 5.5: Downwash effect of helicopter rotor with 4.2 collective pitch angle

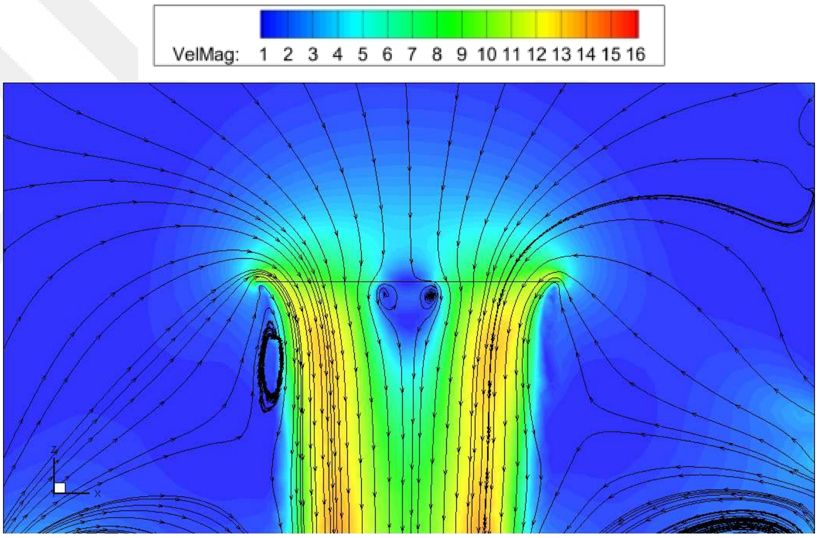

Figure 5.6: Zoomed view of downwash effect of helicopter rotor with 4.2 collective pitch angle

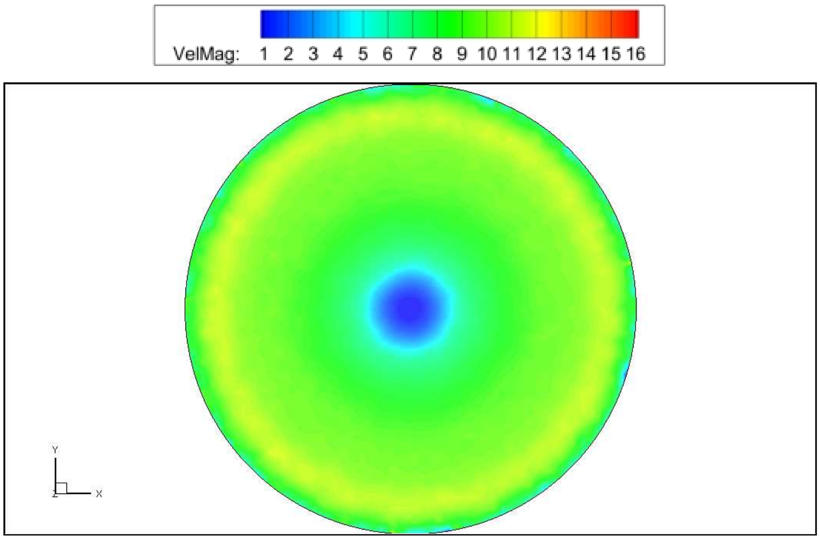

Figure 5.7: Velocity distribution over rotor top disk

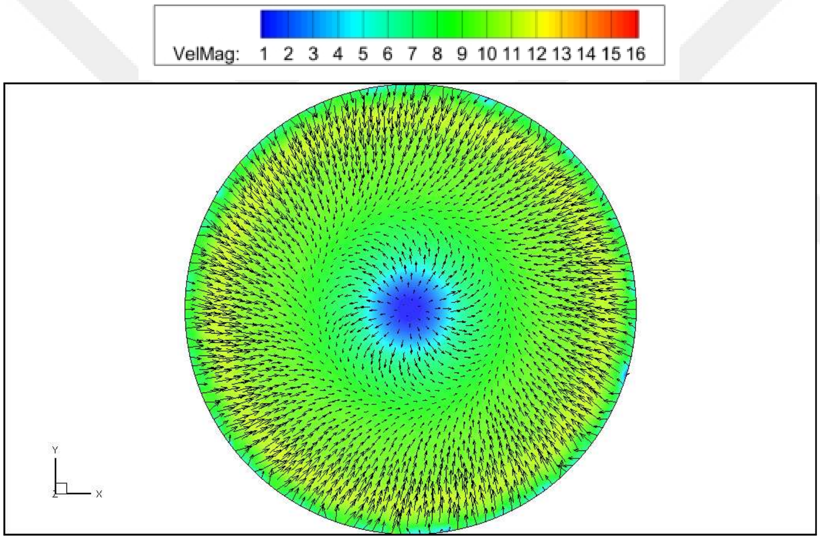

Figure 5.8: Velocity vectors on rotor top disk

5.2 Ship Airwake Studies for Horizontal Flight Deck with Rotor Disk

The ship airwake computations with a rotor disk model are computed as steady-state at first. In order to obtain a general idea of downwash effect of downwash effect of rotor on airwake, steady-state simulations are sufficient. For this case, 8.1 degree collective pitch is selected which provides necessary thrust to maintain in hover position. Simulations are performed 2500 iterations with hybrid RANS/LES turbulence model as in previous cases. As mentioned Section 5.1.1, 2500 iterations are enough for rotor model to converge. Grid details and other computational details are stated in Chapter 2. The results are presented in terms of velocity magnitude contour plots and streamlines of the flow. In Figure 5.9, Figure 5.10 and Figure 5.11 the plots are given for horizontal slice at half hangar height, vertical slice across the centerline of ship and vertical slice behind hangar at mid-deck respectively. It can be seen from figures, new small vortical structures are observed, while the magnitude of vortex cores in original case decreases.

In Figure 5.12, the z-component of velocity vector is presented for SFS2 without rotor (a) and SFS2 with rotor (b). In comparison with horizontal ship case without rotor disk and with rotor disk case, it can be seen that magnitude of vertical component of velocity increases with an actuator disk at the hangar height. Downwash effect of rotor makes the magnitude of w in the negative direction greater.

Helicopter rotor model in CFD++ creates steady-state flow to rotor disk. However, ship airwake problem is unsteady in nature. Therefore, unsteady two-way coupled simulations are necessary in order to obtain more accurate analysis.

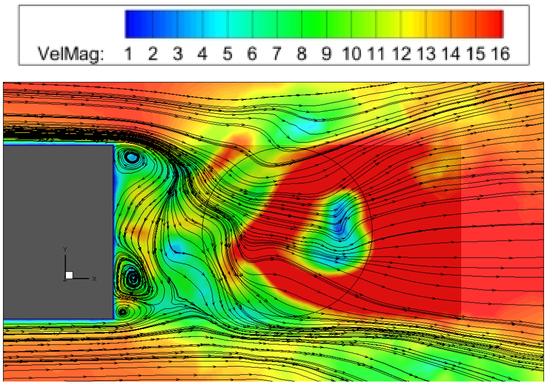

Figure 5.9: Contour plots of velocity magnitude and streamlines over flight deck at horizontal slice at mid-deck (z=7.5m) (Steady-state)

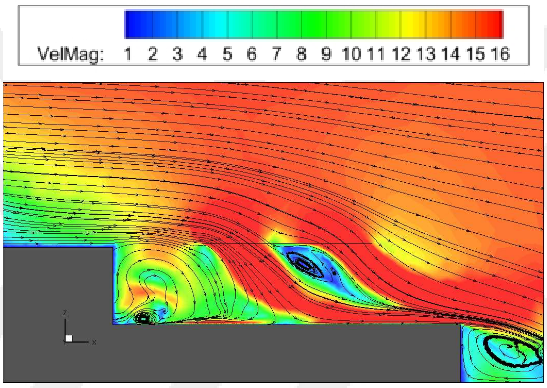

Figure 5.10: Contour plots of velocity magnitude and streamlines over flight deck at vertical slice at centerline (y=0m) (Steady-state)

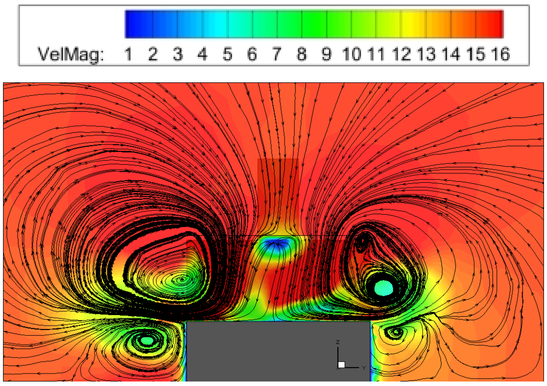

Figure 5.11: Contour plots of velocity magnitude and streamlines over flight deck at vertical slice at mid-deck (x=125m) (Steady-state

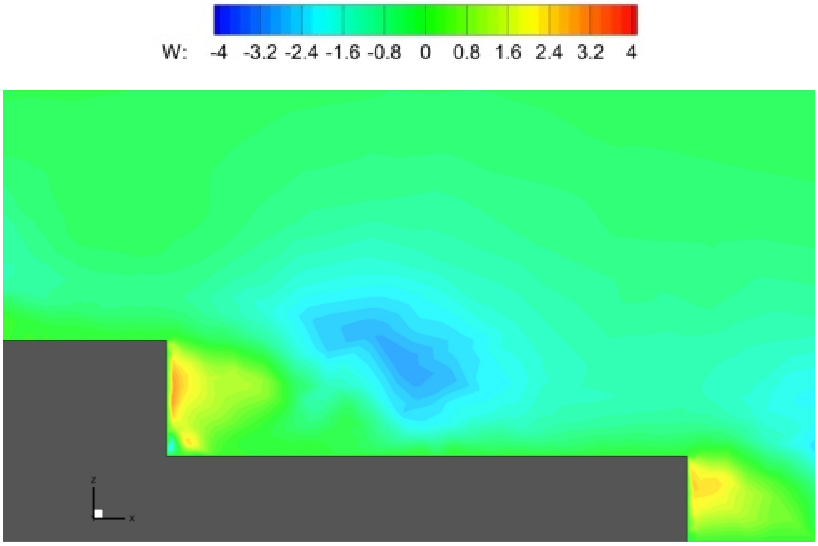

(a) Contour plots of vertical component of velocity vector of SFS2 without rotor (Steady-state)

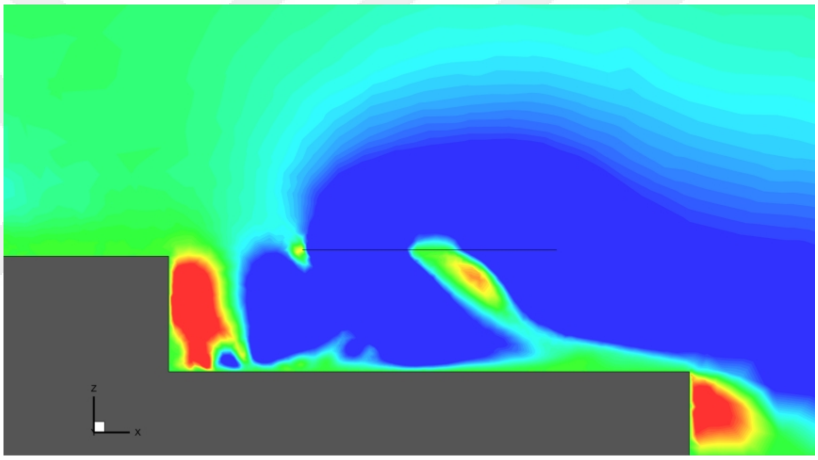

(b) Contour plots of vertical component of velocity vector of SFS2 with rotor (Steady-state)

Figure 5.12: Comparison of SFS2 with and without rotor disk cases

5.3 Ship Airwake Studies for Inclined Flight Deck with Rotor

The inclined ship is also modeled with a rotor disk in order to investigate the roll motion of the flight deck with the helicopter rotor. Again, the computational details are the same as horizontal ship with rotor case. The results are presented in terms of velocity magnitude contour plots and streamlines of the flow. In Figure 5.13, Figure 5.14 and Figure 5.15, the plots are given for horizontal slice over the flight deck at 7.5 m above sea level, vertical slice across the centerline of ship and vertical slice behind hangar at mid-deck respectively. If the case of horizontal ship and rotor combination are compared with this case, the inclined flight deck creates more asymmetric flow. As a result, unsteady nature of ship airwake increases.

The comparison of magnitudes of vertical component of velocity vector for inclined SFS2 case is given in Figure 5.16. The results for horizontal ship model case are valid for this case too. For inclined ship with rotor case, it can be seen that larger positive vertical velocity exists in hub region of rotor and front of the disk.

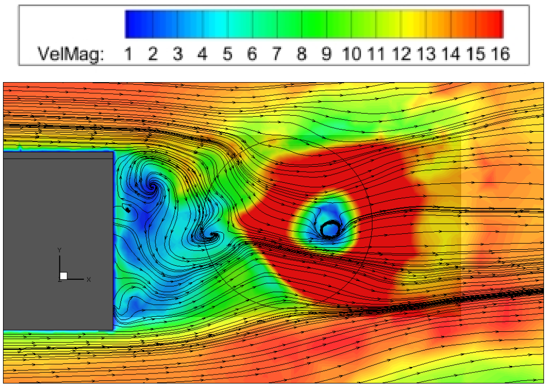

Figure 5.13: Contour plots of velocity magnitude and streamlines over inclined flight deck at horizontal slice at mid-deck (z=7.5m) (Steady-state)

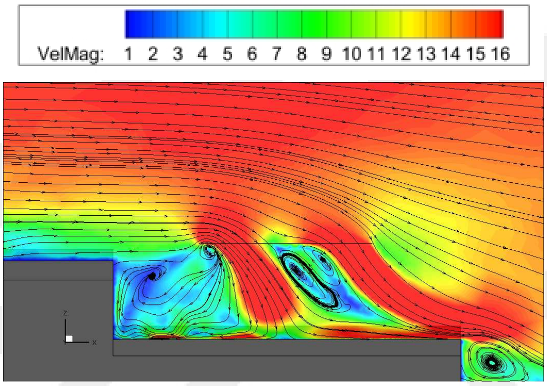

Figure 5.14: Contour plots of velocity magnitude and streamlines over inclined flight deck at vertical slice at centerline (y=0m) (Steady-state)

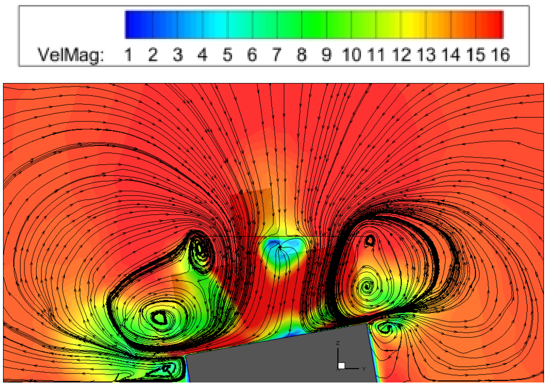

Figure 5.15: Contour plots of velocity magnitude and streamlines over inclined flight deck at vertical slice at mid-deck (x=125m) (Steady-state)

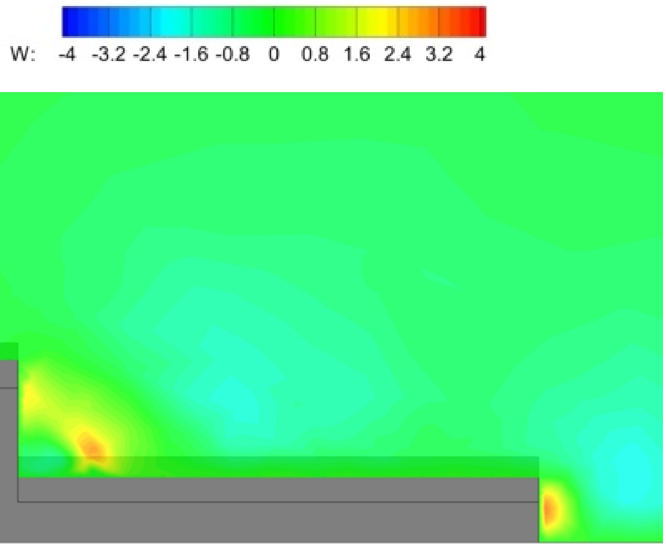

(a) Contour plots of vertical component of velocity vector of inclined SFS2 without rotor (Steady-state)

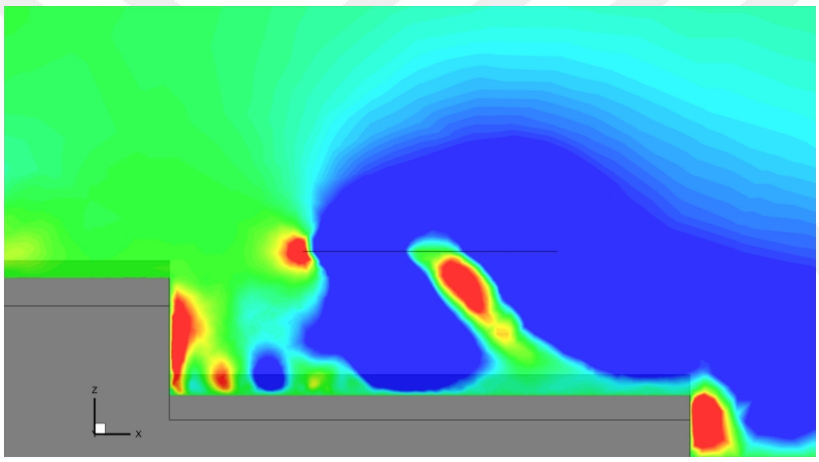

(b) Contour plots of vertical component of velocity vector of inclined SFS2 with rotor (Steady-state)

Figure 5.16: Comparison of inclined SFS2 with and without rotor disk cases

CHAPTER 6

CONCLUSIONS AND RECOMMENDATIONS

6.1 Concluding Remarks

The ship airwake is an important issue for pilots during helicopter shipboard operations. The flow around the superstructure of ship is unsteady, separated, vortical and turbulent. Due to ship airwake over the flight deck, it is hard to operate shipbased helicopters. Therefore, it is important to perform good analysis in order to obtain safe helicopter operating limits.

In this study, the ship airwake is investigated with several different turbulence models for steady-state and unsteady simulations. The results are compared with the experimental data obtained from previous ship airwake studies in the literature. The CFD simulations are performed for two cases: with a horizontal ship and an inclined ship with 10 degree rolled-up position (representing the ship motion due to sea waves) In horizontal ship case, unsteady Realizable $k-\epsilon$ simulations are performed for 24 seconds, while 30-second in real-time simulations are performed with LNS turbulence model. Unsteady hybrid RANS/LES simulations give reasonable results in terms of main flow features, velocity distribution over the flight deck and peak frequencies. Additionally, Euler equations are solved to compute ship airwake. It is stated that Euler is also successful for this problem. Time history data of velocity vector obtained by different computational methods is compared. It is observed that while Euler results are different from LNS, Realizable $k-\epsilon$ simulation results follow in wake of LNS results. Transition from steady-state to unsteady is longer in Euler than LNS and Realizable $k-\epsilon$. The unsteady feature of the ship airwake can also be seen from the plots comparing the mean and instantaneous spanwise velocity distributions over the flight deck.

In addition, ship airwake is affected by ship motion due to the sea waves. Therefore, the simulations including an inclined flight deck illustrating the roll motion of the ship due to sea waves are performed by using hybrid RANS/LES turbulence model for 20 seconds in real time. Ship motions are discussed and definitions of motions and sea states are explained. Steady-state simulation results are sufficient to compare horizontal and inclined flight decks. It is seen that one of two vortex cores disappears and it is stated that this causes to asymmetric loading to helicopter rotor.

Moreover, downwash effect of helicopter rotor is another important issue in ship airwake problems. Therefore, S-76 rotor operating over the flight deck for these two cases are considered to investigate the ship airwake affected by helicopter rotor downwash. Steady-state simulations are sufficient to understand a general opinion about one-way interaction between rotor and airwake. As a result of ship with actuator disk simulations, numbers of small vortical structures are generated and structure of ship airwake flow gets more complicated. However, airwake problem is unsteady in nature, therefore unsteady two-way coupled simulations are necessary to be performed.

In summary, the following conclusions can be made:

- The flowfield is unsteady for both horizontal and inclined ship decks.
- The flowfield features and the vortical structures are different for these two cases.
- Rotor is also changing the flow features completely.
- Rotor is actually not hovering but should trimmed in forward flight under the given wind and airwake conditions.
- Unsteady hybrid RANS/LES simulations are promising for this problem.
- Unsteady nature of the flowfield and complex interactions still make the simulation of this ship/rotor problem challenging.

6.2 Future Works

In the light of this thesis, some further studies listed below can be performed.

- First of all, longer time records can be obtained in order to use in flight simulator which are necessary for pilot's training.
- Moreover, in the light of this thesis, the CFD simulations can be conducted in two-way coupled for ship airwake/helicopter interactions by inputting the induced velocities due to ship airwake into the rotor model. Coupled simulations are needed for more accurate modeling of the problem. This can be done by including ship airwake velocities as an inflow in the BEM code for the rotor and allowing for the trim of the rotor time-dependently.
- Dynamic Interface simulations can also be performed as a future work of this thesis. DI simulations are important for developing more accurate simulators for pilot training.
- In addition, the periodic motions can be applied to the ship model to simulate the realistic unsteady ship motion by using overset grid.
- Instead of the rotor disk model, the real rotor blades can be used with overset grids for the ship airwake/rotor interaction simulation.
- Also, Atmospheric Turbulence and Atmospheric Boundary Layer can be included into computations, because they are exist in nature and influence the flow characteristics.

REFERENCES

[1] ABRAS, J., AND HARIHARAN, N. S. Comparison of cfd hover predictions on the s-76 rotor.

[2] ALPMAN, E., LONG, L. N., BRIDGES, D. O., AND HORN, J. F. Fully-coupled simulations of the rotorcraft/ship dynamic interface. vol. 63, American Helicopter Society, Inc, p. 1367.

[3] BOUSMAN, W. G. Aerodynamic characteristics of sc1095 and sc1094 r8 airfoils.

[4] BRIGGS, M. J., DEMIRBILEK, Z., AND LIN, L. Vertical ship motion study for ambrose entrance channel, new york. Tech. rep., DTIC Document, 2014.

[5] CARRICA, P. M., SADAT-HOSSEINI, H., AND STERN, F. Cfd analysis of broaching for a model surface combatant with explicit simulation of moving rudders and rotating propellers. *Computers & Fluids 53* (2012), 117–132.

[6] CARRICA, P. M., WILSON, R. V., NOACK, R. W., AND STERN, F. Ship motions using single-phase level set with dynamic overset grids. *Computers & fluids 36*, 9 (2007), 1415–1433.

[7] CROZON, C., STEIJL, R., AND BARAKOS, G. N. Numerical study of helicopter rotors in a ship airwake. *Journal of Aircraft 51*, 6 (2014), 1813–1832.

[8] EVERITT, L. http://www.public.navy.mil.

[9] FERRIER, B., AND CARICO, D. Testing and evaluation of landing aids to improve helicopter/ship operational limits. vol. 63, American Helicopter Society, Inc, p. 1589.

[10] FLEMMING, R. J. An experimental evaluation of advanced rotorcraft airfoils in the nasa ames eleven-foot transonic wind tunnel.

[11] FORREST, J., OWEN, I., PADFIELD, G., AND HODGE, S. Towards fully simulated ship-helicopter operating limits: the importance of ship airwake fidelity. vol. 64, American Helicopter Society, Inc, p. 339.

[12] FORREST, J. S., KÄÄRIÄ, C. H., AND OWEN, I. Determining the impact of hangar-edge modifications on ship–helicopter operations using offline and piloted helicopter flight simulation. vol. 3, pp. 11–13.

[13] FORREST, J. S., AND OWEN, I. An investigation of ship airwakes using detached-eddy simulation. 656–673.

[14] FORREST, J. S., OWEN, I., PADFIELD, G. D., AND HODGE, S. J. Ship-helicopter operating limits prediction using piloted flight simulation and time-accurate airwakes. *Journal of Aircraft 49*, 4 (2012), 1020–1031.

[15] GAONKAR, G. H. Toward a complete stochastic model of airwake turbulence for helicopter shipboard operation. vol. 63, American Helicopter Society, Inc, p. 1355.

[16] GEIGER, D., SAHASRABUDHE, V., HORN, J., BRIDGES, D., AND POLSKY, S. Advanced modeling and flight control design for gust alleviation on ship-based helicopters. vol. 64, American Helicopter Society, Inc, p. 1963.

[17] HE, C., LEE, D., ZHAO, J., AND WARE, C. A unified control and simulation tool in support of rotorcraft/ship dynamic interface. vol. 67, American Helicopter Society, Inc.

[18] HE, S. H., LIU, D. Y., AND TAN, D. Comparison of various spatial discretizaion schemes in numerical simulation for ship airwakes. 63–68.

[19] HODGE, S. J., ZAN, S. J., ROPER, D. M., PADFIELD, G. D., AND OWEN, I. Time-accurate ship airwake and unsteady aerodynamic loads modeling for maritime helicopter simulation. *Journal of the American helicopter society 54*, 2 (2009), 22005–22005.

[20] HORN, J. F., SPARBANIE, S. M., COOPER, J., AND SCHIERMAN, J. On-line identification of ship airwake disturbances on rotorcraft.

[21] HWANG, J. Y., AND KWON, O. J. Assessment of tip shape effect on rotor aerodynamic performance in hover. *International Journal of Aeronautical and Space Sciences 16*, 2 (2015), 295–310.

[22] JEPSON, D., MOFFITT, R., HILZINGER, K., AND BISSELL, J. Analysis and correlation of test data from an advanced technology rotor system.

[23] JOHNSON, W. Performance and loads data from a wind tunnel test of a full-scale rotor with four blade tip planforms. Tech. rep., DTIC Document, 1980.

[24] JOURNÉE, J. M. J., AND PINKSTER, J. *Introduction in Ship Hydromechanics*. Delft University of Technology.

[25] KÄÄRIÄ, C. H., FORREST, J. S., OWEN, I., AND PADFIELD, G. D. Simulated aerodynamic loading of an sh-60b helicopter in a ship's airwake.

[26] KÄÄRIÄ, C. H., WANG, Y., PADFIELD, G. D., FORREST, J. S., AND OWEN, I. Aerodynamic loading characteristics of a model-scale helicopter in a ship's airwake. *Journal of Aircraft 49*, 5 (2012), 1271–1278.

[27] KHANTSIS, S. *Control system design using evolutionary algorithms for autonomous shipboard recovery of unmanned aerial vehicles*. PhD thesis, Royal Melbourne Institute of Technology, 2006.

[28] KIM, J. W., MARPU, R., SANKAR, L. N., EGOLF, T. A., AND HARIHARAN, N. A parametric study of planform effects on rotor hover performance using a hybrid navier stokes–free wake methodology.

[29] KIM, S., LEE, H. H., ET AL. Fully nonlinear seakeeping analysis based on cfd simulations. International Society of Offshore and Polar Engineers.

[30] KIM, Y., KIM, K. H., KIM, J. H., KIM, T., SEO, M. G., AND KIM, Y. Time-domain analysis of nonlinear motion responses and structural loads on ships and offshore structures: development of wish programs. *International Journal of Naval Architecture and Ocean Engineering 3*, 1 (2011), 37–52.

[31] KOTTAPALLI, S., AND LEYLAND, J. Analysis of open loop higher harmonic control at high airspeeds on a modern four-bladed articulated rotor.

[32] KÄÄRIÄ, C. H., WANG, Y., PADFIELD, G. D., FORREST, J. S., AND OWEN, I. Aerodynamic loading characteristics of a model-scale helicopter in a ship's airwake. 1271–1278.

[33] LEE, D., HORN, J. F., SEZER-UZOL, N., AND LONG, L. N. Simulation of pilot control activity during helicopter shipboard operations.

[34] LEE, D., SEZER-UZOL, N., HORN, J., AND LONG, L. N. Simulation of helicopter shipboard launch and recovery with time-accurate airwakes. *Journal of Aircraft 42*, 2 (2005), 448–461.

[35] LEE, D., SEZER-UZOL, N., HORN, J. F., AND LONG, L. N. Simulation of helicopter shipboard launch and recovery with time-accurate airwakes.

[36] LI, X., ZHANG, T., ZHANG, Y. O., AND WANG, Y. X. Numerical analysis of ship motion coupled with tank sloshing. IEEE, pp. 1–10.

[37] LIN, R. Q., AND KUANG, W. A fully nonlinear, dynamically consistent numerical model for solid-body ship motion. i. ship motion with fixed heading. The Royal Society, p. rspa20100310.

[38] LIU, C. M., AND GAO, Y. Grid generation and airwake simulation on ship. vol. 246, Trans Tech Publ, pp. 336–340.

[39] METACOMP. http://www.metacomptech.com/index.php/products/cfd.

[40] MONTANYE, P. L., SMITH, E. C., RAHN, C. D., AND CONLON, S. C. Shipboard helicopter gust response alleviation using active trailing edge flaps. vol. 65, American Helicopter Society, Inc.

[41] MORA, R. B. Experimental investigation of the flow on a simple frigate shape (sfs).

[42] MOUSAVIRAAD, S. M. Cfd prediction of ship response to extreme winds and/or waves.

[43] MUIJDEN, J. V., BOELENS, O., DER VORST, J. V., AND GOODEN, J. Computational ship airwake determination to support helicopter-ship dynamic interface assessment. p. 3078.

[44] NACAKLI, Y., AND LANDMAN, D. *Helicopter Downwash Frigate airwake Interaction Flowfield PIV Surveys in a Low Speed Wind Tunnel*. the AHS International 67th Annual Forum and Technology Display, 2013.

[45] NAVARRETE, J. *Construction of airfoil performance tables by the fusion of experimental and numerical data*. PhD thesis, Rice University, 2004.

[46] OWEN, H., HOUZEAUX, G., SAMANIEGO, C., LESAGE, A. C., AND VÁZQUEZ, M. Recent ship hydrodynamics developments in the parallel two-fluid flow solver alya. *Computers & Fluids 80* (2013), 168–177.

[47] POINTWISE. http://www.pointwise.com/.

[48] QUON, E., SMITH, M. J., ROSENFIELD, N., AND WHITEHOUSE, G. Investigation of ship airwakes using a hybrid computational methodology.

[49] QUON, E. W., CROSS, P. A., SMITH, M. J., ROSENFELD, N. C., AND WHITEHOUSE, G. R. Investigation of ship airwakes using a hybrid computational methodology.

[50] RAJAGOPALAN, G., NIAZI, S., WADCOCK, A. J., YAMAUCHI, G. K., AND SILVA, M. J. Experimental and computational study of the interaction between a tandem-rotor helicopter and a ship.

[51] RAJMOHAN, N., ZHAO, J. G., HE, C. G., KIM, J., SANKAR, L. N., AND PRASAD, J. V. R. An efficient pod based technique to model rotor/ship airwake interaction. No. 1.

[52] RIGSBY, J., GEIGER, D., AND XIN, H. *Ship Airwake Turbulence Nodeling Using Moving Stochastic Spectral Filters*. The 67th American Helicopter Society International Annual Forum, Virginia Beach, VA.

[53] SCHAFER, S. A. *Flight Test Measurement of Ship Airwake Disturbances Using Small-scale Rotorcraft*. PhD thesis, The Pennsylvania State University, 2015.

[54] SCHAU, K. A., GAONKAR, G. H., AND POLSKY, S. Helicopter downwash effects on ship airwakes: Predictions, modeling from a database, and simulation. American Helicopter Society, Inc.

[55] SCOTT, P., OWEN, I., WHITE, M., ET AL. The effect of ship size on the flying qualities of maritime helicopters.

[56] SEZER-UZOL, N., SHARMA, A., AND LONG, L. N. Computational fluid dynamics simulations of ship airwake. 369–392.

[57] SHINODA, P. M., AND JOHNSON, W. Performance results from a test of an s-76 rotor in the nasa ames 80-by 120-foot wind tunnel. *AIAA Paper 93* (1993), 3414.

[58] SIMONSEN, C. D., OTZEN, J. F., JONCQUEZ, S., AND STERN, F. Efd and cfd for kcs heaving and pitching in regular head waves. *Journal of Marine Science and Technology 18*, 4 (2013), 435–459.

[59] SMITH, M. J., POTSDAM, M., WONG, T., BAEDER, J. D., AND PHANSE, S. Evaluation of computational fluid dynamics to determine two-dimensional airfoil characteristics for rotorcraft applications. *Journal of the American Helicopter Society 51*, 1 (2006), 70–79.

[60] SNYDER, M. R., KANG, H. S., BROWNELL, C. J., AND BURKS, J. S. Validation of ship air wake simulations and investigation of ship air wake impact on rotary wing aircraft.

[61] SONESON, G. L., AND HORN, J. F. Simulation testing of advanced response types for ship-based rotorcraft.

[62] SPARBANIE, S. M., HORN, J. F., GEIGER, D. H., AND SAHASRABUDHE, V. A stochastic model of unsteady ship airwake disturbances on rotorcraft. vol. 65, American Helicopter Society, Inc.

[63] SYMS, G. F. Simulation of simplified frigate airwakes using a lattice boltzman method. 1197–1206.

[64] TEZDOGAN, T., DEMIREL, Y. K., KELLETT, P., KHORASANCHI, M., INCECIK, A., AND TURAN, O. Full-scale unsteady rans cfd simulations of ship behaviour and performance in head seas due to slow steaming. *Ocean Engineering 97* (2015), 186–206.

[65] THORNBER, B., STARR, M., AND DRIKAKIS, D. Implicit large eddy simulation of ship airwakes. 715–736.

[66] TURNER, G., CLARK, W., COX, I., FINLAY, B., AND DUNCAN, J. Project saif-assessment of ship helicopter operating limits using the merlin helicopter simulator. vol. 62, American Helicopter Society, Inc, p. 226.

[67] UENG, S. K., LIN, D., AND LIU, C. H. A ship motion simulation system. *Virtual reality 12*, 1 (2008), 65–76.

[68] Weymouth, G. D., Wilson, R. V., and Stern, F. Rans computational fluid dynamics predictions of pitch and heave ship motions in head seas. *Journal of Ship Research 49*, 2 (2005), 80–97.

[69] Zhang, F., Xu, H., and Ball, N. G. *Numerical Simulation of Unsteady Flow over SFS 2 Ship Model.* No. 81. 47th AIAA Aerospace Sciences Meeting Including The New Horizons Forum and Aerospace Exposition, 5 - 8 January 2009, Orlando, Florida.

APPENDIX A

APPENDIX NAME

A.1 Euler Simulation Results

Unsteady Euler simulation results which are mentioned in Chapter 3 are presented in Figure A.1 and Figure A.2. In the first figure, velocity contour plots are given for a vertical slice along ship centerline. Flow topology for a horizontal slice at half hangar height can be observed in the second figure. Unsteady computations were time-averaged over 20-second time recording.

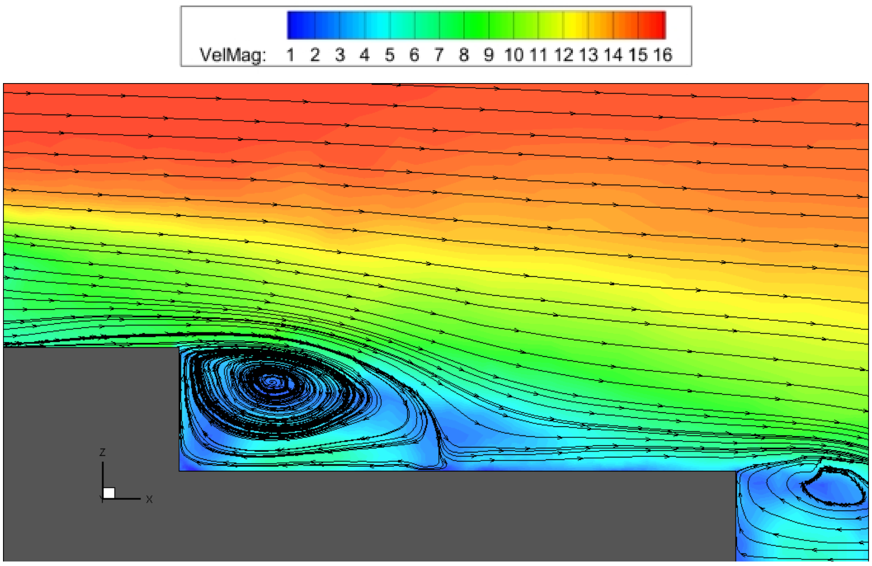

Figure A.1: Velocity contour and velocity vector plots of unsteady Euler simulations on vertical slice along ship centerline

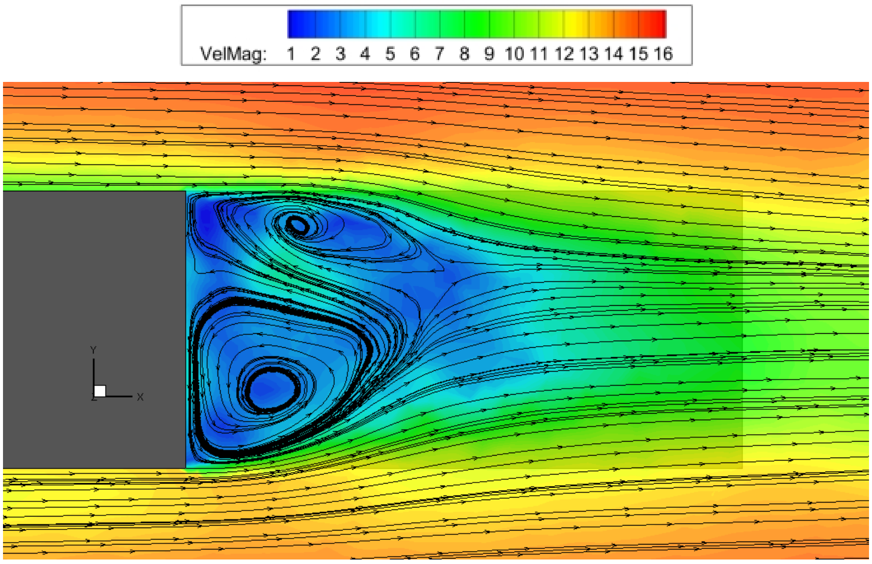

Figure A.2: Velocity contour and velocity vector plots of unsteady Euler simulations on horizontal slice at half hangar height

The separations behind superstructure of ship and recirculation zone can be observed from these figure. As in experiments, there exist two vortex cores behind hangar. Also, location of the recirculation zone and reattachment of the separated flow to surface of the flight deck are similar with experimental data.

A.2 Airfoil Characteristics of SC1095 and SC1095R8

In this section, aerodynamic characterics of airfoils used in S-76 rotor blades are explained. Blade planform is given in Figure A.3 [22]. Two different airfoils are generally used in S-76 rotor, SC1095 and SC1095R8. SC1095R8 is a modified version of SC1095. In Table A.1 and Table A.2, airfoil coordinates are given for SC1095 and SC1095R8 respectively.

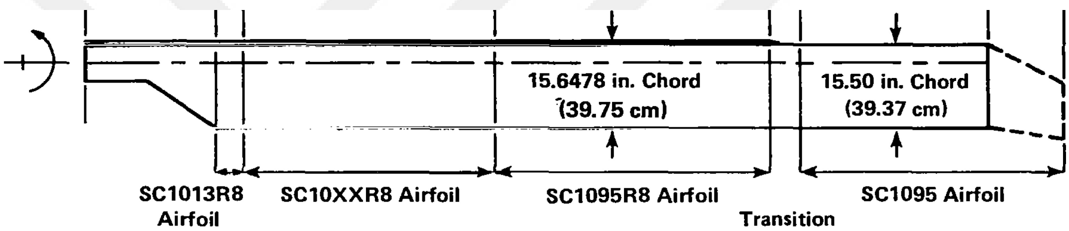

Figure A.3: Planform of the main rotor blade of S-76

In order to perform sectional control, rotor blade is divided into 8 sections; the first 6 sections were calculated according to SC1095R8 airfoil and the last 2 sections were calculated according to SC1095 airfoil. Pitch angle is calculated according to twist distribution given in Figure 5.1 in Chapter 5 and collective pitch at hover condition. In all computation in Chapter 5, tip Mach number is selected as 0.60, and therefore, sectional speed is calculated by using given tip Mach number and distance of section from rotor hub center. Non-dimensional lift and drag forces were calculated by using Qblade software. In Figure A.4 ,Figure A.5, Figure A.6, Figure A.7, Figure A.8, Figure A.9, Figure A.10 and Figure A.11, plot of lift and drag coefficients are presented for airfoils corresponding the given sections.

Upper Surface		Lower Surface	
x/c	y/c	x/c	y/c
0.00	0.00	0.00	0.00
0.0008200	0.0039660	0.0015000	-0.0045890
0.0039700	0.0091750	0.0052400	-0.0090190
0.0096600	0.0152640	0.0111900	-0.0136550
0.0183300	0.0219940	0.0194300	-0.0183320
0.0299900	0.0287360	0.0300900	-0.0228170
0.0445700	0.0349250	0.0432100	-0.0268230
0.0619900	0.0401600	0.0587600	-0.0301220
0.0821700	0.0442810	0.0766900	-0.0326180
0.1049900	0.0473760	0.0969400	-0.0343760
0.1302500	0.0500600	0.1194500	-0.0356080
0.1577500	0.0521800	0.1441000	-0.0366080
0.1872900	0.0539200	0.1707700	-0.0376320
0.2186600	0.0550200	0.1992900	-0.0387180
0.2349500	0.0553800	0.2294600	-0.0393250
0.2516300	0.0555220	0.2450900	-0.0393920
0.2686500	0.0555560	0.2610600	-0.0394470
0.2859800	0.0554370	0.2773300	-0.0394000
0.3036100	0.0551880	0.2938700	-0.0392680
0.3215000	0.0548320	0.3106500	-0.0390670
0.3396100	0.0543890	0.3276500	-0.0388090
0.3579300	0.0538760	0.3448300	-0.0385060
0.3764200	0.0533060	0.3621700	-0.0381680
0.3950500	0.0526880	0.3796500	-0.0376020
0.4138000	0.0520280	0.3972300	-0.0374130
0.4326200	0.0513280	0.4149200	-0.0370030
0.4515000	0.0505070	0.4327000	-0.0365730
0.4704200	0.0498000	0.4505900	-0.0361190
0.4893400	0.0489610	0.4686100	-0.0356380
0.5082500	0.0480630	0.4868000	-0.0351230
0.5271400	0.0470950	0.5051900	-0.0345660
0.5459900	0.0460470	0.5237900	-0.0339580
0.5648100	0.0449100	0.5426200	-0.0332880
0.5835900	0.0436730	0.5616700	-0.0325470
0.6023200	0.0423260	0.5809300	-0.0317250
0.6209800	0.0408720	0.6003700	-0.0308130
0.6395600	0.0393000	0.6199700	-0.0295040
0.6580200	0.0376160	0.6396800	-0.0286940
0.6763400	0.0358230	0.6594700	-0.0274620
0.6944700	0.0339350	0.6792800	-0.0261730
0.7123900	0.0319640	0.6990600	-0.0247730
0.7300500	0.0299320	0.7187600	-0.0232990
0.7474200	0.0278610	0.7383100	-0.0217690
0.7644600	0.0257780	0.7576700	-0.0202070
0.7811300	0.0237120	0.7767600	-0.0186460
0.7974000	0.0216950	0.7955200	-0.0171180
0.8132300	0.0197570	0.8135600	-0.0156630
0.8286000	0.0178200	0.8317200	-0.0143170
0.8578000	0.0144010	0.8490200	-0.0131170
0.8847800	0.0107400	0.8656600	-0.0120980
0.9093200	0.0076470	0.8815800	-0.0107710
0.9312300	0.0048860	0.9109300	-0.0083240
0.9503600	0.0024750	0.9365300	-0.0061900
0.9665400	0.0004360	0.9579900	-0.0044010
0.9734900	-0.0002830	0.9750400	-0.0031170
0.9696000	-0.0010618	0.9875600	-0.0023390
1.0000000	-0.0017000	1.0000000	-0.0017000

Table A.1: Airfoil coordinates of SC1095

Upper Surface		Lower Surface	
x/c	y/c	x/c	y/c
0.00	0.00	0.00	0.00
0.0008200	0.0050470	0.0015000	-0.0075230
0.0039700	0.0128660	0.0052400	-0.0121080
0.0096600	0.0217500	0.0111900	-0.0153640
0.0183300	0.0307540	0.0194300	-0.0177590
0.0299900	0.0392540	0.0300900	-0.0194550
0.0445700	0.0473600	0.0432100	-0.0207000
0.0619900	0.0528920	0.0587600	-0.0219420
0.0821700	0.0573750	0.0766900	-0.0227870
0.1049900	0.0609810	0.0969400	-0.0234150
0.1302500	0.0637490	0.1194500	-0.0239318
0.1577500	0.0657359	0.1441000	-0.0244140
0.1872900	0.0670059	0.1707700	-0.0249160
0.2186600	0.0676209	0.1992900	-0.0254340
0.2349500	0.0677040	0.2294600	-0.0259670
0.2516300	0.0676469	0.2450900	-0.0262250
0.2686500	0.0674599	0.2610600	-0.0264680
0.2859800	0.0671479	0.2773300	-0.0266880
0.3036100	0.0667199	0.2938700	-0.0268800
0.3215000	0.0661829	0.3106500	-0.0270340
0.3396100	0.0655450	0.3276500	-0.0271460
0.3579300	0.0648119	0.3448300	-0.0272100
0.3764200	0.0639910	0.3621700	-0.0272230
0.3950500	0.0630890	0.3796500	-0.0271820
0.4138000	0.0621130	0.3972300	-0.0270890
0.4326200	0.0610690	0.4149200	-0.0269440
0.4515000	0.0599640	0.4327000	-0.0267530
0.4704200	0.0588020	0.4505900	-0.0265230
0.4893400	0.0575910	0.4686100	-0.0262600
0.5082500	0.0563290	0.4868000	-0.0259770
0.5271400	0.0549620	0.5051900	-0.0256880
0.5459900	0.0535140	0.5237900	-0.0253340
0.5648100	0.0519880	0.5426200	-0.0248840
0.5835900	0.0503880	0.5616700	-0.0243450
0.6023200	0.0487180	0.5809300	-0.0237210
0.6209800	0.0469820	0.6003700	-0.0230200
0.6395600	0.0451860	0.6199700	-0.0222470
0.6580200	0.0433350	0.6396800	-0.0214110
0.6763400	0.0414360	0.6594700	-0.0205200
0.6944700	0.0394980	0.6792800	-0.0195800
0.7123900	0.0375270	0.6990600	-0.0186010
0.7300500	0.0355320	0.7187600	-0.0175880
0.7474200	0.0335200	0.7383100	-0.0165520
0.7644600	0.0315020	0.7576700	-0.0154500
0.7811300	0.0294860	0.7767600	-0.0144300
0.7974000	0.0278000	0.7955200	-0.0133590
0.8132300	0.0254940	0.8135600	-0.0122900
0.8286000	0.0235340	0.8317200	-0.0112290
0.8578000	0.0197310	0.8490200	-0.0101830
0.8847800	0.0161300	0.8656600	-0.0091580
0.9093200	0.0127890	0.8815800	-0.0081690
0.9312300	0.0097580	0.9109300	-0.0062670
0.9503600	0.0070800	0.9365300	-0.0045560
0.9665400	0.0047890	0.9579900	-0.0030710
0.9734900	0.0038000	0.9750400	-0.0018530
0.9696000	0.0014970	0.9875600	-0.0009340
1.0000000	0.0000010	1.0000000	-0.0000020

Table A.2: Airfoil coordinates of SC1095 R8

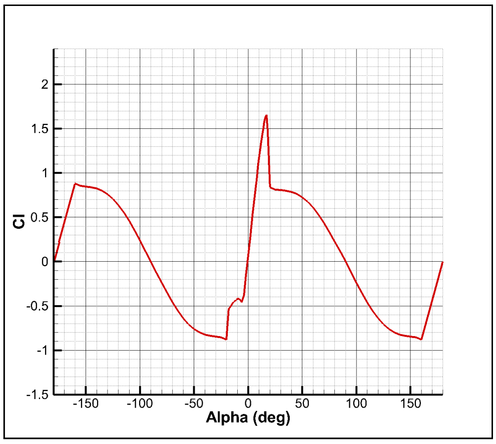

(a) Cl vs angle of attack

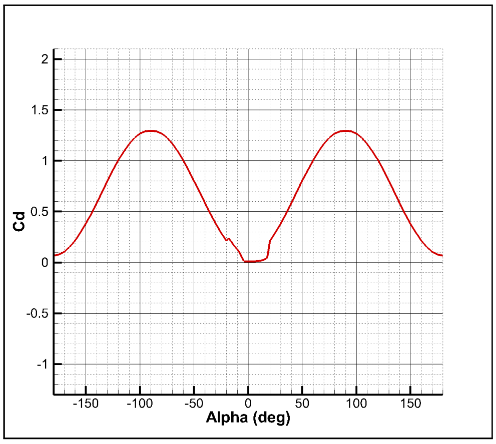

(b) Cd vs angle of attack

Figure A.4: Cl and Cd variation with angle of attack of SC1095 R8 at section 1

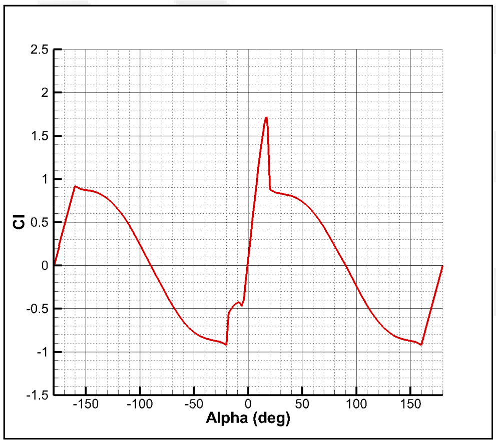

(a) Cl vs angle of attack

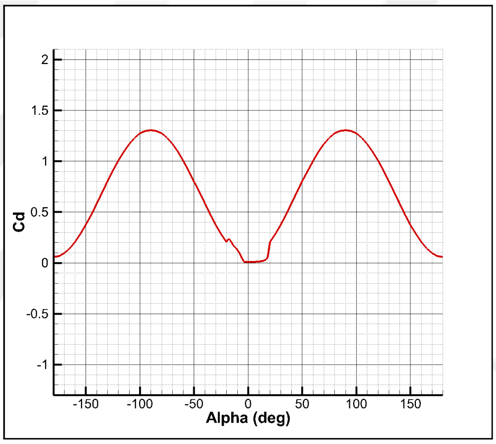

(b) Cd vs angle of attack

Figure A.5: Cl and Cd variation with angle of attack of SC1095 R8 at section 2

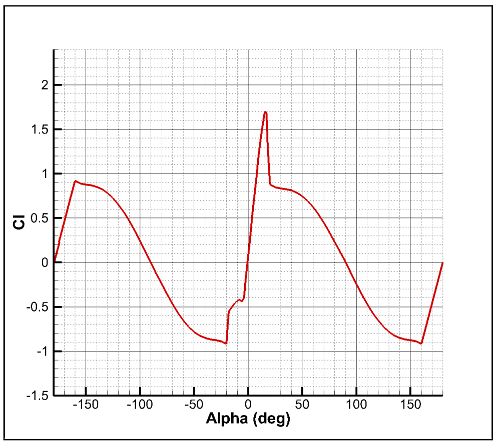

(a) Cl vs angle of attack

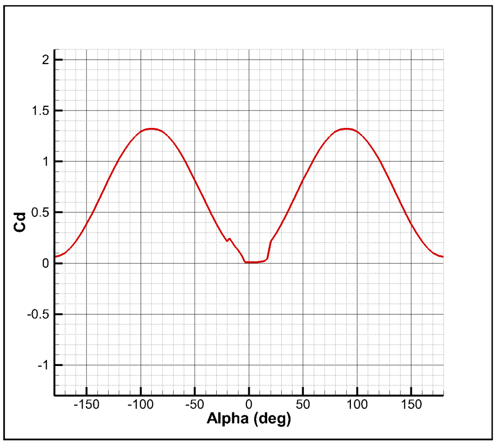

(b) Cd vs angle of attack

Figure A.6: Cl and Cd variation with angle of attack of SC1095 R8 at section 3

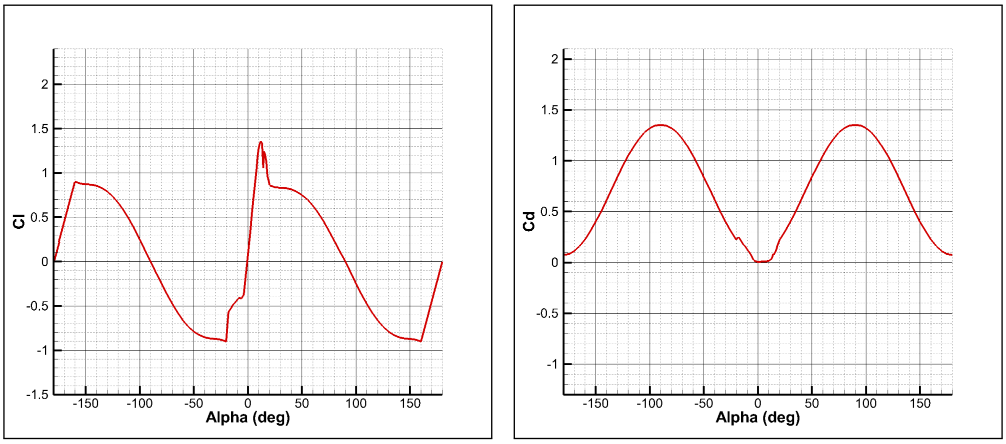

(a) Cl vs angle of attack (b) Cd vs angle of attack

Figure A.7: Cl and Cd variation with angle of attack of SC1095 R8 at section 4

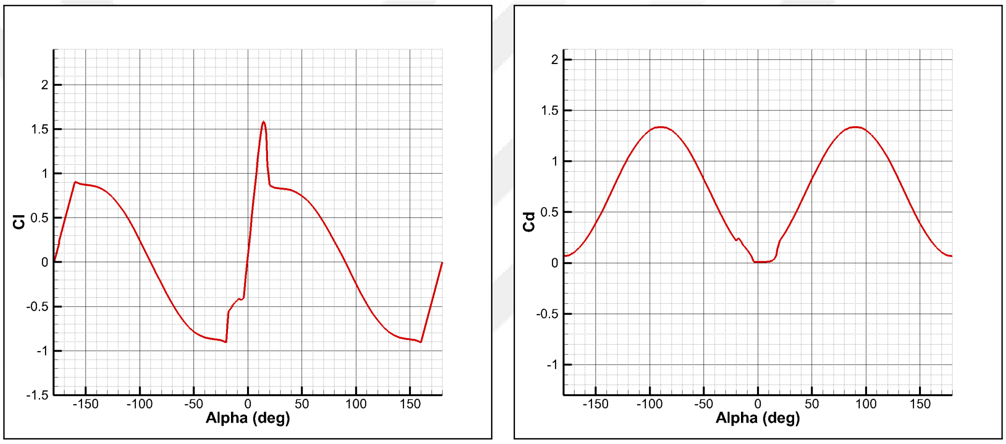

(a) Cl vs angle of attack (b) Cd vs angle of attack

Figure A.8: Cl and Cd variation with angle of attack of SC1095 R8 at section 5

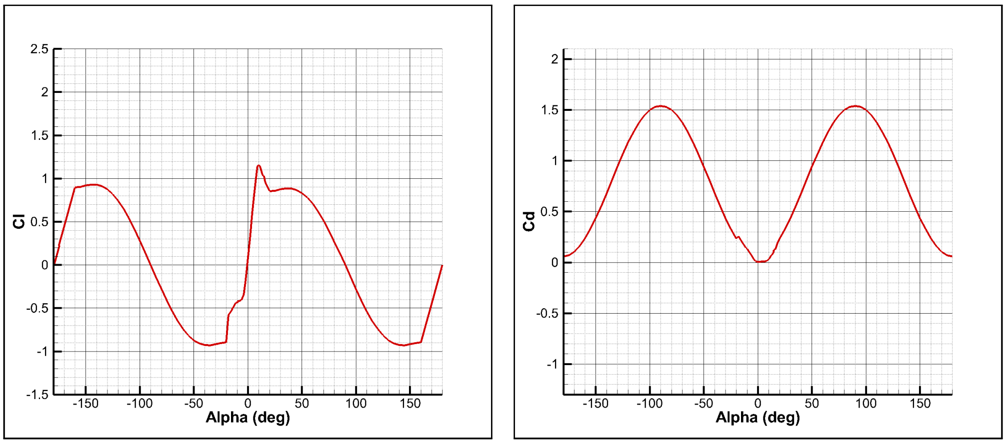

(a) Cl vs angle of attack (b) Cd vs angle of attack

Figure A.9: Cl and Cd variation with angle of attack of SC1095 R8 at section 6

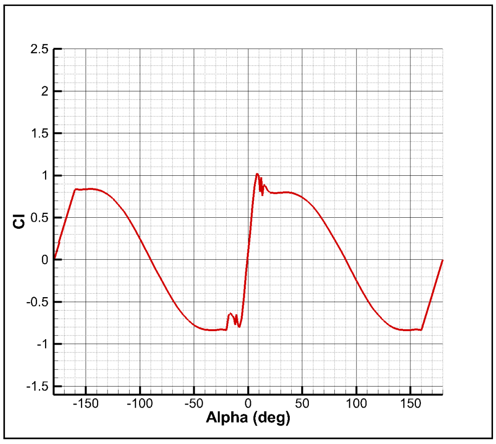

(a) Cl vs angle of attack

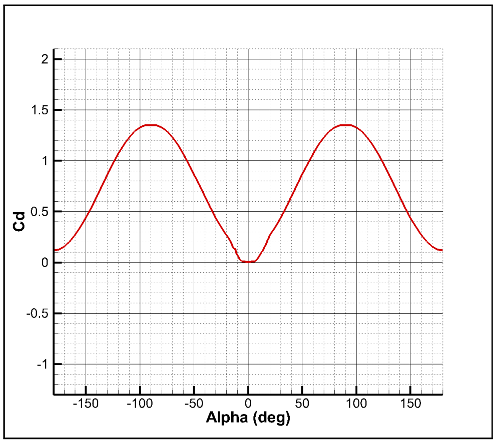

(b) Cd vs angle of attack

Figure A.10: Cl and Cd variation with angle of attack of SC1095 at section 7

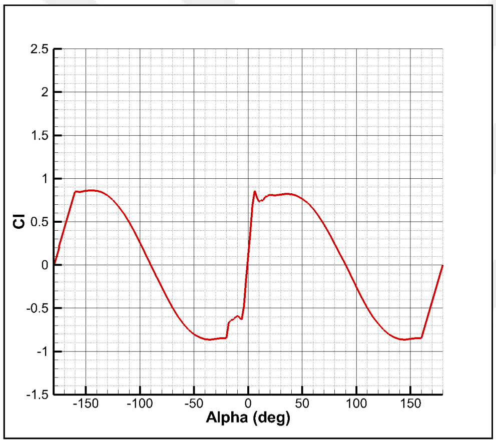

(a) Cl vs angle of attack

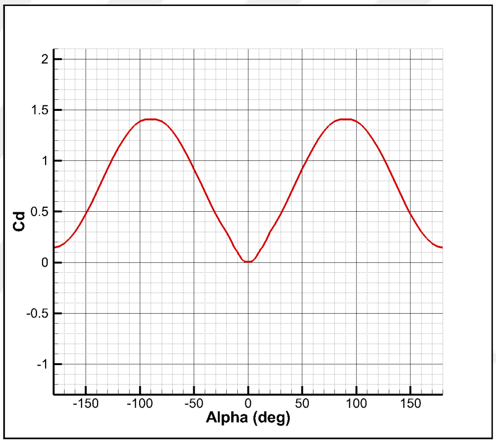

(b) Cd vs angle of attack

Figure A.11: Cl and Cd variation with angle of attack of SC1095 at section 8